RAPID ON-DEMAND LAUNCH MISSION PLANNING

FOR TIMELY DELIVERY OF SPACECRAFT

CONSTELLATIONS

by

CHRISTOPHER ROSS SIMPSON

RICHARD D. BRANAM, COMMITTEE CHAIR
CHARLES R. O'NEILL, CO-CHAIR
SIVA PRASAD GOGINENI
BRENDAN P.W. AMES
JOHN CARR
SEMIH M. OLCMEN
WEIHUA SU

A DISSERTATION

Submitted in partial fulfillment of the requirements
for the degree of Doctor of Philosophy
in the Department of Aerospace Engineering and Mechanics
in the Graduate School of
The University of Alabama

TUSCALOOSA, ALABAMA

2021

ABSTRACT

On-demand launch from an airborne launch vehicle can provide a nanosatellite overhead in under an hour anywhere in the world. On-demand launch can support capabilities already on-orbit and provide tailored or new capabilities rapidly. A military rapid on-demand launch fulfills operational requirements for on-demand space support and reconstitution. Current capabilities in tracking and denial of space-assets limits the effectiveness of constellations already on-orbit to be operationally responsive in military space. Time-sensitive returns using scheduling algorithms for the timely deployment of a nanosatellite constellation can be achieved. Four case studies show the capability to provide persistent coverage of a moving target to provide terminal guidance to a net-enabled weapon, provide reconstitution of a PNT constellation, view persistence, and on-demand coverage of natural phenomena for disaster response. The three novel contributions of this work are creation of a mission planning system to deliver a constellation on-demand to observe a target from anywhere in the world using tactical airborne aircraft, combining existing vehicle models for aircraft, launch vehicle, satellite, and optimization tools to modify on-demand launch scheduling of a constellation for optimal coverage, and applying previously existing coverage quality measurements to measure replenishment and reconstitution value added by on-demand launch. A mission planning system for delivery of multiple satellites from multiple similar air-launched platforms for constellation installation over any selected point constrained for reaction time with optimized coverage quality is delivered.

DEDICATION

I apologize for my brevity. This by no means does those included justice nor does it mention all those that have helped me along my journey. To those not mentioned here; thank you. To those mentioned here; know that you mean more to me than I can express with words set upon a page.

To my family;

My father, who may no longer be with us physically, but continues to inspire. My mother, who shows me daily the strength and stubbornness needed to tackle your goals. My wife, without whose loving support I would still be writing. My dogs, who remind me to that it's time to "PLAY" once in a while.

To my friends;

Charles O'Neill, who continues to fine-tune the undergraduate that knocked on his door nearly 6 years ago. My friends, Ed and Eddie Hackett and Jarrett Robinson, thank you for your honest insight, constructive criticism, and continual support.

LIST OF SYMBOLS AND ABBREVIATIONS

Symbols

A	Area
a	Semi-major Axis
C_d	Drag Coefficient
C_l	Lift Coefficient
C_{per}	Percent Coverage
e	Eccentricity
$E[x]$	Expected Value or First Moment of Random Variable x
G	Coverage Gap Duration
G_{mrt}	Mean Response Time
G_{avg}	Time-Averaged Gap Duration
G_{max}	Maximum Coverage Gap Duration
i	Inclination
M	Mean Anomaly
P	Orbital Period
t_0	Initial Time
t_i	Time at Some Instant, i
t_f	Final Time
t_{rt}	Response Time

$V[x]$	Variance or Second Central Moment of Random Variable x
ϕ	Latitude
λ	Longitude
Ω	Right Ascension of the Ascending Node
ω	Argument of Perigee
ν	True Anomaly
μ	Gravitational Parameter

Abbreviations

LEO	Low-Earth Orbit
GEO	GEOstationary orbit
USSF	United States Space Force
MRT	Mean Response Time
FoM	Figures of Merit
COLA	Collision On Launch Assessment
CA	Conjunction Assessment
RSC	Remote Sensing Center
SAR	Synthetic Aperture Radar
PNT	Precise Navigation and Timing
DARPA	Defense Advanced Research Projects Agency
PNT	Precise Navigation and Timing
USSOCOM	United States Special Operations Command
SBIR	Small Business Innovation Research

ISR	Intelligence, Surveillance, and Reconnaissance
DoD	Department of Defense
CONOPS	CONcept of OPerationS
USRA	Universities Space Research Association
ESA	European Space Agency
CYGNSS	Cyclone Global Navigation Satellite System
SMAP	Soil Moisture Active Passive
ISIS	Innovative Solutions In Space
CFSCC	Combined Force Space Component Command
SSN	Space Surveillance Network
CSpOC	Combined Space Operations Center
SSA	Space Situational Awareness
TDRSS	Tracking and Data Relay Satellite System
UAVs	Unmanned Aerial Vehicles
TDMA	Time Division Multiplexed Architecture
COLA	Collision On Launch Assessment
NOTS	Naval Ordance Test Station
NAWCWD	Naval Air Warfare Center – Weapons Development
SSO	Sun-Synchronous Orbit
GTO	Geostationary Transfer Orbit
DARPA	Defense Advanced Research Projects Agency
IRIS	Interface Region Imaging Spectrograph
ICON	Ionospheric CONnection explorer

MILP	Mixed Integer Linear Programming

ACKNOWLEDGMENTS

I would like to gratefully acknowledge the Science, Mathematics & Research for Transformation (SMART) program for scholarship assistance; allowing me to complete my graduate education at The University of Alabama. I also would like to gratefully acknowledge Michael D. Squire for assistance in determining satellite lifetimes and Dr. Richard D. Branam for assistance in launch vehicle performance modeling. I also want to address special thanks to my committee members, Dr. Brendan P.W. Ames, Dr. John Carr, Dr. Semih M. Olcmen, Dr. Weihua Su, and Dr. Siva Prasad Gogineni.

CONTENTS

LIST OF TABLES

LIST OF FIGURES

1. INTRODUCTION

General background on airborne launch vehicles, their advantages and history, and small satellite trends is provided. The motivation for the work, rapid response deployment of a constellation of satellites, is described in detail from the three areas rapid launch has an immediate impact; military, disaster response, and rapid science return. This overview is followed by a comprehensive literature review of distributed nano- and microsatellite systems, constellation coverage operations, agile constellations, on-demand launch, and airborne launch vehicles. The methodology provides the supporting evidence that drove the development of this work. Orbital mechanics, perturbing forces, and collision assessment will be reviewed. Earth coverage, including coverage parameters, figures of merit, and how communications between satellite, satellite, ground, and ship will be treated as payload agnostic. Having laid the groundwork, constellation design, airborne launch vehicles, and on-demand launch, including scheduling and test cases to model, will be discussed. The technical discussion and results will demonstrate utility of the timely delivery via four test cases. Finally, the conclusions summarize the results, the contributions of the work at hand, current applications, and future work.

1.1 Background

Airborne launch vehicles and airborne anti-satellite missiles have been around since the dawn of the space age. In October 1957, in response to Sputnik, Naval Ordance Test Station (NOTS) China Lake, California, now Naval Air Warfare Center – Weapons Development (NAWCWD) China Lake, developed NOTSNIK (Bille & Lishock, 2002; Lawson, 2017), carried

Figure 1-1. Successful launch of an anti-satellite, or ASAT, missile from a highly modified F-15A Sept. 13, 1985 scoring a direct hit on a satellite orbiting 340 miles overhead. (Reynolds, 1985)

on a Douglas F4D-1 Skyray. NOTSNIK launched satellites and was used as a satellite interceptor. The USAF would complete and test an air-launched anti-satellite missile or ASM-135 from the F-15A against the US Solwind P78-1 satellite on 13 September 1985 (Garwin & Pike, 1984; Kelly, Rogers, Brierly, Martin, & Murphy, 2017; Lawson, 2017; Reynolds, 1985). This launch using the over-the-shoulder maneuver (Horton & Messing, 1963) from a power climb inspired the space community with a vision of responsive space lift capability. Tactical aircraft including the McDonnell-Douglas/Boeing F-15, Lockheed F-104, and Sukhoi SU-27, and commercial aircraft Boeing 747-400 and Lockheed L-1011 TriStar have all been considered as possible first stages for the airborne launch vehicle (Bartolotta et al., 2011; Carter, 2016; DePasquale, Charania, Matsuda, & Kanayama, 2010; Foust, 2014; Hague, Siegenthaler, & Rothman, 2003; Kloesel & Clark, 2013; Kloesel, Ratnayake, & Clark, 2011). Northrop Grumman's, formerly Orbital Sciences Corporation's (Orbital ATK), Pegasus has flown 44 times in 30 years and was the only successful airborne launch vehicle until LauncherOne's launch on 17 January 2021 (Foust, 2014). The Pegasus launch vehicle uses a modified Lockheed L-1011 TriStar and LauncherOne launch vehicle uses a modified Boeing 747-400. Besides the cost-advantage of a reusable first stage, see aircraft, airborne launch vehicles provide schedule and orbit flexibility. Fixed launch

sites often have launches scheduled years in advance and are limited in orbit injection capability due to safety constraints.

Increased demand for mega-constellations increases the market for small launch vehicles. As of December 2018, given the 10,000 satellites that need to be launched within the following 6 years, 64 launches are needed annually to meet demand. Given the current launch capability and existing contracts, a shortfall of 34 launches is expected. Discounting on-orbit spares and assuming failed satellites are replaced on an individual basis, small launchers could see up to 100 launches for a 1% annual failure rate. OneWeb already has a contract arrangement with Virgin Orbit for 39 LauncherOne missions (Cates, Houston, Conley, & Jones, 2018). Rapid reuse isn't determined by the launch vehicle alone. Schedule flexibility is also affected by launch range availability, launch pad throughput, efficiency of the range to reset between launch events, and launch service provider requirements, assuming of course the primary payload is already prepared.

Long-term projections indicate as many as 2,400 nano- and microsatellites launched in the next 5 years with the small satellite launch market exceeding $62 billion by 2030 (*NANO/MICROSATELLITE MARKET FORECAST*, 2020; *Small-Satellite Launch Services Market, Quarterly Update (Q1 2018), Forecast to 2030*, 2018). Larger satellites reflect the trend in satellite production towards redundant systems, highly reliable components, and in the case of military applications, defensive countermeasures. Smaller satellites address these requirements by an increase in numbers enabled by a decrease in production cost.

Satellites in Low-Earth Orbit (LEO) for Earth observation make use of repeating orbits to meet the revisit requirements of their particular mission. GEOstationary (GEO) satellites provide frequent revisits at the cost of coarse spatial resolution, extra launch costs, no polar access, and

inflexible point coverage. LEO satellites require additional numbers and coordination to achieve frequent revisits. To achieve time-sensitive returns, where total reaction time of under an hour is requested, use of scheduling algorithms for multiple near-simultaneous launches globally to place a constellation in LEO is proposed. Specifically, *a mission planning system to optimize delivery of multiple satellites from multiple similar air-launched platforms for constellation installation meeting a specified minimum duration* is the focus of this effort.

1.2 Motivation

Responsive space demonstrates the demands of an interconnected world. The ability to deliver on-demand space capability in a matter of hours is of vital interest to the government and becoming of interest to commercial entities too. Commercial missions have time-critical schedules driven by market pressures and regulatory hurdles. Constellations need to be replenished to restore coverage and continue service to customers. Commercial technology demonstration missions need a cheap accessible ride to space in months, not years. Government drivers for rapid replenishment include weather coverage, communications, and global navigation satellite systems. Airborne launch vehicles provide the schedule flexibility required of a rapid launch.

1.2.1 Government or military response

Operation Desert Storm in 1991 saw the first large-scale use of the space domain in a conflict. Satellites were used for Precise Navigation and Timing (PNT), weather, communications, imagery, and tactical early missile attack warning. The biggest contribution to the conflict was PNT in the form of GPS enabling the wide left sweep or “Hail Mary” plan which avoided fixed Iraqi defenses and destroyed the strategic reserve deep in Iraqi territory (Lang, 2016). The Department of the Navy commissioned a study from the Naval Studies Board

of the National Research Council, published in 2006, on Command, Control, Communications, Computers, Intelligence, Surveillance, and Reconnaissance (C4ISR) for future naval strike groups. Forward deployed naval forces are to be distributed more widely to enhance forward deterrence and rapid response. At the time, naval forces were unable to meet these goals because of gaps in C4ISR. Relevant findings included (*C4ISR for Future Naval Strike Groups*, 2006);

- Network-centric operations that draw C4ISR more prominently into the kill chain can significantly improve future naval strike group capabilities.
- Current ISR capabilities of naval strike groups have a shortfall in persistent ground and sea-surface surveillance.
- The time required for sensors to respond to a commander's tasking is typically too long for tactical utility, and the commander has few tools for recognizing deficiencies in the tactical picture.

Satellite communications or space-based radar from Operationally Responsive Space (ORS) launch can provide on-demand space support in disadvantaged theaters. The network-centric capabilities enable cooperative engagement of relocatable, hiding, and moving targets. China, Russia, and other state actors have taken notice of US reliance on space-assets and considerably developed their space and counterspace capabilities that threaten "de facto" US superiority in space. These increased capabilities by near-peer countries require the US to take safeguards to protect our military, intelligence, and commercial space assets (Lt. Col. Whitney, Maj. Thompson, & Maj. Park, 2019). The US Space Force establishment on 20 December 2019 is in direct response to these priorities.

The People's Republic of China's (PRC's) January 2007 kinetic kill anti-satellite SC-19 test against a Fengyun-1C weather satellite at an altitude of 863 km demonstrated China's ASAT

capability. Comments by PLA officers and PRC civilian analysts justified the ASAT test as needed to counter perceived US hegemony in space and target the vulnerability of US dependence on satellites (Kan, 2007). Two islands in the Spratly Island chain, confirmed as of April 2018, including Mischief Reef, support jamming systems for targeting communications and radar (Harrison, Johnson, Roberts, Way, & Young, 2020). GPS signals for the Automatic Identification System (AIS) in the port of Shanghai and 19 other locations along the Chinese coast experienced significant spoofing attacks during 2018 and 2019 (Harrison et al., 2020).

Figure 1-2. PL-19/Nudol direct ascent ASAT system mounted a mobile transporter erector-launcher (TEL) (Almaz-Antey, 2015).

Russia inherited the majority of the former Soviet Union's vast space infrastructure. Russia established the first space force in 1992 when the Russian Ministry of Defense was created in 1992. In March and December 2018 Russia demonstrated the PL-19/Nudol direct ascent ASAT system from a mobile transporter erector-launcher (TEL). In December 2019 and January 2020, Cosmos 2542, a Russian inspector satellite deployed from Cosmos 2543, made several close approaches to USA 245, potentially a National Reconnaissance Office satellite. These close approaches could have been to observe the satellite, intercept communications, or take control of the satellite (Harrison et al., 2020; Weeden & Samson, 2020). Russia is sponsoring scientific research into on-orbit aerosol obscurants, with defensive and offensive capabilities. Russia has deployed widespread GPS jamming and spoofing since 2014, affecting civilian and military vessels near Russian territory and commercial and civilian aircraft

in the Arctic Circle (Harrison et al., 2020; Humphreys, Ledvina, Psiaki, O'Hanlon, & Kintner Jr., 2008; Weeden & Samson, 2020).

The United States Special Operations Command (USSOCOM) 19.3 Small Business Innovation Research (SBIR) Direct to Phase II Proposal in 2019 requested nanosatellite, 1-10 kg, payloads for tactical Intelligence, Surveillance, and Reconnaissance (ISR) (*19.3 Small Business Innovation Research (SBIR) Direct to Phase II Proposal Submission Instructions*, 2019). USSOCOM and the Department of Defense (DoD) have recognized the feasibility of using nanosatellite platforms for actual operation capabilities. USSOCOM is interested in more abundant ISR data of various forms for rapid collection and dissemination of actionable data. The emphasis is on rapid tactical operation with an envisioned CONcept of OPerationS (CONOPS) having a user in tactical theatre issue an ISR request to the constellation and quickly downlinking the results to the user.

The proposed CONOPS of USSOCOM features a constellation of scaled ISR satellites is at a disadvantage when it comes to successfully navigating just the demands in launch services (Cates et al., 2018). A large constellation to meet the demands of USSOCOM will require constellation replenshiment scheduling (Smith, 2018), which may require the additional penalty of a particulary demanding schedule due to limitations on orbital lifetime (Dell'Elce, Arnst, & Kerschen, 2015). Satellites are easily tracked from fixed terrestrial launch sites to their final orbital station. Current capabilities in the denial of space-based resources (Harrison et al., 2020; Kan, 2007; Weeden & Samson, 2020) can threaten the same operations the constellation was deployed to support. An innovative alternative would be to develop a global delivery capability for flexible and responsive delivery to a specified orbit profile from any tactical fighter aircraft

or commercial derivative. The United States Space Force (USSF) and SPACECOM are seeking to do that.

The United States Space Force's (USSF) Space and Missile Systems Center released a Small Rocket Program-Orbital (SRP-O) Agile Small Launch Operational Normalizer-45 (ASLON-45) FA8818-18-R-0011 recently awarded to Aevum for their Ravn-X platform. The Ravn-X concept is a large UAV delivering an airborne two-stage launch vehicle to orbit for a single nanosatellite payload. The USAF and now USSF look to develop platforms to provide rapid reconstitution, replenishment, and tailored capabilities on-demand.

1.2.2 Disaster response

The data provided by constellations to disaster management and response is critically dependent upon time of response. Through optimization of the launch location using an airborne platform and a satellite with the requested instrument available, optical or radio frequency, a constellation could see first light over the requested area in under an hour *from anywhere in the world*.

In 28 December 2019, Puerto Rico was shaken by a series of hundreds of small earthquakes culminating in a powerful 6.4 magnitude earthquake on 7 January 2020. Using C-band Synthetic Aperture Radar (SAR) from the European Space Agency's (ESA's) Copernicus Sentinel-1 to identify damaged structures, surface displacement, and preliminary mapping of possible landslides. Optical data from NASA satellites for the "Black Marble" maps was provided to FEMA Region II's Geospatial Resource Center by Universities Space Research Association's (USRA's) Earth from Space Institute (Cole, 2020). Timely satellite data mapping affected regions is critical to disaster response. Maxar Technologies and Planet contributed their mapping, imagery, and analysis to civil agencies responding to the crisis (Werner, 2019).

Cyclone Global Navigation Satellite System (CYGNSS) was launched in 2016 to gather more data on the winds in these tropical cyclones as part of an effort to increase data coverage of hurricanes and aid forecasts. CYGNSS is able to provide its core capability through reflections from Global Navigation Satellite System (GNSS) constellations, or passive bistatic radar (Zribi et al., 2018). CYGNSS can provide secondary capability in monitoring soil moisture and flood detection. CYGNSS has an advantage over traditional flood detection and soil moisture satellite monitoring because of its reliance on GNSS. Flood detection is performed by processing sensor data from optical sensors on the U.S. Geological Survey-NASA Landsat satellites and the SAR, microwave sensors, on the European Space Agency's Sentinel 1 and 2. CYGNSS's advantage over other space-based sensors for flood detection is its ability to see through clouds, rain and vegetation. The unbiased root-mean-square difference between daily averaged CYGNSS soil moisture and Soil Moisture Active Passive (SMAP) satellite measured soil moisture is 0.045 cm^3/cm^3. NASA's SMAP mission cost upward of a billion dollars. Each of the eight CYGNSS satellites are 27.5 kg or a little larger than a 12U CubeSat and is hundreds of millions of dollars less expensive (Chew, Reager, & Small, 2018; Chew & Small, 2017; Ruf et al., 2018).

Based on CYGNSS's success, Spire Global, Inc. a 3U CubeSat constellation operator launched two CubeSats equipped for GNSS-Reflectometry measurements on December 11, 2019 and began collecting data after LEOP on January 2, 2020 (Werner, 2020). A 3U CubeSat launched from an airborne platform with GNSS-R for flood detection from a cyclone, tsunami, or regional event could be a response to provide timely information to disaster coordination efforts around the world.

1.2.3 Rapid science return

Arctic cyclones are most common during the summer and pose hazards to ships navigating opening passages and aircraft operating in the Arctic Ocean. Frequent winds, fog, and icing, hazardous to air operations, remain difficult to predict due to underdeveloped climate models. Accurate forecasts of the "Great Arctic Cyclones" in August 2012 and August 2016 were only provided 3 days out (Doyle, Fearon, Finocchio, & Amerault, 2019). Thinner sea ice is susceptible to atmospheric forcing from cyclones. Hazardous conditions from cyclones include weather, sea, and ice conditions can pose a threat to Navy maritime operations and national security. Alaska offers the quickest flight access to strategic locations in the Pacific region and western Russia (Barrett, 2020).

Arctic strategy for Air and Space Forces include collaboration with interagency partners to expand meteorological coverage. Specifically, the Space Force is responsible for devising capabilities to mitigate and predict environmental disturbances unique to the Arctic region (Barrett, 2020). Weather in the Arctic changes rapidly. Taking advantage of unique polar orbital regimes, on-demand launch can provide critical meterological data necessary to improve weather models and augment existing terrestrial sensors.

The Remote Sensing Center (RSC) at the University of Alabama has focused on soil moisture measurements, sounding and imaging ice sheets, and snow pack measurements (Taylor et al., 2019; Yan et al., 2017; Yan, Nunn, Gogineni, O'Neill, Simpson, Taylor, Li, et al., 2019; Yan, Nunn, Gogineni, O'Neill, Simpson, Taylor, Steinhage, et al., 2019) by making use of airborne Synthetic Aperture Radar (SAR) and ground radar. Measurements with a small satellite constellation using SAR from the extreme or physically difficult locations of ice sheets and snow pack measurements would improve the science return of previous and future expeditions

(Gogineni et al., 2018). This highlights the continuing return that an on-demand launch of a CYGNSS or SAR mission to the Arctic theater of operations would provide.

1.3 Work outline

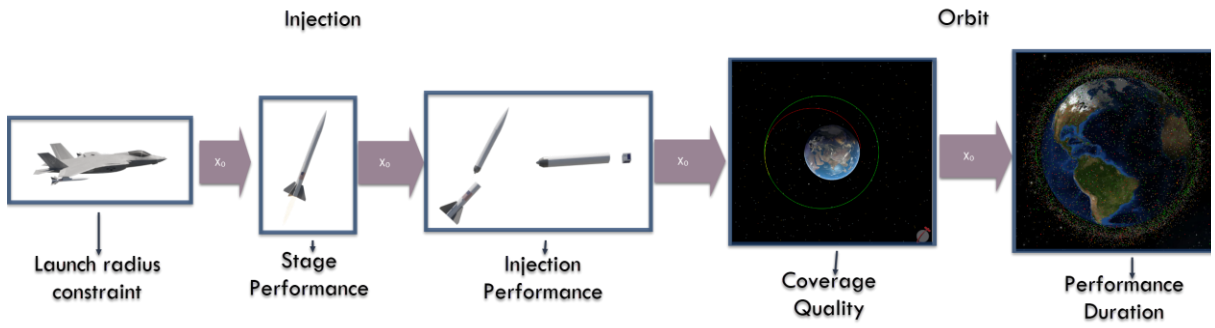

Figure 1-3. Modular design/outline of work.

An effective mission planning system to optimize delivery of multiple satellites from multiple similar air-launched platforms will be constructed of five software modules. Aircraft performance will determine launch radius constraints, stage performance of the launch vehicle will determine the injection, and the selected orbit will determine coverage quality and performance degradation over the lifetime of the constellation. Effective satellite coverage is measured based on three questions; 1. How quickly? 2. How often? and 3. How long? The success of such a mission will rely on reaction time, coverage quality, and lifetime of the constellation. Reaction time, coverage quality, and constellation lifetime are the three measurable answers to the three questions, respectively. The reaction time is the time from a request at a random time until the point requested is observed. Coverage or time over target of the constellation quantitatively determined by Figures Of Merit (FOM) is the coverage quality. Constellation lifetime must be determined to measure the resulting performance degradation as satellites deorbit. These mission requirements, Appendix A.1, are critical to the determining the effectiveness of the rapid response constellation delivered.

1.3.1 Constellation performance

The reaction time is the time from the beginning of the simulation, or time of random request, until the target is first observed, Eq. (1-1). In most cases, observations could be downlinked to the same location observed. Some consideration will be given to those cases where the satellite will have to downlink its observations or communications later.

$$t_{rt} = G_t(x_0) \tag{1-1}$$

Trajectory planning for the aircraft and launch vehicle must be optimized to meet the constraint reaction time. Orbit selection will also be important. An off-nadir pass may be optimal for the overall coverage quality while meeting the reaction time constraint. The combination of time until downlink, pass, launch, and flight will determine the total reaction time.

The percent coverage, C_{per}, Eq. (1-3), of the point is the number of time steps the point was covered over the number of time steps. The maximum gap duration, G_{max}, Eq. (1-2), of the point is the maximum gap in simulation time. The Time-Averaged Gap, TAG, G_{avg}, Eq. (1-5), is the average duration of a gap if randomly sampling the system, and the Mean Response Time, MRT, G_{mrt}, Eq. (1-4), is the average time from a request at a random time until the point requested is observed. Percent coverage, maximum gap duration, time-averaged gap, and mean response time are common FOM used to compare coverage (Crisp et al., 2018; Post et al., 2007; Savitri, Kim, Jo, & Bang, 2017; *Space Mission Analysis and Design*, 2003; Wang, Luo, Dai, & Chen, 2016).

Figures of Merit	**Units**	
$G_{max} = \max(G_t)$	Time	(1-2)
$C_{per} = \frac{\sum_{i=0}^{N} x_i}{N} = \frac{\Delta t - \Sigma G_t}{\Delta t}$	N/A	(1-3)
$G_{mrt} = E[G_t]$	Time	(1-4)

$$G_{avg} = \frac{\Sigma G_t^2}{\Delta t} \qquad \text{Time} \quad (1\text{-}5)$$

The FOM provided in Eqs. (1-2)-(1-5)), can be applied to satellite navigation for Position, Navigation, and Timing (PNT) but Dilution of Precision (DoP) provides a geometric factor multiplied by measurement and other input, gives the error in position or time. A tactical digital data link (TDL), such as Link-16, JTIDS/TADIL J system, can be used as a navigation aid in GPS-denied environments. Using the time-of-arrival (TOA) the pseudorange between other participants in the network can be determined in Eq. (1-6). DoP and Link-16 quality combined with estimates of inertial measurements onboard vehicles is useful in determining the quality of solution. Reducing the covariance matrix of the receiver solution by assuming equal and independent measurement and model errors, $C_{\Delta x} = (A^T A)^{-1}\sigma^2 = D\sigma^2$, where σ represents the standard deviation of the psuedorange measurement error plus the residual model error, we can obtain a measurement of the overall quality of the solution.

$$\tilde{\rho} = \rho + d_{prop} + e \qquad (1\text{-}6)$$

$$\sigma_G = \sqrt{\sigma_E^2 + \sigma_N^2 + \sigma_U^2 + \sigma_T^2} = \sqrt{tr(D)}\sigma \qquad (1\text{-}7)$$

The scaling factor, $\sqrt{tr(D)}$, a function of receiver and transmitting satellites positions and clock offsets, dilutes the precision of the position determination amplifying the pseudorange error. This scaling factor is called the geometric dilution of precision. Using the four minimum satellites, the lowest possible geometric DoP is 1.732 which is directly correlated with the tetrahedron volume formed by the receiver to satellite unit vectors. Given a single frequency receiver, user equivalent range error is about 25 m. The position error, for the best minimum satellite solution, would be about 43.3 m.

A commercially available 6U CubeSat buses from Innovative Solutions In Space (ISIS), Blue Canyon Technologies (BCT), Tyvak, or GOMSpace ("GOMSpace 6U Platform," 2020; "ISIS 6U CubeSat," 2018; "Tyvak Platforms," 2020; University, Obispo, & Lab, 2018; "XB6 Spacecraft," 2020), will be compared and used to provide baseline performance. All cases will be explored using nanosatellites, 1-12 kg, without propulsion on-board. As this mission planning system is payload agnostic, nanosatellite payload performance will be derived from area covered as proportional to the data generated for observation missions. Use of the module development will allow for additions of statistical noise interference like clouds or vegetation for optical or radar payloads.

Planet Labs maintains a peak data rate of 220 Mbps and an average of 160 Mbps for 3U CubeSats in X-band (Devaraj et al., 2017). Normal data volume throughput for a 7-10 minute pass is 12-15 GB. The Defense Satellite Communications System (DSCS) provides joint forces with X-band communications. With deployment of the Wideband Gapfiller System (WGS) to support DSCS nominal rates of 900 Mbps are provided (*C4ISR for Future Naval Strike Groups*, 2006).

1.3.2 Aircraft performance

Given an F-35 variant or commercial derivative the performance of the aircraft, or reusable first stage, determines the required performance of the launch vehicle(s). Using energy-height method we can determine the range and capability of the aircraft to deliver the launch vehicles. Additional optimization could be performed provided sophisticated analysis of drop conditions at varying speeds and altitudes. Without such analyses, drop conditions are fixed to the maximum release velocity, $M_\infty = 1.6$, at 38,000 ft for F-35 variants. The commercial derivative will release the launch vehicle at subsonic conditions.

1.3.3 Launch vehicle performance

Satellites will be directly injected into the final orbit by the launch vehicle. Comparisons are made with commercially available systems, Northrop Grumman's Pegasus XL and Virgin Orbit's LauncherOne, to determine the validity of the ΔV necessary for direct injection. Using near-simultaneous launches from airborne platforms will require a Collision On Launch Assessment (COLA) for each launch. If the constellation uses multiple planes and different inclinations to meet coverage demands Conjunction Assessment (CA) may be required for the satellites in the constellation.

Case 1: Extremists take control of PLA Shandong Carrier Strike Group

Figure 1-4. Two J-15's prepare to launch from the PLA Shandong aircraft carrier while the CSG is underway.

Terrorists have taken control of the PLAN Shandong carrier strike group (CSG) during a training exercise and established a defensive perimeter up to 300 mi. The rogue terrorist group has announced their intention to launch a ballistic missile at US civilian populations in Hawaii unless their demands are met.

This case represents a dynamic solution; highly constrained in time. The solution is to provide persistent coverage overhead with Link 16, to provide terminal guidance to a net-enabled weapon to destroy the terrorist threat. We can examine the solution of tracking a moving target, the effect of launch window on viewing time, power-constraints on the satellites, and the effect of different launching locations.

Case 2: Continuous coverage during Freedom of Navigation Operation

Figure 1-5. Artificial island, Mischief Reef, build-up including SAM batteries, radar, communications, and EW capabilities ("A Look at China's SAM Shelters in the Spratlys," 2017; "Updated: China's Big Three Near Completion," 2017). SAM batteries under-construction are shown on the right.

USN DDG-88 and DDG-111, Preble and Spruance, are conducting innocent passage within 12 nautical miles of Mischief Reef in a Freedom of Navigation Operation (FONOP). Spoofing of GPS signals, (Harrison et al., 2020; Weeden & Samson, 2020) can make navigation dangerous. Continuous coverage via SAR and EO/IR imagery of Mischief Reef has been requested for a week prior to and during the FONOP. During the FONOP, satellite navigation (SATNAV) support is requested for the Ship's Inertial Navigation System (SINS) to improve piloting.

This case represents the combined solution of surprise continuous coverage of a fixed point and moving vessels, rapid response, and reconstitution of jammed or disabled satellites in a constellation. ISR is provided to the moving commander in theater and navigation solutions for safety during operations.

Case 3: Humanitarian Aid/Disaster Response

Figure 1-6. USMC F-35Bs prepare to land on the flight deck of the amphibious assault ship USS Makin Island (LHD 8) (Crosley, 2020).

Typhoon Vamco made landfall 11 November 2020 ten days after super typhoon Goni made landfall along the same path in the Philippines. Search and rescue efforts were hampered by communication and electricity outages. The Makin Island Amphibious Ready Group (ARG) is directed to provide humanitarian aid and disaster relief. Surge capability for the DSCS and SA of the disaster region is provided via rapid responsive launch.

Timely comparisons of satellite mapping with SAR from Sentinel and CYGNSS or Spire, optical from Maxar, Planet, and NASA can provide critical ISR to disaster response teams. Providing SAR and optical ISR to disaster response teams on the ground in an hour will help

teams make critical decisions about how to distribute support and aid, making potentially life-saving decisions for those affected.

Case 4: Rapid science return

HMS Queen Elizabeth CSG is performing a joint NATO exercise in the Norwegian Sea during July. An Arctic cyclone, projected to match the Great Arctic Cyclones 2012 and 2016, is predicted 3 days out (Doyle et al., 2019). Atmospheric forcing may cause hazardous ice, weather, and sea conditions for the exercise participants and international shipping.

This represents an opportunity to demonstrate interagency collaboration on providing meteorological returns to the joint force and continuing science return until de-orbit. Meteorological and ISR return may require distributed communications via terrestrial and orbital systems to surface ships underway. Taking advantage of unique polar orbits will be an interesting case.

2. LITERATURE REVIEW

Distributed small satellite systems represent redundancy and significant cost reduction in mission objective and science return but face priority deployment concerns. Often smaller satellite systems must ride-share with a primary mission for the launch vehicle. Coverage prediction and performance have been considered since 1957. Only recently has much attention been given to the agile satellite problem or changing mission objectives already on-orbit. Most of the attention has been focused on Earth Observation (EO) objectives.

The rapid constellation deployment, just like the agile constellation, is a scheduling problem. Classic scheduling and/or routing problems such as the Traveling Salesman Problem and its variants and artificial intelligence/machine learning techniques have been used to attack the agile satellite problem. Similar approaches and constraints used to solve routing and scheduling problems will also be considered.

Airborne launch vehicles have been fielded since 1959. Only with the resurgence in small satellite systems has more attention been given to their development and rapid launch capabilities. Rapid launch is seen primarily as a replenishment or reconstitution provider for constellations already on-orbit.

2.1 Distributed satellite systems

Small satellites, in the micro- and nanosatellite range, 10-100 kg and 1-10 kg, respectively, have enabled numerous missions to replace monolithic systems with distributed satellite systems. Micro- and nanosatellites cost significantly less, ~$1M, meaning that current

spacecraft can be replaced with multiple small satellites ensuring graceful degradation of missions and improved science return.

2.1.1 Applications

Distributed satellite systems are a space system allocating functionality among multiple spacecraft that interact to achieve desired goals (Selva, Golkar, Korobova, Lluch i Cruz, & Weck, 2017). This broad definition includes concepts allocating program-level, mission-level, or spacecraft-level functionality, which may be owned and operated by one or more organizations. Out of the units this functionality is allocated to; focus is devoted to constellations and formations. Swarms and clusters are subcategories of a formation. Minimal attention is given to fractionated spacecraft, and federated systems because their spacecraft-subsystem-level functionality is out of scope but they should be included and/or considered for commercial market applications.

Constellations are those distributed satellite systems with high degrees of homogeneity and physical separation but low functional and operational interdependence. Global Positioning System (GPS) satellites are homogenous and operate in six equally-space orbital planes with a minimum four slots, satellites, per plane arrangement. GPS satellites transmit coarse acquisition or pseudo-ranging based on their internal clock and systems with occasional updates from distributed ground stations. They are independent of one another for operation (Defense, 2007, 2020; Renfro, Stein, Reed, Morales, & Villalba, 2019; Transportation, 2008, 2020).

Trains will be treated as a constellation for the purposes of this paper despite their lack of homogeneity and increasing functional interdependence. Trains are different spacecraft operating in a similar follow-on orbit for mutual science benefit but do not share the same primary mission goal. The A-Train is a collection of individual Earth science satellites, including the CloudSat,

Aqua, Aura, Calipso, and Parasol satellites. Some of these may have de-orbited or been demoted from the train to preserve the other satellites by time of publication. CloudSat and Calipso's data products have combined for a greater understanding of hydrological cycle, cloud-scale physics, and formation of major storm systems on Earth (Stephens et al., 2002; Stephens et al., 2018).

Formations are distributed satellite systems with high degrees of homogeneity, functional, and operational interdependence with a low degree of physical separation. Gravity Recovery And Climate Experiment (GRACE) uses two identical satellites to measure gravity gradients and map Earth's gravity. Each GRACE satellite carries a precise microwave ranger that determines the change in distance from the 220 km along-track separation (Kim & Lee, 2009; Kim & Tapley, 2005; Ko, Tapley, Ries, & Bettadpur, 2012; Lee & Choi, 2011; Tapley, Bettadpur, Ries, Thompson, & Watkins, 2004). TerraSAR-X add-on for Digital Elevation Measurements (TanDEM-X) also uses two identical satellites to operate as a large single-pass radar interferometer to provide near-global digital elevation models. Using the node line angle, angle between perigees, orbit eccentricities, and phasing between satellites, a helix-like relative movement of the satellites is used to provide baseline sythenthic aperture interferometry (Krieger et al., 2007; Montenbruck, Kahle, D'Amico, & Ardaens, 2008). As of 2016, 39 nanosatellite constellation and formation flying missions were to fly or had flown (Chung, Bandyopadhyay, Foust, Subramanian, & Hadaegh, 2016).

From an operational and potential market standpoint, current trends like fractionated systems and decentralization of ownership are interesting notional concepts. Fractionated systems divide traditional functionality of a spacecraft among multiple assets that coordinate to achieve mission goals. Functionality includes measurements, power, communication, data processing, navigation, etc. Decentralization of ownership includes concepts on-orbit such as

hosted payloads and federated satellite systems. A federated satellite system seeks to share unused capacity in a network to increase computing performance on-orbit. Hosted payloads are customer payloads flying on the host organization's spacecraft paying for resources consumed. A standard bus could provide a hosted commercial or military payload a rapid launch capability via airborne launch.

2.1.2 Market

SpaceX's Falcon 9 is the first orbital class rocket capable of reflight. SpaceX's goal in 2019 was to demonstrate two orbital launches of the same vehicle within 24 hours while already having reflown 15 times (as of August 2018) (Smith, 2018; Wall, 2018). This schedule flexibility coupled with the 30% reduction in price for reused first stage flights (Smith, 2018) is a competitive advantage. Constellation replenishment and/or fulfillment experiences the cost benefits of rapid launch schedules. Planet annually replenishes its constellation with 50-100 satellites, Iridium cyclically replacing its 77 satellites, and SpaceX building its 12,000 satellite constellation with 60 satellites at a time. SpaceWorks analysts projected between 294 to 393 nano/microsatellite launches in 2019, an increase of 18% from 2018. 253 of the 262 small satellites SpaceWorks predicted launched in 2018 (*NANO/MICROSATELLITE MARKET FORECAST*, 2020).

Small satellites are of increasing interest to commercial, government, and academia because of their reduced complexity and resulting cost improvement (Bille & Lishock, 1998; Boll, 2016; Gunter & Maessen, 2010; Iwata & Venturini, 2016; Shao, Koltz, & Wertz, 2014). An increase in performance, reduction in mission cost, lower risk, and shorter schedules are possible by using multiple small satellites at lower altitudes when compared to traditional systems (Shao et al., 2014; Xue, Li, Guang, Zhang, & Guo, 2008). Larger satellites reflect the trend in satellite

production towards redundant systems, highly reliable components, and in the case of military applications, defensive countermeasures. Smaller satellites address these requirements by an increase in numbers enabled by a decrease in production cost. Small satellites often fill the gap in testing novel technologies and systems. Over 20 countries have entered the space community using small satellite launches (*Space Mission Analysis and Design*, 2003). Frost & Sullivan predict the small satellite launch market to exceed $62 billion by 2030 because of demand by commercial constellation operators (*Small-Satellite Launch Services Market, Quarterly Update (Q1 2018), Forecast to 2030*, 2018).

Historically, 2015-2019, 51% of nano- and microsatellites, 1-50 kg, have been used for Earth observation and remote sensing missions. The next largest mission use is technology demonstration at 21% (*NANO/MICROSATELLITE MARKET FORECAST*, 2020). Long-term projections indicate as many as 2,400 nano- and microsatellites launched in the next 5 years.

Trends towards dedicated small satellite launch vehicles reflect the market's attempt to take advantage of these upcoming small satellite launches. Despite this growth, more than 75% of nano- and microsatellite operators chose to leverage rideshare alternatives in 2019. Arianespace and SpaceX have begun to offer low-cost rideshare opportunities to enter the market space of dedicated small satellite launch providers (*NANO/MICROSATELLITE MARKET FORECAST*, 2020). SpaceX's base price for rideshare opportunities is $1 million and $5,000 extra per kilogram over 200 kg (Erwin, 2020). RocketLab a dedicated small satellite launch provider has a base price of $5.7 million for a dedicated launch (Etherington, 2020).

2.1.3 Modularity

The modularity of nanosatellites, especially CubeSats, has led to satellite developers and designers building standard satellite buses to host payloads. The 6U CubeSat standard

(University et al., 2018) lists the maximum mass of a 6U CubeSat at 12.00 kg where the materials used are to have a total mass loss less than or equal to 1.0%. The center of gravity shall be located within 4.5 cm from geometric center in X, within 2.0 cm from geometric center in Y, and within 7.0 cm from geometric center in the Z direction. The center of gravity location for the standardized CubeSat bus will determine the maximum angular rate applied for slewing maneuvers.

The Innovative Solutions In Space (ISIS) offers a basic and advanced satellite bus to operators ("ISIS 6U CubeSat," 2018). This modularity allows payload designers to focus on optimization and improvement of the science return. Blue Canyon Technologies (BCT) ("MICROSAT SPACECRAFT: X-Sat," 2020; "XB3 SPACECRAFT," 2020; "XB6 Spacecraft," 2020; "XB12 SPACECRAFT," 2020), Clyde Space ("AAC Clyde Space," 2019), Pumpkin (*6U SUPERNOVATM Structure Kit: Owner's Manual*, 2014; "MISC 3™ 3U nanosatellite Bus Hardware Revision: A," 2014), Tyvak ("Tyvak Platforms," 2020), and GOMSpace ("GOMSpace 6U Platform," 2020) also offer standard CubeSat buses for operators. NASA Goddard Space Flight Center built Dellingr, a 6U CubeSat bus, to provide experience in non-traditional satellite development and achieve planetary science objectives (Goodloe et al., 2017; Keesey, 2017; Kepko et al., 2017; Kepko et al., 2018).

Table 2-1. Advanced commercially available CubeSat 6U form factor buses.

Commercially Availabe 6U CubeSats					**Units**
Corporation	Tyvak	GOMSpace	ISIS	BCT	
Payload Mass	3	6	5.5	8	kg
Payload Volume	3	4	2.5	4	U
Payload Peak Power	180	48	20	140	W
Onboard Data Storage	128	0.032	64	8	GB
Uplink COMM	UHF, S-Band	UHF	VHF, UHF	S-band, X-band	

Downlink COMM	UHF, S-Band, X-Band	UHF	VHF, UHF, S-band	S-band, X-band	
C&T Tx Min	9.60E+03	1.00E+02	1.00E+02	1.00E+02	bps
C&T Rx Min	1.00E+02	1.00E+02	1.00E+02	1.00E+02	bps
Data Rate Min	2.00E+06	1.00E+02	1.00E+02	1.00E+02	bps
C&T Tx Max	2.00E+06	3.84E+04	9.60E+03	2.50E+07	bps
C&T Rx Max	1.25E+05	3.84E+04	9.60E+03	1.00E+05	bps
Data Rate Max	5.00E+07	3.84E+04	3.40E+06	2.50E+07	bps
Data Interfaces	RS-422, Ethernet	I2C, UART, CAN	I2C, UART, CAN, SPI, USART	Serial, LVDS, Spacewire, HDLC, SPI	
Propulsion Min	10.00	588.60	0		m/s
Propulsion Max	300	1079.1	0.00E+00		m/s
Position Knowledge	5.00	0.1		4	±m
Velocity Knowledge		0.005		0.05	±m/s
Pointing Accuracy		1	0.1	0.002	±°
Pointing Stability			1.85E-05	0.000277778	±°/s

Klofas, as of 23 Nov 2018, has compiled a list of communication frequencies and protocols used by CubeSats and the type of user, University/Commercial/Government (Klofas, 2018). Most CubeSats rely on patch or dipole antennas but RainCube, built on a Tyvak bus, and ISARA, built using JPL and Pumpkin, Inc., used a parabolic deployable antenna and a reflectarray antenna. Earth observation and remote sensing missions have designed CubeSats to use inflatable, deployable, reflectarray, and rib reflector antennas (Chahat et al., 2016; Gao, Rahmat-Samii, Hodges, & Yang, 2018).

The modularity of CubeSats, payload miniaturization, and resiliency of small satellites has forced constellation and systems engineers to consider CubeSats in the initial design stages. The design options are to distribute the payload across members of the distributed satellite system, see synthetic aperture (Chung et al., 2016; Gogineni et al., 2018; Krieger et al., 2007),

miniaturize the payload and deploy more satellites (Chahat et al., 2016; Chew et al., 2018; Chew & Small, 2017; Gao et al., 2018; Masters, 2018; Ruf et al., 2018; Werner, 2020), or combine both approaches. Having a standard satellite bus available for payload integration reduces development time and lends itself to all three approaches.

2.1.4 Operations

Optimal satellite operations depend upon the level of Space Situational Awareness (SSA) enjoyed by the operator. The Combined Force Space Component Command (CFSCC) a subordinate command of the United States Space Command (USSPACECOM) is responsible for identifying, cataloging, and tracking over 23,000 man-made objects achieving orbit. CFSCC uses data collected by the Space Surveillance Network (SSN) and the expertise of its personnel at the Combined Space Operations Center (CSpOC) to execute its mission. CSpOC is a strategic defense partnership between the United States, Canada, Australia, and the United Kingdom with participation by Germany, France, and New Zealand (Armstrong, 2019). The United States Space Force (USSF) 18th Space Control Squadron (18 SPCS) maintains the US catalog and provides space flight safety support on behalf of USSPACECOM (Administration, 2020). “The 18th SPCS monitors approximately 3,200 active satellites for close approaches with approximately 24,000 pieces of space debris, and issues an average of 15 high-interest warnings for active near-earth satellites, and 10 high-interest warnings for active deep-space satellites, each day,” (Chiles, 2020).

The proliferation of CubeSats and nanosatellites pose unique tracking and identification challenges. CSpOC has and continues to provide guidance to operators on how to achieve optimal operations. CSpOC provides guidance to operators through a data-sharing agreement for telemetry of the CubeSat. 18 SPCS shares SSA information with more than 100 governmental,

academic, and commercial partner organizations from 25 nations through formal SSA data sharing agreements, and www.Space-Track.org (Chiles, 2020). Detailed launch plans and payload deployment help CSpOC quickly and efficiently categorize objects. If objects are unable to be categorized, they are classified as “analyst satellites,” which are not publicly releasable ("JSpOC Recommendations for Optimal CubeSat Operations," 2015).

SSA is the ability to accurately characterize the space environment and activities in space. Civil and military SSA combine state information, trajectory of objects in orbit using mainly optical telescopes and radar, with information on space weather. Military SSA is additionally tasked to characterize objects in space, capabilities, limitations, and potential threat. Within NASA, the Human Space Flight Operations Directorate of Johnson Space Center provides conjunction risk analysis support to the International Space Station, vehicles visiting the ISS and Artemis space flight missions from the console positions, Trajectory Operations Officer (TOPO) and Flight Dynamics Officer (FDO). The TOPO group is the sole liason to USSPACECOM and USSF for trajectory maintenance and orbital safety of human space flight assets (Administration, 2020; Chan, 2008). CFSCC and CSpOC actively monitor NASA human space flight missions to provide recovery trajectory tracking, rescue support through Task 45 Assigned Contingency Rescue Support, and provide Space Domain Awareness to spacecraft and mission partners via sensor tasking, on-orbit screening, confirmation of status, and conjunction analysis (Allison, 2020).

SSN includes both ground-based radar and optical instruments. The SSN is used by CSpOC to maintain the catalog of space objects. The catalog supports commercial, civil, military, and intelligence spaceflight safety and applications. Essentially, the SSN through global and orbit-based network collects data on objects. CSpOC converts this into actionable items

through orbit determination. Objects in the catalog are refined and any new objects are added (Weeden, 2017).

Table 2-2. Current and past sensors in the United Space Surveillance Network (SSN).

Sensor Name	Sensor Category	Sensor Type	Sensor Mission	Operational
GEODSS SOCORRO	Dedicated	EO	DS	Y
GEODSS TAEGU	Dedicated	EO	DS	N
GEODSS MAUI	Dedicated	EO	DS	Y
GEODSS DIEGO GARCIA	Dedicated	EO	DS	Y
ALCOR	Contributing	MTR	NE	Y
ALTAIR	Contributing	MTR	DS	Y
TRADEX	Contributing	MTR	NE and DS	Y
MMW	Contributing	MTR	NE	Y
PIRINCLIK	Collateral	MTR	NE and DS	N
FYLINGDALES	Collateral	PAR	NE	Y
CLEAR	Collateral	PAR	NE	Y
ASCENSION	Contributing	MTR	NE	Y
ANTIGUA	Contributing	MTR	NE	N
MILLSTONE HILL	Contributing	MTR	DS	Y
MILLSTONE UHF	Contributing	MTR	DS	N
HAYSTACK	Contributing	MTR	NE and DS	Y
GOODFELLOW	Collateral	PAR	NE	N
ROBINS	Collateral	PAR	NE	N
CAPE COD	Collateral	PAR	NE	Y
BEALE	Collateral	PAR	NE	Y
COBRA DANE	Collateral	PAR	NE	Y
THULE	Collateral	PAR	NE	Y
PARCS	Collateral	PAR	NE	Y
EGLIN	Dedicated	PAR	NE and DS	Y
NAVSPASUR	Dedicated	RIF	NE	N
KAENA POINT	Contributing	MTR	NE	Y
MOTIF	Dedicated	O	DS	Y
AMOS	Contributing	O	DS	Y
SBSS	Dedicated	EO	DS	Y
HEH (C-BAND RADAR)	Dedicated	MTR	NE and DS	Y
SST	Dedicated	EO	NE and DS	Y
GSSAP	Dedicated	EO	NE and DS	Y
SAPPHIRE	Dedicated	EO	DS	Y
GLOBUS II	Dedicated	MTR	NE	Y
SPACE FENCE (S-BAND)	Dedicated	PAR	NE and DS	Y

PAR	Phased-Array Radar	DS	Deep-Space
MTR	Mechanical-Tracking Radar	NE	Near-Earth
RIF	Radar Interferometer		

O	Optical sensor
EO	Electro-Optical sensor

Table 2-2 was compiled from (Berger, Moles, & Wilsey, 1992; Weeden, 2017) on publicly released information regarding the SSN. The DS or NE classification is made based on the orbital period to use the correct orbit model. Orbits where $P \geq 225$ minutes are classified as DS. HEH and SST were relocated to Australia to fill a gap in Southern Hemisphere coverage for the SSN. GSSAP, SAPPHIRE, and SBSS are space-based dedicated observation platforms.

With over 23,000 tracked objects in the public catalog, sensor management to maintain SSA is an important optimization task. In 1992, when the SSN tracked approximately 6,000 man-made objects, CSpOC used 32 Gabbard classes to divide the satellite population according to perigee and apogee altitude to classify satellites for tasking. (Berger et al., 1992). Dividing the population allowed USSTRATCOM at that time to set no observational requirements on Gabbard classes 19-32, technically deep-space by their classification of $P \geq 225$ minutes. Those classes, 19-32, were all lower than 35,786 km, GEO, $1800 > P > 1100$ minutes , or parabolic. This freed up DS sensors to focus on higher priority payloads, rockets, or debris. While the Gabbard classes do not appear in the redacted Strategic Directive (SD)505-1 V1 or V2 from 2004, the same tasking categories, foreign launch, debris event, etc., appear with changes to the observation quantity requirements for each tasking (*Strategic Command Directive (SD)505-1 VOL 1 Space Surveillance Operations - Basic Operations*, 2004; *Strategic Command Directive (SD)505-1 VOL 2 Space Surveillance Operations - Event Processing*, 2004).

Known challenges to CSpOC processes include multiple launch and multiple payload identification. The Operationally Responsive Space (ORS) 3 mission launched on 01:15:00 UTC 20 Nov 2013 from Wallops, launching Space Test Program SATellite (STPSAT) 3 and 27

CubeSats, followed by a Dnepr launch on 07:10:16 UTC 21 Nov 2013 from Dombarovsky with 32 satellites including 31 CubeSats presented these known challenges. CSpOC depends on Owner/Operators (O/Os) to provide detailed information regarding launch plans and payload deployment to ensure individual payload(s) are quickly identified upon separation or release from the payload deployer ("JSpOC Recommendations for Optimal CubeSat Operations," 2015). Performance is directly correlated to object density on sensors' focal planes and average measurement prediction accuracy by tracks (Mori, Chang, Chong, & Spain, 1988; Peng & Bai, 2018).

Space News's provocative article, "1 in 5 CubeSats Violates International Orbit Disposal Guidelines," (de Selding, 2015), a summary of "A Review of Space Environment Implications of CubeSat Traffic, 2003-2014," by Anz-Meador, P. (Anz-Meador, 2015) is misleading. Anz-Meador made the following assumptions, there existed no on-board propulsion for disposal at end-of-life, and all CubeSats mission lifetimes were 2 years. The debris population currently catalogued is limited by SSN capabilities and tasking time. Debris must be associated with a particular track, an object, to be published in the public catalog. Debris at a diameter of up to 10 cm is the limit of current capabilities (Stokes et al., 2003; Thompson, 2015).

A pursuit-evasion game was used as a model by Chen et al. for the low-high satellite tracking case to compare greedy algorithms for total information gain to algorithms that maintain the estimation covariance at a certain criterion (Chen, Chen, Shen, Blasch, & Pham, 2010). The 2D plane pursuit evasion game between a single observer and target where complete knowledge is known to both players, the thrust angles of the pursuer and evader must be the same for the target to evade the observer (Isaacs, 1965). An intelligent target in the 3D case should choose its

maneuvering onset time as soon as the predicted observer's orbital trajectory creates an occlusion by the Earth.

Given two satellites in the same orbital plane with thrusting capability, their polar motion is described in the body frame by Eqns. (2-1) and (2-2) where α is the thrust vector angle.

$$\hat{e}_r : -\frac{\mu}{r^2} + \frac{F \sin\alpha}{m} = \ddot{r} - r\dot{\theta}^2 \tag{2-1}$$

$$\hat{e}_\theta : \frac{F \cos\alpha}{m} = 2\dot{r}\dot{\theta} + r\ddot{\theta} \tag{2-2}$$

The type of observation available, i.e. range-rate measurement, can improve the average detection delay of the target maneuver significantly, reducing the peak estimation errors in position and velocity as shown by Chen et. al (Chen et al., 2010). The observations possible to the observer are

Range $$\bar{\rho} = r_b \hat{e}_{r_b} - r_a \hat{e}_{r_a} \tag{2-0-3}$$

Range-rate coplanar: $\dot{\bar{\rho}} = \dot{r}_b \hat{e}_{r_b} - \dot{r}_a \hat{e}_{r_a} + r_b(\dot{\theta}_b - \dot{\theta}_a)\hat{e}_{\theta_b}$
general case: $\dot{\bar{\rho}} = \dot{r}_b \hat{e}_{r_b} - \dot{r}_a \hat{e}_{r_a} + \omega_{b/a} \times \bar{r}_b$ (2-0-4)

Elevation $$\text{El} = \text{acos}\left(\frac{\bar{\rho} \cdot \hat{e}_{\theta_a}}{\rho}\right) = \text{asin}\left(\frac{z_t}{\rho}\right) \tag{2-0-5}$$

Azimuth $$\text{Az} = \text{acos}\left(\frac{y_t}{\bar{\rho} \cdot \hat{e}_{\theta_a}}\right) = \text{asin}\left(\frac{x_t}{\bar{\rho} \cdot \hat{e}_{\theta_a}}\right) \tag{2-0-6}$$

where $(x, y, z)_t$ are expressed in the topocentric frame centered at satellite a, the observer. Chen et al. demonstrate an improvement in the model switching tracker based on maneuvering detection over the multiple model estimator assuming random maneuvering onset time. Sensor assignment based on maximum information gain can lead to large tracking error for evasive targets. Using the covariance error constraint for all targets alleviates the issue at the price of more frequent revisit time. The compromise of using covariance control for maneuvering targets and maximum information gain for non-maneuvering achieves a reasonable trade-off where complete knowledge of the observer's and target's state is known. The nonlinear filter does not

account for clutter or closely spaced targets causing imperfect data association (Chen et al., 2010).

Prior to launch each mission performs a Collision On Launch Assessment (COLA), screening through the possible modeled launch vehicle trajectories, including separated stages for collisions. The standard COLA involves determination of conjunctions between launched objects and objects in the US catalog of resident space objects. Miss distance and probability of collision are computed and given go or no-go status based on the tolerance of risk. Versions of this process implemented are available from CSpOC, The Aerospace Corporation, and (Gist & Oltrogge, 1999; *Space Safety and Mishap Prevention Program*, 2014). Jenkin et al. established additional screening methods for the International Space Station from the end of COLA screening until launch object orbits have been determined (Jenkin, McVey, & Peterson, 2012).

The 18th Space Control Squadron (18 SPCS) provides screening for all U.S. launches against the space object catalog maintained by the 18 SPCS at CSpOC. Physical separation windows vary from 250, 25, and 2.5 km for manned, active satellites, and debris. In the case of active satellites and debris Probability of collision (Pc) is used. Launch providers must give the 18 SPCS covariance information and size (in meters) of the launch vehicle, and any other launched objects for which screening is desired to screen against Pc. Pc is limited to 1.0×10^{-5} for both active and debris space objects in the catalog (*LAUNCHCONJUNCTION ASSESSMENT HANDBOOK: 18 SPCS Process for Launch Conjunction Assessment*, 2018).

Probability of collision and expected miss distance vary based on the initial formulation of the encounter. In short-term encounters approximations can be made to linearize and simplify the conjunction assessment. In long-term encounters such as formation flying and geostationary satellites these approximations cannot be made. A guide to both the formulation and determining

the risk to or from a constellation is examined by Chan et al. and Chobotov et al (Chan, 2008; Chobotov, Herman, & Johnson, 1997). Non-actionable situations from 18 SPCS conjunction assessments occur when an object whose state has been propagated longer than the orbit determination fit-span to reach time of closest approach. This object is insufficiently tracked and over-propagated, therefore not suitable for mitigation action decisions (Administration, 2020).

Aviation restrictions during launch operations designate a large area following the launch vehicle trajectory from flight path up to an altitude of 30 nmi. During Falcon 9 launches no-fly restrictions were active seven hours prior to launch and up to 30 minutes after launch. Dynamic rerouting of aircraft under risk tolerance during space lift operations was examined by Bojorquez et al (Bojorquez, Dolan, & Chen, 2020). Day of launch for space lift operations includes trajectory optimization given vehicle's structural constraints, loading, and environmental conditions. Six hours before lift-off weather balloons are released near the launch site to measure wind and other atmospheric conditions. Weather balloons released are considered in COLA operations to ensure successful launch without fear of collision (Harrington, Picka, & Cordova, 2011).

Currently, CSpOC provides conjunction warnings to all satellite operators that provided contact information. Other operators have taken it upon themselves, following the Iridium-Kosmos collision in 2009, to share operational data and promote best practices by forming the Space Data Association. The Space Data Associations current list of challenges include inter-system biases in operator flight dynamics systems, limitations in the availability and accuracy of data related to debris and non-member satellites, and lack of consistent availability of government data (Cacioni, 2018). Decisions to maneuver are often made with the balance of

mission lifetime sustainment and operational knowledge requiring on-call capability (Symonds et al., 2014).

Orbit determination is important in gravity field model refinement, decay and modeling of satellite orbits, and accurate assessments of satellite coverage. Satellite-to-satellite tracking in two-way range and range-rate estimates indirectly incorporate the relay satellite's state estimation error. Incorporation of the relay satellite's state estimation error was demonstrated in the ATS-6/GEOS-3 and the ATS-6 and NIMBUS-6 satellite-to-satellite orbit determination experiments and operationally in the Tracking and Data Relay Satellite System (TDRSS) (Fang, 1979; Vonbun, Argentiero, & Schmid Jr., 1978). Non-cooperative objects require illumination of the target for optical tracking measures or a large enough cross-sectional area to deliver a return to a radar system. Orbit determination of illuminated objects from overhead platforms, high-to-low tracking, can be especially useful when determining timing necessary to shield delicate sensors from being saturated (Bate, Mueller, & White, 1971; Osedacz, 1989). Precise state estimation in position is achievable in centimeter level knowledge when using carrier differential GPS (Bonin et al., 2015; Busse, 2003).

Due to the stochastic nature of the atmosphere and complexity of drag modeling for a spacecraft any deterministic analysis of spacecraft lifetime will have a large confidence interval. Uncertainty quantification of the lifetime estimation from the dominant sources of uncertainty, drag and environmental forces, are considered by Dell'Elce et al. using a 2U CubeSat (Dell'Elce et al., 2015). The probability density function in this case for the lifetime uncertainty was right-tailed extending from a few hours to over 200 days with an expected value just under 100 days.

Formation flying missions attempt to not only control orbital position but also their relative configuration with high accuracy to accomplish mission goals. Autonomous robust and

reliable GNC poses two main challenges. Miniaturization of satellite hardware and optimal-fuel and computationally efficient GNC algorithms (Chini, Giambene, & Kota, 2009; Di Mauro, Lawn, & Bevilacqua, 2018; Vikan, 2011). Current projected and past missions from 2000 to 2025 expect 32.4% of formation flying missions to be nanosatellites. CanX-4 and CanX-5 demonstrate centimeter-precision formation flight from 1 km to 50 m range separation using carrier-phase differential GPS techniques. GNC algorithms and inter-formation networking can be tested on Unmanned Aerial Vehicles (UAVs) due to the miniaturization of hardware. Marshall Space Flight Center has tested inter-formation networking using Time Division Multiplexed Architecture (TDMA) to enable relative positioning of satellite formations (Becker & Merrill, 2017a, 2017b; Merrill, 2016; Merrill & Becker, 2015). UAVs were used as a satellite proxy to test the networking and autonomous capabilities of the software.

Telemetry and ground station systems must be considered prior to launch. In some cases, GPS position information may be enough for the satellite. In others, tracking should occur often with systems designed to maintain precise position information. Frequency allocation, the availability of ground stations, and link budgets must be considered to relay the science return from the nanosatellite to the ground (Chandrasekaran, Stewart, & Murphy, 2004; Diaz, 2017; Gao et al., 2018; Malphrus et al., 2010; Schor, Kinsner, & Thoren, 2009; Christopher R. Simpson, 2017; Tuli, Orr, & Zee, 2006).

2.2 Coverage Prediction

Coverage drives satellite, constellation, and orbit decisions. Coverage is the common denominator in decisions for orbit, attitude control, and the number of nanosatellites. This includes determining the orbit to within some degree of certainty within the bounds of coverage, different inclined planes, and lifetime.

2.2.1 Constellation Design

Analytical methods of constellation design often focus on global coverage. Special cases are applied for determining coverage at latitude. Methods focus on spherical geometrical analysis of passes. Coverage analysis is often performed using commercially available orbital propagation and simulation software, such as Systems Tool Kit (STK), or FreeFlyer ("FreeFlyer," 2019). Selecting the right orbit is critical to mission success. The right orbit is often a balance between power requirements, view times, and downlink availability. Requirements are specified in terms of area of interest, frequency, and duration. The time interval requested from one view to the next is the gap duration or revisit time.

Analytical methods for developing global coverage include the Walker constellation, featuring satellites in varying planes and spacing within those planes at the same inclination (Walker, 1970, 1971, 1977, 1982b). The Walker constellation is a starting point for most constellation designers to provide continuous global coverage. Walker constellations feature the notation $T/P/F$, where T is the total number of satellites, P, is the number of planes, and F is a non-dimensional measure of satellite relative spacing, or phasing, in different orbital planes. The Rosette constellation design features some of the same points as the Walker constellation, including multiple planes, inter-plane phasing, and differing altitudes to affect continuous global coverage but unnecessarily restricts retrograde orbits (Ballard, 1980; Walker, 1982a).

Walker, Mozhaev, Ballard, and Lang (Ballard, 1980; Mozhaev, 1972, 1973; Walker, 1970, 1971, 1977, 1982a, 1982b) examined constellations in common-altitude, generally inclined, circular orbits providing continuous global coverage for a minimum of satellites. Chobotov (Chobotov et al., 2002) suggests using a common access area for a satellite, constellations could be designed by combining single satellite coverage with multiple streets,

great circles from swath width, of coverage. Continuous global coverage is ideal for Global Positioning Satellites (GPS). In-theater coverage or point target observations may necessitate specific viewing angles, increased revisit time, or lower altitudes to provide improved resolution that a global constellation cannot provide.

Coverage analysis, revisit metrics for EO and DoP for PNT is numerically determined using commercially available software. Analytical approximations of coverage, such as those by Wertz (Wertz, 2011), assume a spherical Earth. Given Eq. (2-7), the longitude of all passes, λ, for each nodal period is determined, and each longitude at latitude, ϕ, satisifying the inequality, Eq. (2-8), is viewable by the satellite given a sensor with a longitudinal coverage, $\Delta L(\phi)$.

$$\lambda = \lambda_0 - (j-1)P_n\omega_\oplus \text{ for } j = 1, 2, 3 \ldots \left|\frac{t_{analysis}}{P_n}\right| \tag{2-7}$$

$$\lambda_\phi - \lambda_P \leq \Delta \text{L} \tag{2-8}$$

Wertz provides a coverage analysis example (Wertz, 2011) to explain how we might select the right circular orbit for coverage from a single satellite. Analytically, it can be determined that for a circular orbit at an altitude of 850 km and an inclination of 65°, approximately 60% of the time, Haiti can be observed while in communication with Wallops Island. An example of this coverage calculation is described in detail for the South China Sea in Appendix B. A numerical example from CYGNSS (Ridley, 2015) determined coverage statistics by binning regions of interest to measure gap statistics in desired regions, in their case along the equator for tropical cyclone measurements by GNSS-reflectometry.

Continuous optimal coverage in LEO of point targets is examined in Sugrue and Rendon (Rendon, 2006; Sugrue, 2007). Sugrue extends spherical analytical coverage for determination of optimal orbits to build coverage of in-theater targets. Rendon determined the variation of inclination and eccentricity to increase the number of daylight passes for given point coverage by

single satellites. Crisp et al. (Crisp et al., 2018) extends the analytical coverage prediction by Sugrue to focus on revisit time for Walker delta constellations and compares performance with commercial software.

Repeating ground track orbits can be designed to meet specific coverage criteria. At critical inclinations (63.4/116.6 deg) constellation designers will have to incorporate growth of eccentricity growth for orbits with almost fixed inclination (Lara & Russell, 2008). Lara and Russell (Lara & Russell, 2008) demonstrate how to automate the process of designing for repeating ground tracks. Formation missions can be designed in a similar manner to take advantage of J_2 secular perturbations for interferometric or SAR observations (Fasano & D'Errico, 2006). The primary challenge to formation missions is the design of robust and reliable onboard Guidance, Navigation, and Control (GNC) (Di Mauro et al., 2018).

2.2.2 Scheduling optimization

Constellation design is primarily driven by scheduling requirements. With delayed and long-term launching cadence for constellations commonplace agile constellations, or constellations able to redesignate targeted observations on-orbit are of interest to operators. Agile satellite mission scheduling and agile constellations have been covered extensively in literature. While rapid space lift or agile launch has not been covered, problems that could be modified to be applied to space lift or agile launch have been covered. Optimization of Emergency Medical Service (EMS) locations in cities, single-agent scheduling with constraints such as deadline or precedence condition for optimal solutions, and multiple Earth observation satellite scheduling problems provide useful analogues for building the rapid launch scheduling problem.

The problem of schedule optimization is generalized or converted into more common problems such as the knapsack, dynamic programming, constraint programming, network flow,

or the single-machine scheduling problem (Baek et al., 2011; Bensana, LeMaitre, & Verfaillie, 1999; Cho, Kim, Choi, & Ahn, 2018; Jung-Hyun et al., 2012; Vasquez & Hao, 2001). Schedule optimization using dynamic programming with two levels of heuristics was verified and improved upon using mixed integer linear programming to plan the time-varying full-body orientation of agile CubeSats in a constellation under hardware constraints by Nag et al. (Nag, Li, & Merrick, 2017). Additional work demonstrated 11.3x improvement when using Delay Tolerant Networking for reactive imaging (Nag et al., 2019). Genetic, priority-based, rule-based, simulated annealing, and tabu search algorithms have been proposed for the multiple observing satellite case (Abba, Meselhy, Moughith, & Omer, 2019; Cho et al., 2018; Holvoet, Vongsantivanich, Chaimatanan, & Delahaye, 2018). McGrath et al. (McGrath & Macdonald, 2016) highlighted that analytical expressions may be valuable in addressing the optimized solution for time, fuel, or a cost function combining the two. A survey of the solution space for low-thrust satellite maneuvers showed complexity making optimization challenging, especially where ΔV may not reduce the fly-over time or achieve similar times with different ΔV usage (McGrath & Macdonald, 2016).

The prize collecting traveling salesman problem (PCTSP) is an important class of the scheduling and routing problem. Where the salesman gets a prize w_k in every city k that he visits and pays a penalty p_l for every city l that he fails to visit, and travels between cities i and j at cost c_{ij}. He wants to minimize the sum of his travel costs and net penalties, while including in his tour enough cities to collect a prescribed amount w_0 of prize money. The variable y_i is 1 for every city i included in the tour and 0 otherwise, and x is the incidence vector of the tour, allowing us to formulate the PCTSP on a complete directed graph $G' = (N, A)$:

$$\min \sum_{i \in N} \sum_{j \in N-[i]A} c_{ij} x_{ij} + \sum_{i \in N} p_i (1 - y_i)$$

subject to

$$\sum_{j \in N-[i]} x_{ij} - y_i = 0$$

$$\sum_{i \in N-[j]} x_{ij} - y_j = 0$$

$$\sum_{i \in N} w_i y_i \geq w_0$$

$y_i \in [0,1], i \in N; x_{ij} \in [0,1], (i,j) \in A$

$G'(y,x)$ is a cycle.

The constraints, $\sum_{j \in N-[i]} x_{ij} - y_i = 0$ and $\sum_{i \in N-[j]} x_{ij} - y_j = 0$, tell us that if the salesman is in city i, he must go to one of the other cities, j, and if he is in city i, he must have come from one of the other cities j on the route.

Emergency Medical Services (EMS) can achieve more effective results through optimization of allocation and location decisions. An EMS control center will make decisions on where to deploy ambulances. Ambulance requests can be considered stochastic process and the travel time for the journey, rush hour traffic, may contain randomness. The optimization of the locations of EMS departments and prioritization of care can guide the delivery of EMS to different hospitals and patients (Acuna, Zayas-Castro, & Charkhgard, 2019; Liu, Yang, & Hao, 2017; Zhen, Wang, Hu, & Chang, 2014).

Optimal trajectories can be determined using direct collocation with nonlinear programming. Pontani and Conway made a determination of the optimal, i.e. minimum-time trajectories leading to interception of a repeating ground track LEO satellite by a two-stage ground launched interceptor (Pontani & Conway, 2009). Ignoring atmospheric effects represents the best possible case of minimum-time intercept. Atmospheric effects will degrade performance. The properties of the direct collocation with nonlinear programming are to discretize the continuous problem in time, translate state equations into nonlinear algebraic

equations by means of high-order quadrature rules, and solve the resulting nonlinear programming problem by a numerical optimizer.

Some numerical optimizers available from the Non-Linear OPTimization (NLopt) (Johnson, 2020) library for nonlinear local optimization are the Constrained Optimization BY Linear Approximation (COBYLA) and Bound Optimization BY Quadratic Approximation (BOBYQA). COBYLA is a direct search iterative algorithm useful for those algorithms with no or unknown derivatives. Each iteration forms linear approximations to the objective and constraint functions by interpolation at the vertices of a simplex and trust region bound restricts each change to the variables. Direct search optimizations are "[attempting] to find the deepest point of a muddy lake, given a boat and a plumb line, when there is a price to be paid for each sounding," (Powell, 1994). COBYLA is restricted to small numbers of variables to run with any appreciable amount of time especially as the nonlinearity of the approximated function increases. While BOBQYA is also a direct search iterative algorithm, it employs a quadratic approximation to the objective function. The amount of second derivative information needed is proportional to the rate of convergence. BOBYQA is faster and delivers smaller relative error for those nonlinear problems but it too will take an increasing amount of time as the nonlinearity of the approximated function, especially its derivatives, increase (Powell, 2009).

2.3 Airborne Launch Vehicles

An airborne launch addresses the schedule flexibility by removing the effects of launch range availability, launch pad throughput, and the efficiency of the range to reset between launch events. The schedule is reduced to loading the payload, loading the launch vehicle, and the flight profile. Air launch has had limited financial success to-date but has experience a resurgence

because of the smallsat market and increased government pressure to develop a rapid launch capability.

2.3.1 History and Development

Airborne launch vehicles have been tested and developed since the launch of Sputnik in October 1957. In response, the Naval Ordance Test Station (NOTS) China Lake, California, now Naval Air Warfare Center – Weapons Development (NAWCWD) China Lake, began development of an airborne launch vehicle to deliver military satellites in a timely manner or intercept adversarial ones. NOTSNIK (Bille & Lishock, 2002; Lawson, 2017), the NOTS-EV-1, was an all solid five-stage booster carried on a Douglas F4D-1 Skyray. Six launch attempts resulted in two possible partial successes.

Figure 2-1. NOTS-EV-1 attached to a Douglas F4D-1 Skyray at NOTS China Lake, California (Verver, 1958).

The successor to NOTS-EV-1 was NOTS-EV-2 or Caleb. Caleb was used in upper atmospheric testing. It could deliver 85 pounds to 1,000 miles as a two-stage vehicle and 13 pounds to 2,000 miles as a three-stage vehicle. It was dropped from the centerline of a McDonnell-Douglas F4H-1 Phantom. As a satellite interceptor, Caleb was ground launched (Lawson, 2017).

At Edwards Air Force Base and the NASA Flight Research Center, now Armstrong Flight Research Center, sounding rockets were being launched from the centerline of a F-104A

Figure 2-2. F-104A Starfighter shown with the Air Launched Sounding Rocket (ALSOR) attached on December 16, 1959 ("Air Launched Sounding Rocket (ALSOR) Attached to F-104," 1959).

Starfighter the same time NOTS-EV-1 and Caleb were being developed by the Navy. Five launches, four for atmospheric measurements and one for a classified NOTS payload, were used to investigate the airplane as a first-stage booster. The F-104A Starfighter encountered several problems during testing. Approximately 40 practice flights were necessary to perfect pilot technique and ground-control coordination to achieve repeatability of initial conditions at launch. Airplane and maneuver incompatibility manifested in severe engine-compressor stalls, engine overtemperature, and flameout. Three different launch maneuvers were used for the five launches. To maintain unobstructed line of sight to the second-stage vehicle radar beacon and use the available impact area at Edwards Air Force Base, an over-the-shoulder maneuver was used for launches 1 and 2. Launches 4 and 5 made at the Pacific Missile Range were fired before vertical position was obtained. Launch 3 was initiated at a low attitude angle requiring a rollover and pull-through recovery after launch (Horton & Messing, 1963).

The USAF would eventually complete an air-launched anti-satellite missile or ASM-135 in 1982 (Kelly et al., 2017). Air Force Space Systems Command and LTV Aerospace made use of a McDonnell Douglas, now Boeing, F-15A. The F-15A would complete five flight tests, the third resulting in a successful demonstration against the US Solwind P78-1 satellite on September 13, 1985 (Garwin & Pike, 1984; Kelly et al., 2017; Lawson, 2017; Reynolds, 1985).

Intercept occurred at an altitude of 555 km, 6.7 km/sec, with a miss of the target point on the spacecraft by 6 inches. This launch using the over-the-shoulder maneuver (Horton & Messing, 1963) from a power climb inspired the space community with a vision of responsive space lift capability. F-15, F-104, Boeing 747-400, and Sukhoi SU-27 have all been considered as possible first stages for the airborne launch vehicle (Bartolotta et al., 2011; Carter, 2016; DePasquale et al., 2010; Foust, 2014; Hague et al., 2003; Kloesel & Clark, 2013; Kloesel et al., 2011). The rapid space lift capability provided has been desired since the NOTSNIK program in 1958 (Lawson, 2017).

DARPA has run several programs with the intent of speeding up access to space. The Airborne Launch Assist Space Access program was intended to launch 100 lbm satellites for less than $1 million total and launch from aircraft to enable more frequent missions (Foust, 2014). The DARPA Launch Challenge will receive notice of a launch site a few weeks prior, payload details a few days prior, launch and then launch again at a different site in two weeks into two different orbits each time ("DARPA Launch Challenge," 2019). DARPA also funded and

Figure 2-3. Virgin Orbit completing a drop test of LauncherOne on July 10, 2019. (Russell, 2019)

cooperated in studies with NASA Armstrong Flight Research Center for launch vehicles from a towed glider air-launch system (Carter, 2016; Spurrier, Walker, Merkley, & Whitmore, 2016; Whitmore, Merkley, Spurrier, & Walker, 2015). The NASA-DARPA trade space report on "Horizontal Launch: A Versatile Concept For Assured Space Access," concluded in 2011 focused on subsonic configurations using a 747-400F carrying the launch vehicle externally (Bartolotta et al., 2011) on top. Virgin Orbit is using a 747-400 carrying the launch vehicle externally under wing shown during a drop test in Fig. II-3. The Horizontal Launch Study identified potential near-and mid-term concepts capable of delivering 15,000 lbm payloads to a 28.5° due East inclination, 100 nautical-mile LEO. Payload capability of Virgin Orbit's LauncherOne and Northrop Grumman's Pegasus XL demonstrates the need for these large aircraft. Virgin Orbit's LauncherOne can deliver up to 500 kg to LEO and 300 kg to Sun-Synchronous Orbit (SSO) ("LauncherOne Service Guide," 2019). Northrop Grumman's Pegasus XL can deliver up to 475 kg to LEO and 125 kg to a Geostationary Transfer Orbit (GTO) ("Pegasus User's Guide," 2007).

Figure 2-4. The Pegasus XL being mated with the Orbital ATK L-1011 aircraft to launch CYGNSS (Herrera, 2016).

LauncherOne, Pegasus XL, NASA Armstrong's towed glider, and the NASA-DARPA trade space report are not geared towards rapid launch of a nanosatellite. They are targeting the microsatellite (10-100 kg) and minisatellite market (100-500 kg) and intend to launch multiple satellites from the same launch vehicle. Multiple payloads require a longer integration process. These systems are focused on providing launch access and independence to the small satellite market and could have the benefit of rapid launch capabilities if the process is streamlined.

2.3.2 Current status

Northrop Grumman's, formerly Orbital Sciences Corporation's (Orbital ATK), Pegasus has flown 44 times in 30 years and is the only successful airborne launch vehicle to-date (Foust, 2014). The Pegasus was developed with help from the Defense Advanced Research Projects Agency (DARPA) to meet the schedule flexibility goal and decrease payload to orbit costs

(Mosier & Rutkowski, 1993). Pegasus has only flown with NASA customers, requires over $55 million, and a modified L-1011 aircraft. The modified L-1011 requires specialized equipment and facilities to mate the Pegasus reducing the number of launch sites to only 5, Vandenburg, Cape Canaveral, Wallops Island, Kwajalein Atoll, and the Canary Islands (Clark, 2019). The Pegasus is shown being mated to the L-1011 aircraft in its Orbital ATK livery in Fig. II-4. Virgin Orbit's LauncherOne, an airborne launch vehicle dropped from a modified Boeing 747-400, "Cosmic Girl," is estimated to cost roughly $10-15 million and is solely targeting the small satellite market. Virgin Orbit in July 2019 announced their participation in a new United Kingdom Royal Air Force project ARTEMIS, intending to demonstrate capability of short call-ups on the order of a week for space lifts (Pomerantz & Russell, 2019). Currently, 9 months is the expected call-up time for Virgin Orbit ("LauncherOne Service Guide," 2019).

2.3.3 Launch profiles

Launch profiles or trajectories of airborne launch vehicles are important to the optimization of the rapid launch or rapid space lift problem. Initial conditions and aircraft, first-stages, define the required performance of the airborne launch vehicle.

Whitehead compared launch trajectories to provide broad results regarding significance of drag, ideal velocity to reach orbit, and the advantage of horizontal airborne launch vehicles. The common sense insights help illustrate decisions by Pegasus XL and LauncherOne on their trajectories. Smaller rockets require more ΔV to reach orbit if acceleration is constant as vehicles are scaled. Launches at 10 km, 32,810 ft, or 20 km, 65,620 ft, require less ΔV than those launched from the ground. Primarily because of drag, smaller vehicles see the most benefit (Whitehead, 2006).

The Pegasus XL is a three stage solid rocket 50 ft long, 50 in diameter, and a total mass 42,000 lbs, delivering a payload of 1100 lbs. LauncherOne is a two stage liquid rocket 70 ft long, 50 in diameter, and a total mass of 57,000 lbs, delivering a payload of 1000 lbs. The ASM-135 was a two stage solid rocket 18 ft long, 20 in diameter, and a total mass of 2,700 lbs, delivering a miniature homing vehicle about 30 lbs (Foust, 2014; Hague et al., 2003; Kelly et al., 2017; "LauncherOne Service Guide," 2019; "Pegasus User's Guide," 2007).

The ALSOR tests using the F-104A Starfighter are interesting especially in light of NanoLauncher's attempts to use a suborbital rocket launched from an F-104 (DePasquale et al., 2010). Maximum reported altitude achieved by ALSOR was 116 km, 383,000 ft with a payload fraction of 1.143×10^{-3} (Horton & Messing, 1963). ALSOR carried a payload in the nanosatellite range, 1-10 kg, our range of interest. ASM-135 is relatively close at 14 kg, 30 lbs, for the Miniature Homing Vehicle, especially when compared with Pegasus XL and LauncherOne. The ALSOR was 9 ft and ASM-135, double, at 18 ft.

Table 2-3. Current launch vehicles compared with an anti-satellite missile and sounding rocket.

Launch Vehicle Dimensions	Pegasus XL	LauncherOne	ASM-135	ALSOR	Units
m_0	92,610	125,685	5,954	440	kg
m_{pay}	500	475	14	1	kg
m_{pay}/m_0	0.005399	0.003779	0.002285	0.001143	
Diameter	1.28	1.27	0.51	0.17	m
Length	15.24	21.34	5.49	2.72	m
Area	1.29	1.27	0.20	0.02	m^2

Airborne launch vehicles from a tactical fighter aircraft should fit the form factor of current missiles to facilitate rapid deployment without modification to airframes. Four missiles considered, Sparrow, AMRAAM, HARM, and SLAM-ER, have two orders of magnitude higher payload mass ratios and two orders of magnitude lower drag-area-ratio profiles to the current airborne launch vehicles.

The F-104A and F-15A provided unique flight profiles to consider. The F-104A and F-15A

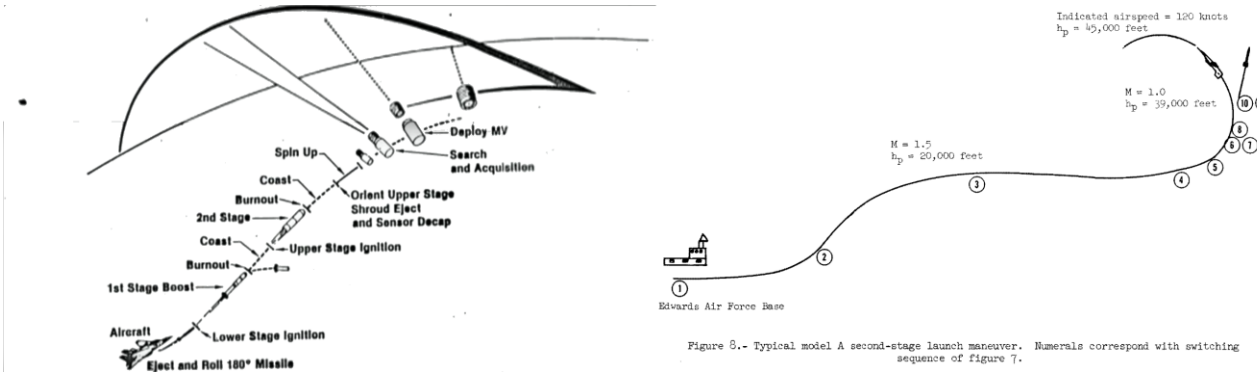

Figure 2-5. F-15A and F-104A both completed "over-the-shoulder" launches. (Day, 2010; Horton & Messing, 1963)

made use of the zoom climb ability by launching "over-the-shoulder" in a 1-3 g and 3.8 g launch. The L-1011, B-52, and Boeing 747-400 used for the Pegasus XL and LauncherOne pitch up slightly prior to drop but do not initiate a steep climb prior to launch to achieve a near-vertical angle. The launch vehicle in these cases drops until clear of the carrier aircraft and then initiates a 2.2 or ~3 g turn to achieve a vertical flight path angle.

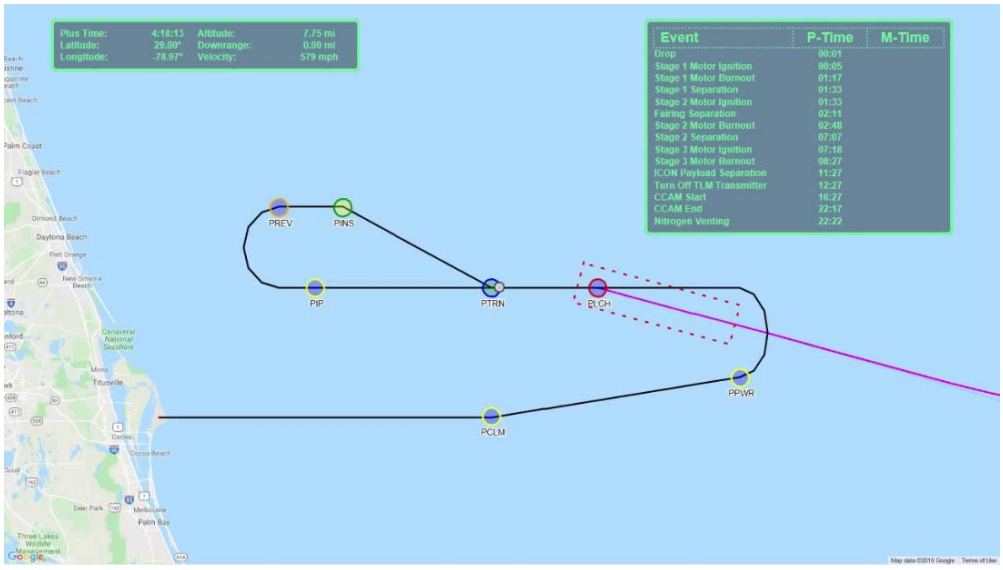

Figure 2-6. L-1011 Stargazer flight path for ICON launch from Cape Canaveral. (Clark, 2019)

2.4 Rapid Space Lift

Space assets provide near-worldwide coverage and access to otherwise denied areas. Advantages to using space include freedom of action, overflight, global perspective, and responsiveness. Responsivness from the rapid revisit times provided by LEO satellites and persistence by geosynchronous satellites. The US is increasingly dependent on the use of commercial systems to provide communications, tagging, tracking, and locating, and other support. Natural threats to space operations include orbital debris, solar activity, and radiation. Man-made threats include unintentional debris or EM interference. Intentional threats include but are not limited to jamming, lasing, cyberspace attacks, and ASAT weapons (STAFF, 2018).

2.4.1 Space Mission Assurance

Operationally responsive space is necessary to maintain US superiority in space. Increased capabilities by near-peer countries require the US to take safeguards to protect our space assets (Lt. Col. Whitney et al., 2019). The USSOCOM 19.3 Small Business Innovation Research (SBIR) Direct to Phase II Proposal in 2019 requested nanosatellite, 1-10 kg, payloads for tactical Intelligence, Surveillance, and Reconnaissance (ISR) (*19.3 Small Business Innovation Research (SBIR) Direct to Phase II Proposal Submission Instructions*, 2019). USSOCOM and the Department of Defense (DoD) have recognized the feasibility of using nanosatellite platforms for actual operation capabilities (Bille & Lishock, 1998). Schedule uncertainty from a variety of factors for large constellations means that replacing lost PNT capability from GPS or communications satellites could take years using traditional launch scheduling (Cates et al., 2018). Warfighting with near-peers in space for conventional purposes threatens the US nuclear mission especially the fragile Space Based Infrared Systems (SBIRs). Space represents the strategic high ground in enabling or preventing the flow of information to

allied and adversarial forces. Irregular space assets represent the new norm causing disruption and preventing normal deterrence measures (Cheng et al., 2018; Forbis, 2018; Krepon et al., 2013). Physical kinetic and nonphysical kinetic threats from near-peer adversaries have increased as space is used in combination with electronic and cyber warfare for greater effect (Lt. Col. Whitney et al., 2019).

Resilient space architecture or space mission assurance can be grouped into three categories: defensive operations, reconstitution, and resilience. Defensive operations include "synchronized and systematic maneuvers of on-orbit assets to confuse and overwhelm an enemy's targeting system," (STAFF, 2018). Reconstitution are the actions taken to restore systems to an acceptable level including launching additional satellites. Resilience includes disaggregation of dissimilar capabilities into separate platforms, distribution of nodes like GPS, diversification in orbits, protection against countermeasures like ASATs, proliferation of large numbers, and deception. "Given the physics of space operations, deception is likely a critical element of any space-system resilience effort," (STAFF, 2018). Rapid airborne launch of nanosatellite payloads from multiple sites addresses all of these concerns effectively. Nanosatellites encourage distribution and disaggregation as seen in the many Earth observing missions on-orbit. Leveraging an airborne launch, diversification of orbit is a benefit of access to a wide range of inclinations, delivering the satellite directly into its optimized orbit.

Rapid responsive launch can also address normal operation failures. The Launch and Early Operations Phase (LEOP) or check-out of Galileo 5 & 6, Europe's GNSS provider, saw both satellites suffer a launch injection failure from the Ariane V and solar array deployment failure (Come et al., 2016). Rapid responsive launch would be able to complement or provide

additional capability until these issues were resolved. In the case of servicing satellites it might even be able to provide assistance.

Anti-satellite weapons can be separated into four distinct types with varying degrees of attribution, awareness, damage assessment, and collateral damage capabilities. Kinetic physical weapons, including direct-ascent ASAT missiles, co-orbital ASAT satellites or kill vehicles, and ground station attack produce irreversible damage to the target and provide near real-time confirmation of success and attribution. Non-kinetic physical weapons can include high-altitude nuclear detonation due to the ElectroMagnetic Pulse (EMP), high-powered lasers, or high-powered microwaves. Electronic and Cyber ASAT attack are often the least attributable and therefore the least likely form of attack to experience retribution. Electronic attack includes uplink and downlink jamming or spoofing. Cyber attack includes data intercept or monitoring, data corruption, or seizure of satellite control.

The People's Republic of China's (PRC's) January 2007 kinetic kill anti-satellite SC-19 test against a Fengyun-1C weather satellite at an altitude of 863 km demonstrated China's ASAT capability. Comments by PLA officers and PRC civilian analysts justified the ASAT test as needed to counter perceived US hegemony in space and target the vulnerability of US dependence on satellites (Kan, 2007). Later direct-ascent tests would demonstrate ASAT capability against GEO targets in 2013. China has tested rendezvous and proximity operations (RPO) demonstrating co-orbital capabilities against space systems. SJ-17 continues to test RPO for close approaches and inspection against five Chinese GEO satellites and an Indonesian communications satellite. In 2006, China demonstrated its non-physical kinetic ASAT capabilities using a ground-based laser to dazzle American imaging satellites. Two islands in the

Spratly Island chain, confirmed as of April 2018, including Mischief Reef, support jamming systems for targeting communications and radar (Harrison et al., 2020).

3. METHODOLOGY

A mission planning system capable of optimizing delivery of multiple satellites from multiple similar air-launched platforms for constellation installation requires a reasonable accounting of performance. Making informed decisions regarding the space environment, especially at Low Earth Orbit (LEO), and the standard atmosphere we can reasonably model the injection and constellation performance for aircraft time-of-flight, launch vehicle ascent, orbit insertion, orbit, and orbital lifetime.

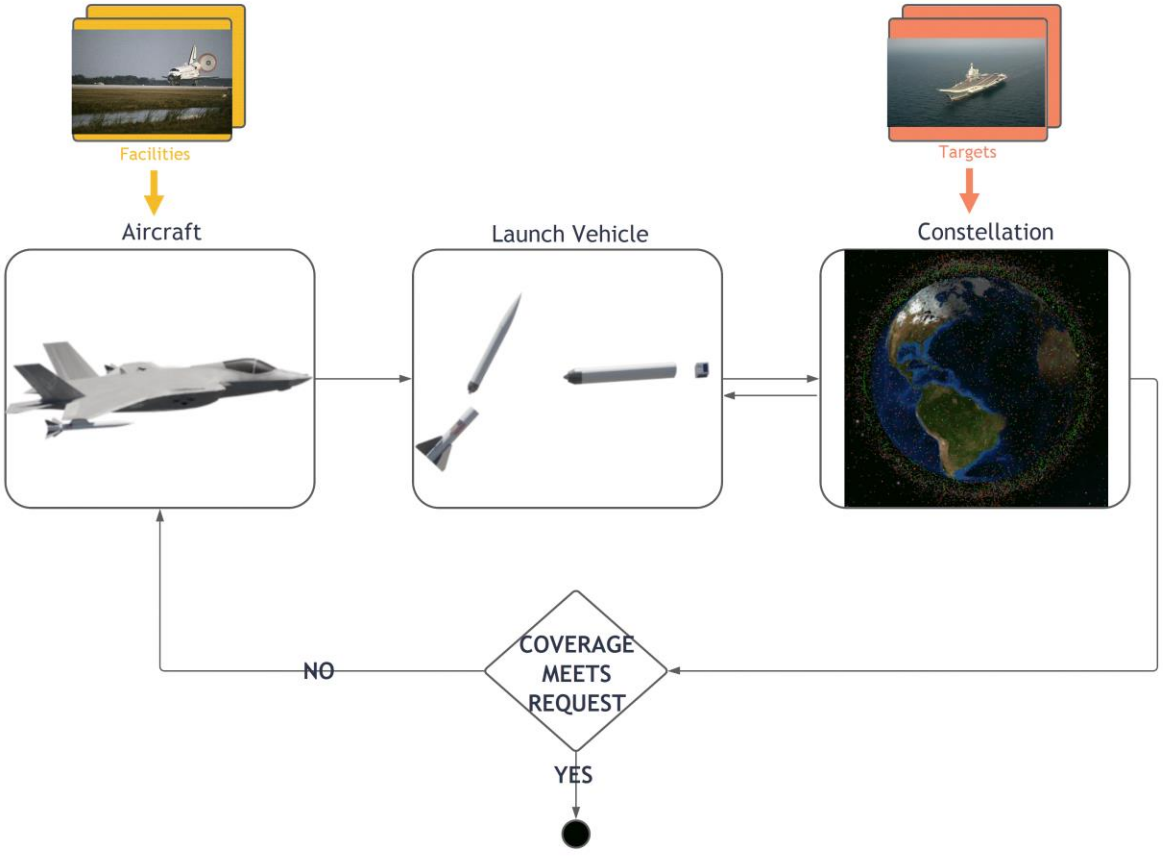

Figure 3-1. Optimization of on-demand launch schedule for coverage of selected targets.

The *injection performance* is considered within three software modules. Aircraft performance or the effective launch radius constraint, individual stage performance of the launch vehicle, and the orbital injection performance of the launch vehicle. The *constellation performance* is made of two software modules. Coverage quality determines the performance of the installed constellation. Performance duration tells us the impact of the atmosphere on constellation lifetime and degradation of performance.

3.1 Atmospheric Flight

Using the US Standard Atmosphere, 1976, (*U.S. Standard Atmosphere, 1976*, 1976), the aircraft and launch vehicle performance are predicted. Above 85 km, 275 kft, atmospheric density is neglected except for satellite lifetime assessments. The aircraft weight specific excess power will allow the prediction of minimum time-to-climb rate following takeoff.

3.1.1 US Standard Atmosphere

The standard atmosphere is a common reference and starting point. The air density affects the performance of aircraft and launch vehicle flight. Temperature, pressure, and density are defined for each geometric altitude. MIL-STD-210A, comparable with the US Standard Atmosphere and International Standard Atmosphere, ISO, (Defense, 1993), is used for non-standard atmosphere, hot, cold, tropic, or polar days. The US Standard Atmosphere is identical with the ICAO Standard, 1964, up to 32 km and the ISO Standard, 1973, up to 50 km, (*U.S. Standard Atmosphere, 1976*, 1976). The US Standard Atmosphere is derived from the following assumptions (Payne, 1990):

1. Sea level pressure is 29.9 inches mercury (Hg).
2. Measurement of vertical displacement is geopotential.

3. The air is dry.
4. The air composition is constant throughout the altitude range, 0 to 160,000 ft.
5. Sea level temperature is 288.16 Kelvin (K).
6. Temperature variation with geopotential is expressed as a series of straight line segments.

Geopotential altitude is a fictitious altitude physically compatible with the assumption that the acceleration due to gravity is constant equal to the given sea level value.

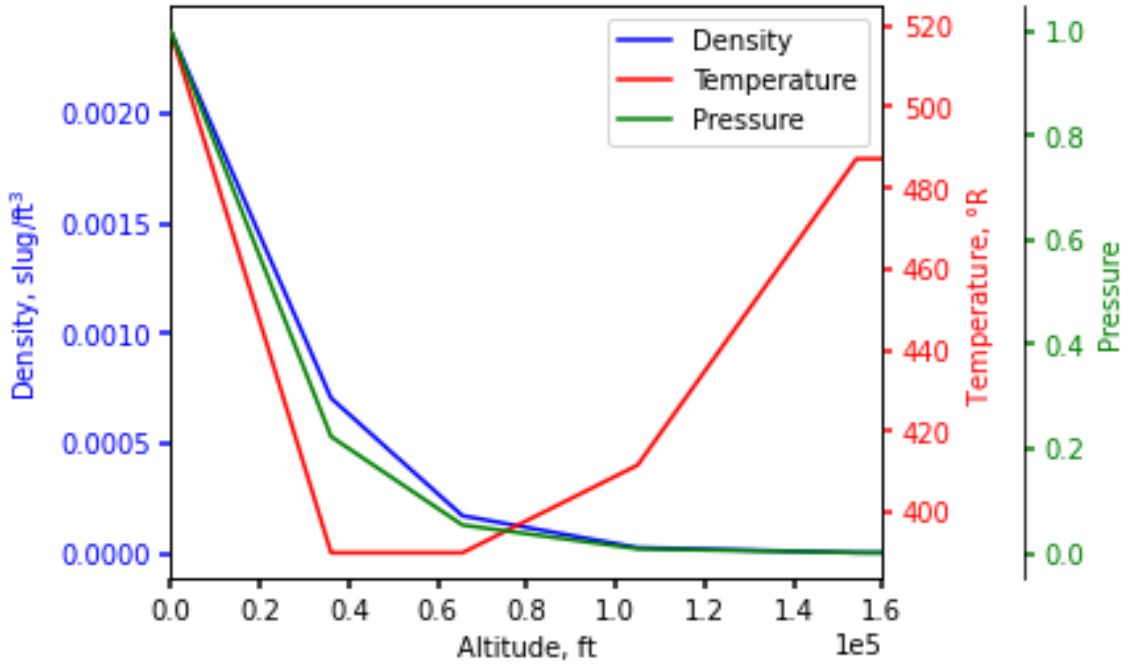

Figure 3-2. The U.S. Standard Atmosphere, 1976, density, pressure ratio, and temperature linear lapse rate from 0 to 160,000 ft at geopotential altitude.

3.1.2 Weight specific excess power, P_s

An optimal flight path for minimum time to climb is determined using specific excess power, P_s. Specific excess power, P_s, is a measure of performance derived from mechanical energy. The operational maneuverability and efficiency of an aircraft are directly related to the aircraft's energy state and energy rate capabilities. Specific excess power, P_s, is the rate at which the aircraft is capable of changing its energy height or specific energy:

$$E = KE + PE = \frac{1}{2}mV^2 + mgh \tag{3-1}$$

$$e_s = \frac{E}{W} = \frac{V^2}{2g} + h \tag{3-2}$$

$$P_s = \frac{de_s}{dt} = \frac{dV}{dt}\left(\frac{V}{g}\right) + \frac{dh}{dt} = \frac{P_{av} - P_{req}}{W} = \frac{V(T - D)}{W}. \tag{3-3}$$

For the P_s model where T information is not fully available we assume a linearly decreasing rate of climb as altitude increases so that $dh = f(h)\, dt$, where $f(h)$ is approximated by $ah + b$. Solving for dt,

$$dt = \frac{dh}{ah + b} \tag{3-4}$$

$$t_{climb} = \frac{1}{a}(\ln(ah_2 + b) - \ln(ah_1 + b)), \tag{3-5}$$

where b is the sea level rate of climb and a is the slope of the linearly decreasing rate of climb. The time to climb is given by Eq. (3-5) when the altitude at takeoff, $h_1 = 50$ ft, and altitude at release, $h_2 = 38{,}000$ ft, is assumed.

3.1.3 Take-off performance

An airplane must accelerate from zero ground speed to a minimum speed to takeoff safely. The takeoff speed gives the aircraft a safety margin. Common practice, (Payne, 1990), is to use 1.2 times the 1-g takeoff configuration stall speed as the desired takeoff speed, placing the aircraft safely above stall and near minimum drag for most aircraft. Total take-off distance includes the ground run distance, S_g, plus the airborne distance required to clear a 50 ft obstacle, S_a.

During take-off thrust is estimated as $T = T_0 - aV^2$, where T_0 is the static thrust and a is some constant. The time and distance of the ground run to achieve the take-off velocity, V_{to}, is calculated by estimating the static thrust T_0 as the maximum thrust without after-burner and the constant a as zero. The ground roll distance, S_g is given by Eq. (3-6). The time to achieve V_{to} is given by Eq. 3-7. A headwind, V_w, and runway down slope, γ_R, will reduce the ground roll:

$$S_g = \frac{W}{2g\left[\frac{\rho S}{2}(C_D - \mu_R C_L) + a\right]} \ln\left[\frac{\frac{T_0}{W} - (\mu_R \cos\gamma_R + \sin\gamma_R)}{\left(\frac{T_0}{W} - (\mu_R \cos\gamma_R + \sin\gamma_R)\right) - \left(\frac{1}{W}\right)\left[\frac{\rho S}{2}(C_D - \mu_R C_L) + a\right] V_{to}^2}\right] \tag{3-6}$$

$$t_g = \frac{\tanh^{-1}\left(V_{to}\sqrt{\frac{\frac{g}{W}\left[\frac{\rho S}{2}(C_D - \mu_R C_L) + a\right]}{g\left(\frac{T_0}{W} - (\mu_R \cos\gamma_R + \sin\gamma_R)\right)}}\right)}{\sqrt{g\left(\frac{T_0}{W} - (\mu_R \cos\gamma_R + \sin\gamma_R)\right)\left(\frac{g}{W}\left[\frac{\rho S}{2}(C_D - \mu_R C_L) + a\right]\right)}}. \tag{3-7}$$

To minimize time and ground run length, the pilot will rotate the plane to achieve lift-off, changing the angle-of-attack by deflecting control surfaces, instead of continuing to accelerate until lift-off occurs naturally due to C_L. Some aircraft like the B-52 require long runways and long, shallow landing approaches because rotation is virtually impossible to complete safely. In both Eqs. 3-6 and 3-7 note the thrust, T, component. Eqs. 3-6 and 3-7 are determined from deriving the equations of motion in the body frame of reference for the aircraft assuming thrust is perfectly aligned with the x-axis. To achieve short take-off the F-35B Lightning II Short Take-Off and Vertical Landing (STOVL) aircraft deflects the F-135-PW-600 aft exhaust nozzle. This

enables the F-35B to perform the STO from the HMS Queen Elizabeth ski-jump ramp with a combat load-out (Fry, Cook, & Revill, 2009).

Ground run distance, S_g, and ground run time, t_g, are simplified by introducing variables A and B, given by Eqs. 3-8 and 3-9, which are functions of drag, ground roll friction, ground slope, and static engine thrust:

$$A = g\left[\frac{T_0}{W} - (\mu_R \cos\gamma_R + \sin\gamma_R)\right] \tag{3-8}$$

$$B = \frac{g}{W}\left[\frac{\rho S}{2}(C_D - \mu_R C_L) + a\right] \tag{3-9}$$

$$S_g = \frac{1}{2B}\ln\left[\frac{A}{A - BV_{to}^2}\right] \tag{3-10}$$

$$t_g = \frac{\tanh^{-1}\left(V_{to}\sqrt{\frac{B}{A}}\right)}{\sqrt{AB}}. \tag{3-11}$$

The simplified equations, Eqs. 3-10 and 3-11, can include thrust deflection, δ, if A and B are rewritten as Eqs. 3-12 and 3-13:

$$A = g\left[\frac{T_0}{W}(\cos\delta + \mu_R \sin\delta) - (\mu_R \cos\gamma_R + \sin\gamma_R)\right] \tag{3-12}$$

$$B = \frac{g}{W}\left[\frac{\rho S}{2}(C_D - \mu_R C_L) + a(\cos\delta + \mu_R \sin\delta)\right]. \tag{3-13}$$

Figure 3-3. An F-35C Lightning II completes its ground run off the flight deck of the USS Abraham Lincoln (Escobosa, 2017).

Fig. 3-3 shows the beginning of the airborne phase for takeoff. The airborne distance is estimated by considering the mechanical change of energy during the short airborne phase. The change in energy is related to the work done or force applied over distance, $\int_{S_g}^{S_a} T - (D + W)\, dS$. The distance necessary to climb-out and finish the takeoff is the airborne distance, S_a. The airborne distance, S_a, is given by Eq. 3-16. The change in kinetic and potential energy is given by the numerator in Eq. 3-16. V_3 is the climb-out speed with all engines operating. Any scenario off-nominal including an engine failure on takeoff will not be considered for this dissertation:

$$\int F\, dS = \int_0^{S_a} T_0 - \left(\frac{1}{2}\rho C_D S + a\right) V^2 - W\, dS = S_a \left[T_0 - \left(\frac{1}{2}\rho C_D S + a\right) V_3^2 - W\right] \quad (3\text{-}14)$$

$$\Delta[KE + PE] = W\left[\frac{V_3^2 - V_{to}^2}{2g} + 50\right] \quad (3\text{-}15)$$

$$S_a = \frac{W\left[\frac{V_3^2 - V_{to}^2}{2g} + 50\right]}{T_0 - \left[\left(\frac{1}{2}\rho C_D S + a\right)V_3^2 + W\right]}. \tag{3-16}$$

Euler method estimates the time to traverse the airborne distance while ignoring the acceleration over the short distance. The time to climb-out, t_a, or complete the takeoff is given by Eq. 3-17. Adding the time for the ground roll, t_g, with the time to climb-out, t_a, provides the total take-off time estimate, t_f, for aircraft launching from different facilities around the world:

$$t_a = \frac{(V_3 - V_{to})}{S_a - S_g} \tag{3-17}$$

$$t_f = \frac{\tanh^{-1}\left(V_{to}\sqrt{\frac{B}{A}}\right)}{\sqrt{AB}} + \frac{V_3 - V_{to}}{S_a - S_g}. \tag{3-18}$$

3.2 Launch Vehicle Platform

Primary attention is given to the development of a simplified module that supports scheduling decisions. An optimal trajectory for minimum-time orbital injection of the two-stage launch vehicle from the airborne platform is modeled as Lambert's problem. The vehicle dimensions will reflect that of an AMRAAM (12 ft long, 7 in diameter) for easy integration with a tactical fighter aircraft. The design of launch vehicles, their related sub-systems, and control have generated many successful dissertations, theses, and inspired engineers to dream of escaping the bounds of this pale blue dot, the author among them. Detailed is a suitable model for the purposes of this dissertation, limited in scope.

3.2.1 Lambert's Problem

Lambert's problem is determination of an orbit having a specified transfer time and connecting two position vectors. Lambert's problem solutions are essential for spacecraft and

missile targeting. Lambert's theorem, Eq. 3-19, posits that transfer time is dependent only on the semi-major axis, a, the sum of the distances of the initial and final points of the arc from the force center, $r_1 + r_2$, and the chord length joining the two points, c. Transfer time, counter-intuitively, does not depend on the eccentricity of the arc (Battin, 1999):

$$\sqrt{\mu}(t_2 - t_1) = F(a, r_1 + r_2, c). \tag{3-19}$$

The theorem is true for a general conic. Solution of the transfer-time relation depends on a single orbital element iterated to solve the boundary-value problem. Solving Lambert's problem provides the velocity at each point to determine the energy cost of the transfer.

The energy cost is described in terms of the change in velocity or "delta-v," ΔV. The energy cost, ΔV, is directly proportional to the transfer time for the launch vehicle. After the appropriate orbits are selected for the constellation, the launch vehicle will inject the satellite into the orbit that optimizes the transfer time and therefore reaction time. The launch vehicle will be constrained by the performance of its motors. Launching requires $\Delta V_1 = \int_{t_0}^{t_1} T/m \, dt$, where thrust, T, and mass, m, are functions of time. Different motors' performance can be compared in Eq. 3-20 using the specific impulse, I_{sp}, or characteristic exhaust velocity, c and the initial and final mass, m_i and m_f, respectively. Eq. 3-21 checks the launch vehicle provides the minimum performance necessary for the maneuver or burn, ΔV, given the inert mass fraction, f_{inert}, of the launch vehicle:

$$\Delta \mathrm{V}_1 = I_{sp_1} g_0 \ln \frac{m_i}{m_f} = c \ln \frac{m_i}{m_f} \tag{3-20}$$

$$I_{sp_1} \leq \frac{\Delta V_1}{\ln\left(\frac{1}{f_{inert}}\right) g_0}. \tag{3-21}$$

3.2.2 Equations of motion

Operations for current airborne launch vehicles, Pegasus and LauncherOne, involve a flight path through a corridor where the aircraft maintains a certain speed, altitude, and heading before being dropped. The airborne launch vehicle then ignites after a specified time, 5 seconds for both current vehicles, following drop. The ALSOR program launched by the F-104A (Horton & Messing, 1963) ignited on the rail or rail-launched. The Pegasus launch vehicle will change its angle of attack until some limiting acceleration is met. The flight path angle of that trajectory is then maintained until a gravity turn is initiated as the vehicle arcs over into orbit.

Sizing plays an important role when atmospheric losses are considered. The cross-sectional area in the direction of motion is proportional to the drag force exerted on the launch vehicle. The ballistic coefficient, $C_D A/m$, is determined by launch vehicle shape and mass. Using a two-dimensional body-fixed reference frame, the equations of motion for a launch vehicle are described in Eqs. 3-22 and 3-23:

$$\sum F_y = L\cos\alpha + D\sin\alpha - (W\cos(\alpha+\gamma) + T\sin\delta) \tag{3-22}$$

$$\sum F_x = L\sin\alpha + T\cos\delta - (W\sin(\alpha+\gamma) + D\cos\alpha). \tag{3-23}$$

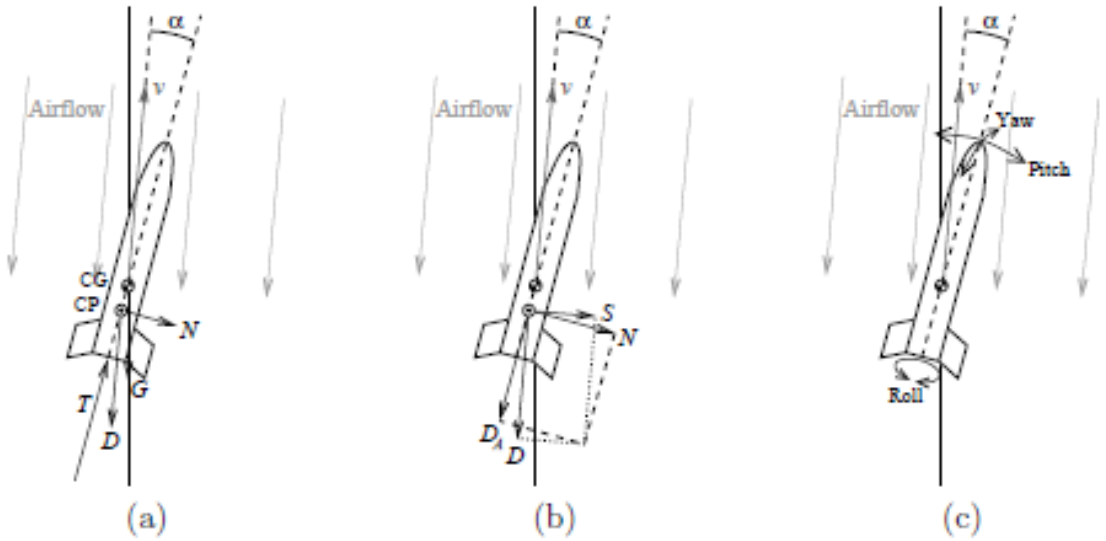

Figure 3-4. (a) The forces acting on a rocket in free flight: weight, G, thrust, T, drag, D, and normal force, N. (b) Deriving the perpendicular components to align drag with the x axis. The perpendicular component pairs of the resultant aerodynamic force are: N and axial drag, D_a; side force, S, and D. (c) Pitch, yaw, and roll or attitude angles about $y, z,$ and x axes. (Christopher R. Simpson & O'Neill, 2016)

Expanding to the three-dimensional body-fixed reference frame while maintaining the assumption of the launch vehicle as a point mass, we consider a state given by the instantaneous radius, r, absolute longitude, λ, latitude, ϕ, flight path angle, γ, velocity, v, and azimuth angle, ψ. Control is provided through thrust deflection in angle-of-attack and sideslip angles. Including aerodynamic forces, Eqs. 3-24;

$$
\begin{aligned}
\dot{r} &= v\sin\gamma \\
\dot{\lambda} &= \frac{v\cos\gamma\sin\psi}{r\cos\phi} \\
\dot{\phi} &= \frac{v\cos\gamma\cos\psi}{r} \\
\dot{\gamma} &= \frac{v\cos\gamma}{r} + \frac{T\sin\alpha + L}{mv}\cos\beta\ - \frac{\mu_\oplus\cos\gamma}{v} + 2\omega_\oplus\sin\psi\cos\phi \\
&\quad + \frac{\omega_\oplus^2 r}{v}\cos\phi\,(\cos\psi\sin\gamma\sin\phi + \cos\gamma\cos\phi) \\
\dot{v} &= \frac{T}{m}\cos\alpha - \left(\mu_\oplus\sin\gamma + \frac{D}{m}\right) + \omega_\oplus^2 r\cos\phi\,(\sin\gamma\cos\phi - \sin\phi\cos\gamma\cos\psi) \\
\dot{\psi} &= \frac{T\sin\alpha + L}{mv\cos\gamma}\cos\beta + \frac{v}{r}\tan\phi\sin\psi\cos\gamma + 2\omega_\oplus(\sin\phi - \cos\psi\cos\phi\tan\gamma) \\
&\quad + \frac{r}{v\cos\gamma}\omega_\oplus^2\sin\psi\cos\phi\sin\phi\,.
\end{aligned}
\tag{3-24}
$$

Inherent in this derivation is that the angle of attack, α, and side-slip angle, β, if thrust deflection is used, are calculated in from this deflection. If lifting surfaces are present, such as in the Pegasus vehicle, then control surface deflection will be directly related to α and β.

3.2.2 Ideal performance

Ideal launch cost is a potential energy cost only considers the cost of moving to a higher orbit for a two-body gravitational problem. Atmospheric contributions are not considered. ΔV_1, the cost to leave the altitude or lower orbit and reach the desired altitude or higher orbit is given for the airborne case in Eq. 3-25. β is the launch azimuth or the direction from due east, positive counterclockwise, γ, flight-path angle, the angle from horizontal for the launch, and η the ratio of aircraft radius from the focus over the target radius, $\frac{h_{a/c}+r_\oplus}{r}$:

$$
\begin{aligned}
&\Delta V_1 \\
&= \sqrt{2\frac{\mu}{r_\oplus + h_{a/c}}\left(\frac{1-\eta}{1-(\eta\cos\gamma)^2}\right) + v_{a/c}^2 - 2v_{a/c}\cos\beta\sqrt{2\frac{\mu}{r_\oplus + h_{a/c}}\left(\frac{1-\eta}{1-(\eta\cos\gamma)^2}\right)}}\,.
\end{aligned}
\tag{3-25}
$$

The cost to circularize the orbit is expressed as ΔV_2 in Eq. 3-26:

$$\Delta V_2 = \sqrt{\frac{\mu}{r_\oplus + h_{a/c}}}\left[\sqrt{\eta} - \eta\cos\gamma\sqrt{2\left(\frac{1-\eta}{1-(\eta\cos\gamma)^2}\right)}\right]. \quad (3\text{-}26)$$

The launch azimuth, β, determines the inclination, i, of the orbit. A launch azimuth of $\beta = 0°$ would make $i = \phi$, where ϕ is the launch latitude. Determining the correction to β for spherical geometry, α, we can determine i as $\cos i = \cos\alpha\cos\phi$:

$$\tan\alpha = \frac{\tan\beta}{1 + \left(\frac{v_{a/c}}{\Delta V_1\cos\beta}\right)}. \quad (3\text{-}27)$$

The ideal ΔV just calculated does not include atmospheric nor gravity losses, approximately 1,500 m/s for a typical vertical launch vehicle (Altman et al., 1995; Sarigul-Klijn, Sarigul-Klijn, & Noel, 2005). Expected drag losses for an airborne launch vehicle that undergoes a high-g turn to achieve the required flight-path angle after being dropped from the aircraft could exceed 1,500 m/s. The ideal ΔV provides an estimate of necessary rocket motor performance.

3.2.3 Hybrid Engine

Hybrids bridge the gap between liquid and solid engines. Liquid engines, requiring pump systems and mixing design for both fuel and oxidizer, rarely use storable propellants. HTPB, hydroxyl-terminated poly-butadiene or aluminum in a polymer binder fuels, are primarly used in solid motors, see Space Shuttle re-usable boosters. While lesser performers than liquid engines, they require less hardware development, more cost-effective, and can be stored for long periods of time. Solids are exceptionally hard to stop firing and require pre-formed throttling by molding the grain assuming timing is accurate. Hybrids experience significant advantages over solids;

- can be fabricated at any site without risk of explosion
- reduced sensitivity to cracks and debonds in the grain
- better specific impulse than solids,
- throttling to optimize trajectory for atmospheric launch and orbit injection

- terminate thrust on demand

A “normal” hybrid injects the oxidizer into the solid fuel port, combustion chamber. A “reverse” hybrid is one using a liquid fuel and solid oxidizer. This simplified model focuses on normal hybrid engines. Hybrid engines rely on a combustion mechanism of fuel melting, evaporation and diffusive mixing. Large polymeric fuels evaporate too slowly making it difficult to produce high thrust (Cantwell, 2020). Thrust performance is determined by regression rate of the fuel which is coupled to mass flux:

$$\frac{\partial r(x,t)}{\partial t} = \frac{a}{x^m}\left(\frac{\dot{m}_{port}}{\pi r^2}\right)^n \tag{3-28}$$

$$\frac{\partial \dot{m}_{port}(x,t)}{\partial x} = \rho_f(2\pi r)\frac{a}{x^m}\left(\frac{\dot{m}_{port}}{\pi r^2}\right)^n. \tag{3-29}$$

Eq. 3-29 assumes a circular port such that $2\pi r$ is the circumference or instantaneous burning area. Integrating Eq. 3-29 over the burn time provides the amount of propellant mass, m_{prop}, required, at 100% efficiency. From the propellant mass required we can determine the characteristic velocity, c^*, or thrust over mass flow, $T/\dot{m}$ performance required to meet the total impulse:

$$m_{prop}\frac{dv}{dt} = \rho_e v_e^2 A_c + (P_e - P_a)A_e \tag{3-30}$$

$$c^* = \frac{T}{\dot{m}} = v_e + \frac{A_e}{\dot{m}}(P_e - P_a). \tag{3-31}$$

The paraffin hybrid with N_2O, GOX, and LOX oxidizers overcomes the limitations of HTPB hybrids by reducing the web complexity. The paraffin hybrid outperforms HTPB hybrids and HTPB regression rate mechanisms. The paraffin hybrid performance documented by Cantwell and Karabeyoglu has been relied on for motor development (Cantwell, 2020; Karabeyoglu, 2008;

Karabeyoglu, Zilliac, Cantwell, DeZilwa, & Castellucci, 2003, 2004; Sella et al., 2020; Simurda et al., 2012). Given the estimated energy required by ΔV, motor performance is determined by I_{sp} or effective exhaust velocity, c, in Eq. 3-20:

$$\Delta \mathrm{V}_1 = I_{sp_1} g_0 \ln \frac{m_i}{m_f} = c \ln \frac{m_i}{m_f} \quad \textbf{(3-20)}$$

$$I_{sp_1} \leq \frac{\Delta V_1}{\ln\left(\frac{1}{f_{inert}}\right) g_0}. \quad (3\text{-}21)$$

Eq. 3-21 provides the check on performance for each stage given the inert mass fraction which is assumed based on historical data. Given the AMRAAM AIM-120 format and a nominal 10 kg payload we can determine the inert mass fraction and performance of motors given a fixed O/F ratio.

Table 3-1. Sizing for the two hybrid motors in AIM-120 form factor.

Stage	Motor	Length (m)	Case Dia (m)	D_t (m)	D_e (m)
Stage 1	HTPB/N2O	1.8288	0.18	0.0889	0.18
Stage 2	HTPB/N2O	1.1088	0.18	0.0889	0.18
Stage 1	SP-1a/N2O	1.8288	0.18	0.0889	0.18
Stage 2	SP-1a/N2O	1.1088	0.18	0.0889	0.18
Stage 1	HTPB/LOX	1.8288	0.18	0.0889	0.18
Stage 2	HTPB/LOX	1.1088	0.18	0.0889	0.18
Stage 1	SP-1a/LOX	1.8288	0.18	0.0889	0.18
Stage 2	SP-1a/LOX	1.1088	0.18	0.0889	0.18

Table 3-2. Mass sizing given historical hybrid motor data (Altman et al., 1995).

Stage	Motor	Prop (kg)	Ins (kg)	Case (kg)	Nozzle (kg)	Igniter (kg)	Misc. (kg)	Total (kg)
Stage 1	HTPB/N2O	38.537	0.8405	1.7364	0.746	0.0288	0.0666	41.956
Stage 2	HTPB/N2O	22.847	0.5712	1.0079	0.8968	0.04	0.0748	25.438
Stage 1	SP-1a/N2O	18.365	0.4005	0.8275	0.3555	0.0137	0.0317	19.994
Stage 2	SP-1a/N2O	10.888	0.2722	0.4803	0.4274	0.0191	0.0356	12.123
Stage 1	HTPB/LOX	38.162	0.8323	1.7195	0.7388	0.0286	0.0659	41.547
Stage 2	HTPB/LOX	22.625	0.5656	0.9981	0.8881	0.0397	0.0741	25.19
Stage 1	SP-1a/LOX	38.371	0.8368	1.7289	0.7428	0.0287	0.0663	41.774
Stage 2	SP-1a/LOX	22.748	0.5687	1.0035	0.8929	0.0399	0.0745	25.328

Table 3-3. Mass fraction of each launch vehicle.

Stage	Motor	f_{prop}	f_{inert}	f_{pay}
Stage 1	HTPB/N2O	0.91853	0.08147	0.23835
Stage 2	HTPB/N2O	0.89816	0.10184	0.39312
Stage 1	SP-1a/N2O	0.91853	0.08147	0.50014
Stage 2	SP-1a/N2O	0.89816	0.10184	0.82491
Stage 1	HTPB/LOX	0.91853	0.08147	0.24069
Stage 2	HTPB/LOX	0.89816	0.10184	0.39698
Stage 1	SP-1a/LOX	0.91853	0.08147	0.23938
Stage 2	SP-1a/LOX	0.89816	0.10184	0.39483

3.3 Orbital Mechanics

To design the constellation to be launched; orbital dynamics must be accounted for, satellite views of the central body about which they orbit should be defined, figures of merit for satellite viewing times must be created, and the lifetime of the satellites in orbit should be calculated. Graceful degradation of the constellation is not a priority and therefore not considered here.

A short review of classical orbital mechanics, applied orbital perturbations, and spacecraft collision probability is provided. The terminology and nomenclature used here are used consistently. Those seeking a deeper understanding of orbital mechanics should review Chobotov, Battin, or Bate, Mueller, and White (Bate et al., 1971; Battin, 1999; Chobotov et al., 2002) before continuing. See Eq. 3-32 for the two-body point mass problem or the gradient of the gravitational potential:

$$\ddot{r} = -\frac{GM_{\oplus}m}{r^2}\hat{r} = -\frac{\mu_{\oplus}}{r^2}m\hat{r} = \nabla U. \tag{3-32}$$

Classical orbital elements, listed here and shown in Figure 3-7, are (1) a, semimajor axis, (2) e, eccentricity, (3) i, inclination, or the angle between $\bar{h}$ and $\hat{K}_{eci}$, (4) Ω, longitude of the ascending node, or the angle in the fundamental plane between $\hat{I}_{eci}$ and the ascending node

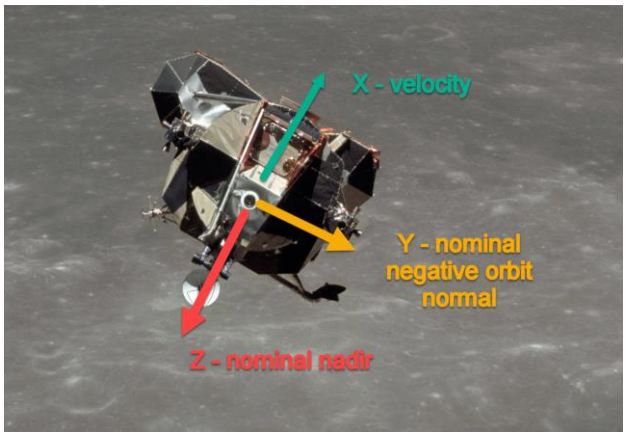

Figure 3-5. The spacecraft reference frame is laid over the Apollo 11 Lunar Module (LM). (Collins, 1969)

measured counterclockwise when viewed from the north side (top-down) of the fundamental plane, (5) ω, argument of periapsis, the angle in the satellite orbital plane between the ascending node and the periapsis point, and (6) ν, true anomaly, or the angle in the satellite orbital plane from the periapsis point to the satellite's current position at a particular time, t.

A reference frame is an ordered set of three mutually orthogonal unit vectors and an origin. If the orthogonal vectors are time dependent then the frame is non-inertial. The coordinate system for that particular frame specifies the method of point location within the frame.

The satellite shown in Figure 3-5 is shown in the spacecraft-fixed frame. The origin is the spacecraft's center. The Apollo 11 Lunar Module (LM) ascent stage is rotated from nominal in this view. The spacecraft-fixed frame is originally fixed in the nadir (Moon pointing) for the +Z direction, and in the velocity direction of the orbit for the +X direction. +Y is found through cross product formation and indicates the fundamental plane (orbit plane) of the reference frame.

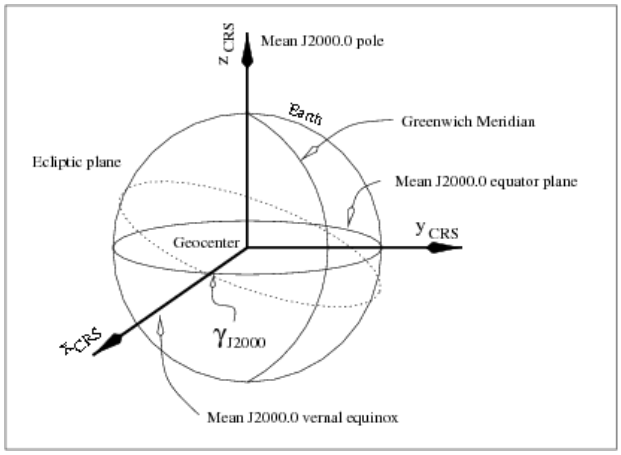

Figure 3-6. The ECI, J2000, frame is effectively the Celestial Reference Frame.

The Earth-Centered Inertial (ECI) or J2000.0 frame in Figure 3-6 is an inertial frame for our case. The +X direction is the

intersection of equatorial and ecliptic planes in the direction of the vernal equinox. The +Z direction is normal to the mean equator of date at epoch J2000 Barycentric Dynamical Time (TDB), approximately Earth's spin axis orientation at that epoch. The epoch J2000 is 01 Jan 2000 12:00:00 TDB or JD 2451545.0 TDB. The fundamental plane is the equatorial plane (Acton, Bachman, Thomson, Semenov, & Wright, 2020).

The International Celestial Reference Frame (ICRF) was made to coincide almost exactly with the J2000 frame. The ICRF origin is located at the barycenter of the solar system through modeling of the Very Long Baseline radio Interferometry (VLBI) observations in the General Relativity framework. VLBI measures the time differences in the arrival of microwave signals from extragalactic radio sources received at two or more radio observatories. More than 600 radio sources at 120 different observatories are used. VLBI is the only technique capable of measuring all components of the Earth's orientation accurately and simultaneously. The difference between ICRF and ECI is a rotation of less than 0.1 arc second. No transformation is required to convert between the two (Acton et al., 2020; "The International Celestial Reference System (ICRS)," 2013).

The state vector of the spacecraft is defined as a combination of position from center of the Earth to the spacecraft, $\bar{r}$, and velocity, $\bar{v}$, with respect to the ECI Cartesian coordinate frame in Eq. 3-33. The two-body equations of motion for the state vector are given by Eq. 3-34 and expanded to the gravitational potential in Eq. 3-35 for addition of gravitational perturbations due to an oblate spheroid. Drag or other non-conservative perturbations can be added to the individual terms for the force applied in that particular direction:

$$\bar{X} = [r_I \quad r_J \quad r_K \quad v_I \quad v_J \quad v_K]^T \tag{3-33}$$

$$\dot{\bar{X}} = \left[v_I \quad v_J \quad v_K \quad -\mu_\oplus r_I/r^3 \quad -\mu_\oplus r_J/r^3 \quad -\mu_\oplus r_K/r^3\right]^T \tag{3-34}$$

$$\dot{\bar{X}} = [v_I \quad v_J \quad v_K \quad \partial U\hat{r}_I/\partial r_I \quad \partial U\hat{r}_J/\partial r_J \quad \partial U\hat{r}_K/\partial r_K]^T. \tag{3-35}$$

3.3.1 Applied Orbit Perturbations

Two-body, Keplerian, mechanics does not take into account perturbing accelerations acting upon the spacecraft. Two-body mechanics simplifies the satellite and the focus of the orbit as two point masses. The Earth is lumpy, other bodies, solar radiation pressure, drag, solid and ocean tides, relativistic effects, infrared Earth radiation, optical Earth albedo, Earth Yarkovsky, and solar Yarkovsky all affect spacecraft orbits. Using these perturbing accelerations Lara and Russell and Fasano and D'Errico both used geopotentials expressed in harmonics to build repeating ground track orbits (Fasano & D'Errico, 2006; Lara & Russell, 2008). As the zonal harmonic, J_2, is the largest perturbing force affecting satellite orbits. Drag force on the satellite is the next largest perturbing force proportional to altitude (Dell'Elce et al., 2015). A first-order ground track design is achieved including J_2 to approximate the nominal solution. Further refinement, includes additional perturbations and a medium degree zonal model to provide the nominal orbit.

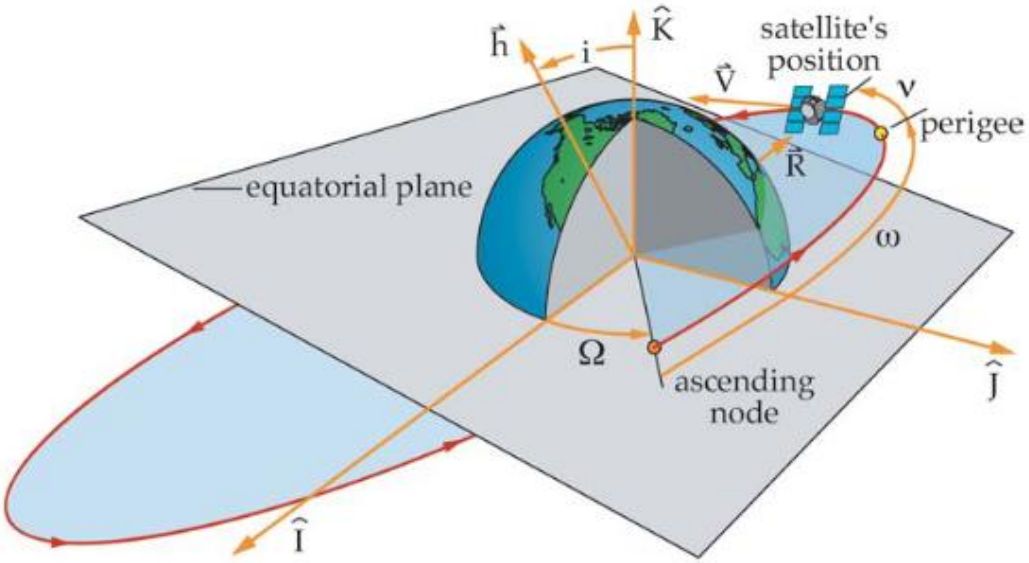

Figure 3-7. Classical orbital elements, except for semimajor axis and eccentricity vector shown in ECI frame(*Describing Orbits*, 2017).

Perturbing forces are divided into conservative and non-conservative perturbations. Conservative perturbations acting on satellites are a function of position. The satellite does not lose nor gain mechanical energy, only transfers it between kinetic and potential. Non-conservative perturbations include drag, outgassing, and tidal forces. Conservative perturbations include N-body attractions, non-spherical celestial bodies, i.e. an oblate Earth, and solar radiation pressure. Surface spherical harmonic function to describe Earth's lumpiness is given by Eq. 3-36. The most common gravitational model used, represented by spherical harmonics, is the WGS84. WGS84 has its own reference frame within centimeters of the International Terrestial Reference Frame (Battin, 1999; Chobotov et al., 2002; Tapley, Schutz, & Born, 2004):

$$U = \frac{\mu}{r}\Sigma_{n=0}^{\infty}\Sigma_{m=0}^{n}\left(\frac{r_{\oplus eq}}{r}\right)^{n} P_n^m(w)\left(C_{n,m}\cos m\lambda + S_{n,m}\sin m\lambda\right). \quad (3\text{-}36)$$

Tidal effects are when one side of the celestial body experiences greater acceleration. Tidal effects redistribute liquid and solid mass of the body. It can change ground station

positions and affect spacecraft acceleration. Tidal potential can be approximated by Eq. 3-37 where Love numbers, k_n, describe how deformable the affected body is (Pisacane, 2008):

$$U_t = -\frac{\mu_n}{r}\Sigma_{n=2}^{\infty} k_n \left(\frac{r}{R}\right)^n P_n(\cos\psi). \tag{3-37}$$

Drag on a spacecraft is proportional to the ballistic coefficient, atmospheric density, and velocity squared. Drag acts against the direction of motion. The ballistic coefficient, $B = \left(\frac{C_D A}{m}\right)$, is determined by spacecraft shape, cross-sectional area exposed in the translational direction, and mass of the vehicle. Air density is estimated by the model atmosphere at the given altitude:

$$a_D = -\frac{1}{2}\rho V^2 B. \tag{3-38}$$

Drag experienced by spacecraft is within the free molecular flow region, where the Knudsen number, K_N is greater than 10. The approximate K_N is given by M_∞/R_N, where R_N is the Reynold's number for the flow regime. The K_N is greater than 10 for a characteristic length of 1 ft at 121 km (Townsend et al., 1963). Therefore, for near-circular orbits we can approximate the energy loss due to drag proportional to the ballistic coefficient, B, as shown in Eq. 3-39:

$$\Delta E_D = \oint \frac{D}{m} ds \approx 2\pi\mu_\oplus B \rho_{avg}. \tag{3-39}$$

Using the Keplerian period, $T = 2\pi\sqrt{a^3/\mu_\oplus}$, the lifetime for those near circular orbits is approximated as inversely proportional to the semi-major axis, a, and the ballistic coefficient, B, as shown in Eq. 3-40:

$$\Delta t = \frac{\Delta r}{-2B\rho_{avg}\sqrt{\mu_\oplus a}}. \tag{3-40}$$

Elliptical orbits that do not meet the near-circular criteria of $\Delta r/r_p \ll 1$ will experience the majority of drag within a certain portion of the perigee section of the orbit, modifying the eccentricity, e and semi-major axis, a, such that the orbit has a tendency to circularize over time

if no correcting force is applied. Eq. 3-41 shows this change in radius as drag is applied over the range $-\theta_{lim}$ to θ_{lim}

$$\frac{\Delta \mathrm{r}}{\mathrm{rev}} = \left[-\frac{B\rho\left(h_{p0}\right) r_{p0}^2 \exp\left(-k r_{p0} e\right)}{1 + e\cos\theta} \left[2C_1\theta - C_2\theta\cos\theta + \cdots \right] \right]_{-\theta_{lim}}^{\theta_{lim}} . \quad (3\text{-}41)$$

FreeFlyer ® is a Commercial Off-The-Shelf (COTS) software for mission design, analysis, and operations. FreeFlyer ® has been independently verified and validated for flight-tested, proven accuracy, and is used for spacecraft analysis and operations by NASA, NOAA, DoD, and commercial satellite providers. It provides full force modeling capability including but not limited to Solar System celestial bodies, atmospheric drag and lift, solar radiation pressure, and custom forces ("FreeFlyer," 2019). FreeFlyer ®'s full force modeling capability will be applied to the deterministic assessment of lifetime as well as orbital change over time due to perturbations.

3.3.2 Earth geometry viewed from space

Earth coverage is that part of the Earth which an instrument on-board the spacecraft can see at one time. The instantaneous Field of View (FoV) or footprint is what the satellite/instrument can see at that moment. In contrast, the access area or Field of Regard (FoR) is the area the instrument could see if it were scanned instantaneously through its normal range.

FoV and FoR are the building blocks for four important parameters determining coverage. Footprint area, F_A, is the area the instrument can see at any one instant. Instantaneous access area or Instantaneous field of regard, $F_{R,A}$, is the area the instrument could see if it were

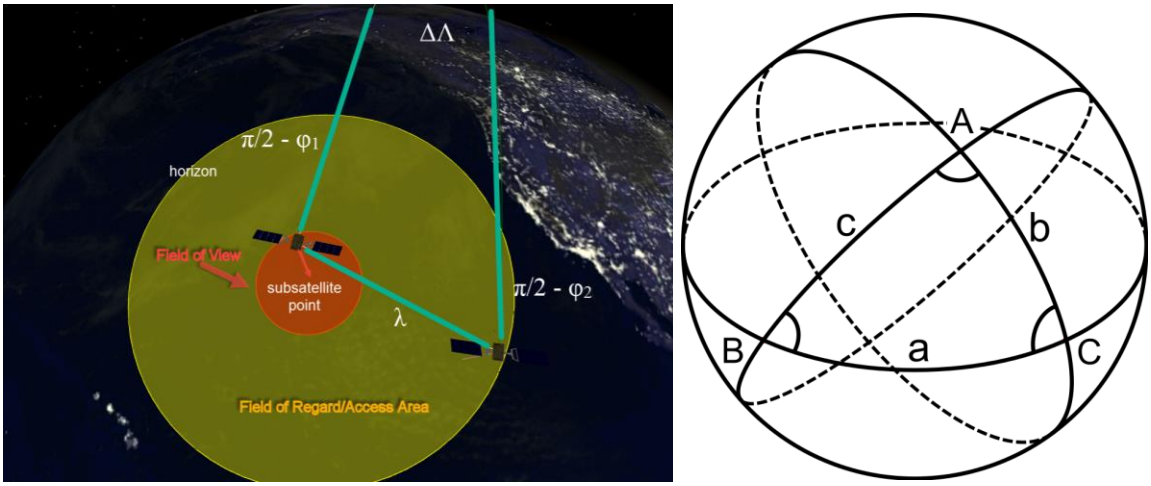

Figure 3-8. Spherical geometry aids in the construction of the satellite FoV and FoR. Difference in longitude can be compared to $A = \Delta\Lambda$, the Earth central angle describing FoR and FoV, $a = \lambda(\epsilon)$, and latitude of each satellite as $c, b = \frac{\pi}{2} - \phi_{1,2}$.

scanned through its normal range of operations instantaneously at that moment in time. Area Coverage Rate A_{CR} is the rate at which the instrument or antenna is sensing or accessing new land. A_{CR} will be determined by the duty cycle of the instrument and the exposure or dwell time of the instrument. Area Access Rate A_{AR} is the rate at which new land is coming into the spacecraft's access area (*Space Mission Analysis and Design*, 2003).

The FoV area or footprint area, F_A, is proportional to the length of the footprint, L_F, and the width of the footprint, W_F. The particular coverage pattern, i.e. rectangular, circular, elliptical, etc., will determine the exact area calculation. The length of the footprint, L_F, is given by Eq. 3-42. The linear approximation, $D \sin\theta \,/\, \sin\varepsilon$, while computationally convient, provides up to 400% error at $\varepsilon = 1°$ and up to 10% error at $\epsilon = 15°$ for an altitude of 1,000 km with a 1 deg diameter beam (*Space Mission Analysis and Design*, 2003).

$$L_F = K_L(\lambda_{FO} - \lambda_{FI}) \approx D \sin\theta \,/\, \sin\varepsilon \tag{3-42}$$

where θ, beamwidth angle, ϵ, elevation angle constraint, D, slant range, λ_{FO}, is the Earth central angle to the toe of the footprint, λ_{FI}, is the Earth central angle to the heel, and K_L is the conversion for a spherical Earth from steriradians.

The footprint width, W_F, is given by Eq. 3-43. Here the error in the approximation is proportional to $1 - (W_F/\sin W_F)$. While th error is negiligible for most applications it bears checking for unique geometries considering the spherical Earth approximation inherent in Eq. 3-43:

$$W_F = R_\oplus \operatorname{asin}\left(\frac{D \sin\theta}{R_\oplus}\right) \approx D \sin\theta. \tag{3-43}$$

If the footprint area, F_A, is an ellipse then the area is given by Eq. 3-44. The error, assuming no approximations made in footprint length, L_F, is proportional to $1 - (W_F/\sin W_F)$:

$$F_A = \left(\frac{\pi}{4}\right) L_F W_F. \tag{3-44}$$

If the footprint area, F_A, is the instantaneous area the instrument sees, the rate at which the instrument/footprint senses new land is given by the Area Coverage Rate, A_{CR}, which is inversely proportional to the dwell time, T, as seen in Eq. 3-45. The average rate is proportional to the duty cycle, DC, and average overlap area, $1 - O_{avg}$ as seen in Eq. 3-46:

$$A_{CR} = \frac{F_A}{T} \tag{3-45}$$

$$A_{CR,avg} = \frac{F_A(1 - O_{avg})}{T/DC}. \tag{3-46}$$

The corresponding measurements for the FoR are the instantaneous field of regard, $F_{R,A}$, all the area that the instrument could see if instantaneously scanned through its normal range of operations, and area access rate, A_{AR}, the rate at which new land enters the FoR. The $F_{R,A}$ depends on the shape of the potential coverage area on the ground. Radar instruments that cannot work too closely to the subsatellite point will have both an outer horizon, λ_1, and inner horizon,

λ_1, that affects the available access area. Using the constant, $K_a = 2\pi$ [rad] = $20626.4806\ [\text{deg}^2] = 2.55604187 \times 10^8 [\text{km}^2]$, Table 3-4, provides the F_A, $F_{R,A}$, A_{CR}, and A_{AR} in the case of an omni-antenna, radar, SAR, or a scanning sensor.

Table 3-4. Coverage formulas for four different patterns. The approximation for footprint area is invalid when $\varepsilon \approx 0$. The A_{CR} for SAR and the scanning sensor assume that the instrument is side-looking, (*Space Mission Analysis and Design*, 2003).

Application	$\boldsymbol{F_A}$	$\boldsymbol{F_{R,A}}$	$\boldsymbol{A_{CR}}$	$\boldsymbol{A_{AR}}$
Omni-antenna,	$\left(\frac{\pi}{4}\right) L_F W_F$	$K_a(1-\cos\lambda)$	$\frac{F_A(1-O_{avg})DC}{T}$	$\frac{2K_a \sin\lambda}{P}$
Radar	$\left(\frac{\pi}{4}\right) L_F W_F$	$K_a(\cos\lambda_2 - \cos\lambda_1)$	$\frac{F_A(1-O_{avg})DC}{T}$	$\frac{2K_a \sin\lambda_1}{P}$
Synthetic Aperture Radar (SAR)	$\left(\frac{\pi}{4}\right) L_F W_F$	$2K_L(\lambda_1 - \lambda_2)$	$\frac{2K_a(\sin\lambda_1 - \sin\lambda_2)}{P}$	$\frac{2K_a(\sin\lambda_1 - \sin\lambda_2)}{P}$
Scanning sensor	$\left(\frac{\pi}{4}\right) L_F W_F$	$K_L(\lambda_1 \pm \lambda_2)$	$\frac{K_a(\sin\lambda_1 \pm \sin\lambda_2)}{P}$	$\frac{K_a(\sin\lambda_1 \pm \sin\lambda_2)}{P}$

The maximum Earth central angle, λ_{max}, or the angle between the satellite position vector to the horizon, is the edge of FoR. Twice the λ_{max} gives the swath width or length of $F_{R,A}$. Given a point P for which the latitude, ϕ_P, and longitude, L_P, is known the fraction of the orbit at which point P is in view during an orbit can be determined. Given Figure 3-8 and Figure 3-9

to help visualize the spherical and planar geometry the time in view over one orbit, $t_{view,\ so}$, is given in terms of the off-nadir angle, η, and λ_{max}.

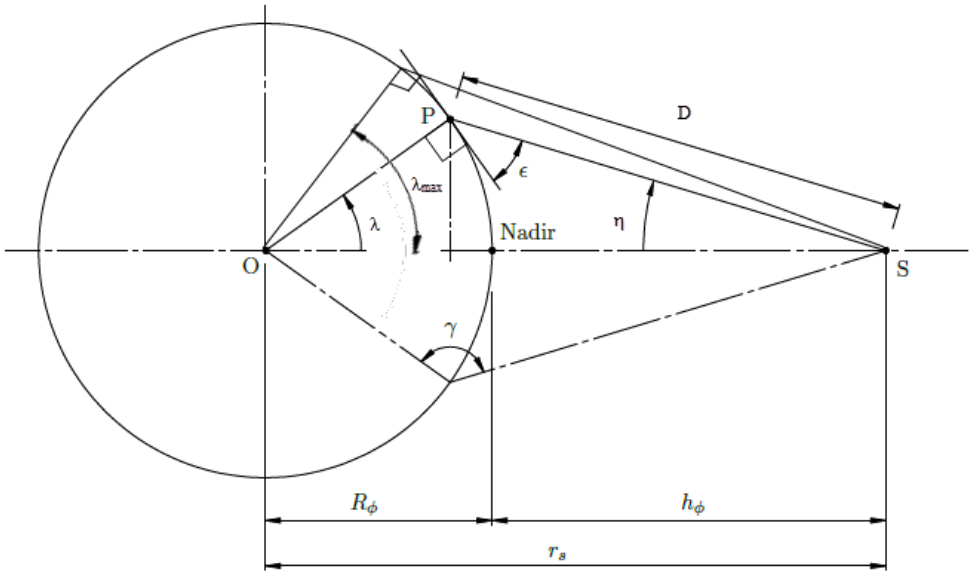

Figure 3-9. Planar geometry of viewing angle given some elevation constraint ϵ. Max Earth central angle, λ_{max}, is determined to find off-nadir angle, η, and finally, the Earth central angle, λ. Adapted from Crisp et al. (Crisp, Livadiotti, & Roberts, 2018).

Assuming elevation constraint, ϵ, is known;

$$\begin{aligned} \sin\rho = \cos\lambda_{max} &= \frac{R_\phi}{R_\phi + h_\phi} \\ \sin\eta &= \cos\epsilon \sin\rho \\ \lambda &= \frac{\pi}{2} - (\epsilon + \eta), \end{aligned} \tag{3-47}$$

where ρ is the angle between the line to the FoR horizon and the satellite radius or the angular radius of Earth seen from the spacecraft. The geocentric angle λ is the the arc between the satellites in Figure 3-9. If $\Delta\nu$ is the change in true anomaly where point P is in view we can determine the time in view over one orbit by multiplying the period by the fraction of orbit as in Eq. 3-48.

$$\cos\Delta\nu = \cos\lambda / \cos\eta$$
$$t_{view,\ so} = 2\pi\sqrt{\frac{a^3}{\mu_\oplus}}\frac{\Delta\nu}{\pi} \tag{3-48}$$
$$t_{view,\ so} = 2\sqrt{\frac{a^3}{\mu_\oplus}}\operatorname{acos}\left(\frac{\cos\lambda}{\cos\eta}\right),$$

where λ is the maximum Earth central angle provided the elevation constraint, ϵ.

Using the law of cosines for spherical trigonometry relationships we can determine the difference in longitude, ΔL, between the two subsatellite points. Eq. 3-49 gives the longitudinal coverage at each latitude, ϕ:

$$\cos\Delta L = \frac{\cos\lambda - \sin\phi_{sat}\sin\phi_P}{\cos\phi_{sat}\cos\phi_P}. \tag{3-49}$$

Wertz et al. provide an analytical prediction of the number of coverage regions for a point P given a circular orbit but does not take into account noncircular orbits, the rotation of the Earth under the spacecraft, or possible overlapping coverage of satellites. Using numerical simulations of coverage will help us determine the percent coverage, maximum gap time for points, and time-averaged gaps. Analytical determination (*Space Mission Analysis and Design*, 2003), is a function of latitude, L, for a satellite in a circular orbit at a certain inclination, i, where $\lambda_{\max}$ is the max Earth central angle. For θ_1 the minus sign applies and for θ_2 the plus sign applies:

$$\cos\theta_{1,2} = \frac{\pm\sin\lambda_{\max} + \cos i\sin L}{\sin i\cos L}. \tag{3-50}$$

Table 3-5. Analytical coverage regions.

Latitude Range	Number of Coverage Regions	Percent Coverage
$L > \lambda_{\max} + i$	0	0
$\lambda_{\max} + i > L > i - \lambda_{\max}$	1	$\theta_1/180$
$i - \lambda_{\max} > L > 0$	2	$(\theta_1 - \theta_2)/180$

As Sugrue and Crisp et al. have shown coverage given nodal precession for both circular and an oblate spheroid can be used to predict coverage of points at a certain latitude, ϕ, (Crisp et al., 2018; Sugrue, 2007). Eq. 3-51 is the precession of the nodes for a circular Earth and Eq. 3-52 for an oblate spheroid using J_2:

$$\delta L = -P_k \omega_{\oplus} \tag{3-51}$$

$$\delta L = P_n\left(-\omega_{\oplus} + \delta\Omega\right), \tag{3-52}$$

where δL is the change in longitude, P_k, Keplerian period, P_n, nodal period, and $\delta\Omega$, precession of right ascension of ascending node due to the oblate spheroid perturbing harmonics like J_2.

$$P_k = 2\pi\sqrt{\frac{a^3}{\mu_{\oplus}}} \tag{3-53}$$

$$P_n = \frac{P_k}{\left[1 + \frac{3J_2R_{eq}}{4p}\left(\sqrt{1-e^2}(2 - 3\sin^2 i) + (4 - 5\sin^2 i)\right)\right]} \tag{3-54}$$

$$\delta\Omega = -\frac{3}{2}nJ_2\left(\frac{R_{eq}}{p}\right)^2 \cos i + \frac{3}{32}nJ_2^2\left(\frac{R_{eq}}{p}\right)^4 \cos i\,[12 - 4e^2 - (80 + 5e^2)\sin^2 i], \tag{3-55}$$

where $p = a(1-e^2)$, the semilatus rectum, R_{eq}, is the equatorial radius of the oblate spheroid, and $n = \sqrt{\mu_{\oplus}/a^3}$, the mean motion.

To determine the t_{view} over the period of analysis, we will determine all longitudinal passes at point P's latitude. Each pass, λ_{ϕ_P}, is checked for visibility by the inequality in Eq. 3-56:

$$L_{\phi_P} - L_P \leq \Lambda. \tag{3-56}$$

The check on the longitudinal sensor range is used to check if point P is in the FoR if passing over longitude, L_{ϕ_P}. The longitudinal passes are determined by checking the longitudinal passes of a single satellite, L_j, multiple planes, L_p, and multiple satellites in each plane, L_s, so that

combining all passes gives the constellation longitudinal passes at the given latitude over the analysis period, L_{ϕ_P}:

$$\left[L_j\right] = L_1 + (j-1)\delta L \text{ for } j = 1, 2, 3 \ldots \left|\frac{t_{simulation}}{P_n}\right| \tag{3-57}$$

$$\left[L_p\right] = \left[L_j\right] + 2\pi m\left(\frac{1}{p} + \frac{f}{t}\right) \text{ for m= 1 to } p-1 \tag{3-58}$$

$$[L_s] = \left[L_j\right] + {}^{l}/_{S}\,\delta L \text{ for } l = 1 \text{ to } s-1. \tag{3-59}$$

where a Walker constellation notation is used for separation, t, total number of satellites, p, number of equally spaced planes, f, relative spacing between satellites in adjacent planes, and s, is the number of satellites per plane. Assuming equal distribution of satellites in planes, $s = t/p$.

Satellite could be ascending or descending for any pass over the target latitude so a pair of longitudes exist for the true anomaly, ν_ϕ:

$$L = \text{atan}\left[\frac{\cos(\omega+\nu_\phi)\sin\Omega + \sin(\omega+\nu_\phi)\cos\Omega\cos i}{\cos(\omega+\nu_\phi)\cos\Omega - \sin(\omega+\nu_\phi)\sin\Omega\cos i}\right] + \frac{\nu_\phi}{2\pi}\delta L. \tag{3-60}$$

3.3.3 Constellation Coverage Analysis

Common figures of merit for Earth observation include percent coverage, C_{per}, maximum coverage gap, G_{max}, mean response time, G_{mrt}, and the time averaged gap, G_{avg}. Satellite navigation for for Precision Navigation, and Timing (PNT) uses Dilution of Precision (DoP), σ, a geometric factor multiplied by measurements and other input to give the error in position or time. In the case of moving targets, G_{mrt}, will be modified to capture the mean rate of track, the average length of time a single moving target is tracked.

A fixed target observation makes determination of the figures of merit by the difference in time of passes able to observe the fixed target P, or those meeting Eq. 3-56. Given the time of

each pass meeting Eq. 3-56, Eq. 3-61 gives the gap duration, G, between each pass where P is in view:

$$G = t_{\phi_{P_j}} - t_{\phi_{P_{j-1}}} \text{for } j = 1, 2, 3, \ldots \tag{3-61}$$

Given the gap duration over the entire analysis or simulation time frame, t_{sim}, we can determine the total time in view, t_{view}, percent coverage, C_{per}, maximum coverage gap, G_{max}, mean response time, G_{mrt}, and the time averaged gap, G_{avg}:

$$G_{max} = \max\left(t_{\phi_{P_j}} - t_{\phi_{P_{j-1}}}\right) \text{for } j = 1, 2, 3, \ldots \tag{3-62}$$

$$G_{mrt} = \frac{1}{N}\sum_{j=1}^{N}\left(t_{\phi_{P_j}} - t_{\phi_{P_{j-1}}}\right) \tag{3-63}$$

$$G_{avg} = \frac{1}{t_{\phi_{P_N}} - t_{\phi_{P_0}}}\sum_{j=1}^{N}\left(t_{\phi_{P_j}} - t_{\phi_{P_{j-1}}}\right)^2 \tag{3-64}$$

$$C_{per} = \frac{1}{t_{\phi_{P_N}} - t_{\phi_{P_0}}}\sum_{j=0}^{N} t_{view_j} = \frac{\sum_{j=0}^{N} x_j}{N}. \tag{3-65}$$

Eqns. 3-62-65 are estimators of the population parameters. Eq. 3-63 is the sample mean or a point estimator of the population mean response time, G_{mrt}. Eq. 3-64 is similar to the unbiased estimator for standard variance except the squared difference is divided by the simulation/analysis time instead of the number of samples minus one (Wackerly, Mendenhall III, & Scheaffer, 2008).

Using the time-of-arrival (TOA) the pseudorange between participants in a network can be determined in Eq. 3-66. DoP, σ, and network quality combined with estimates of inertial measurements onboard vehicles is useful in determining the quality of solution. Reducing the covariance matrix of the receiver solution by assuming equal and independent measurement and model errors, $C_{\Delta x} = (A^T A)^{-1}\sigma^2 = D\sigma^2$, where σ represents the standard deviation of the

psuedorange measurement error plus the residual model error, we can obtain a measurement of the overall quality of the solution:

$$\tilde{\rho} = \rho + d_{prop} + e \tag{3-66}$$

$$\sigma_G = \sqrt{\sigma_E^2 + \sigma_N^2 + \sigma_U^2 + \sigma_T^2} = \sqrt{tr(D)}\sigma. \tag{3-67}$$

The scaling factor, $\sqrt{tr(D)}$, a function of receiver and transmitting satellites positions and clock offsets, dilutes the precision of the position determination amplifying the pseudorange error. This scaling factor is called the geometric dilution of precision. Using the four minimum satellites, the lowest possible geometric DoP, σ_G is 1.732 which is directly correlated with the tetrahedron volume formed by the receiver to satellite unit vectors. Given a single frequency receiver, user equivalent range error is about 25 m. The position error, for the best minimum satellite solution, would be about 43.3 m.

For those moving targets the performance parameters are updated use the viewing time. The maximum gap duration, G_{max}, remains the same as the minimum viewing time will be an equivalent measurement. The time averaged gap also remains the same because we prefer to minimize the gap duration:

$$G_{mrt} = \frac{1}{N}\sum_{j=1}^{N}\left(t_{view_j} - t_{view_{j-1}}\right) \tag{3-68}$$

$$G_{avg} = \frac{1}{t_{\phi_{P}N} - t_{\phi_{P}0}}\sum_{j=1}^{N}\left(t_{\phi_{P}j} - t_{\phi_{P}j-1}\right)^2. \tag{3-69}$$

Eq. 3-69, after its moving target update, must be maximized to minimize gap duration.

3.4 Optimization

Minimization of the reaction time, or overall time to deploy the constellation and reach first light, is the primary goal. Additionally, equal weight must be given to the coverage quality of the constellation, whether as a satellite navigation replacement or providing ISR on-demand. The constellation must be available over a certain time period requiring a lifetime constraint. Two fundamental optimal problems represent the scheduling problem to see first light as quickly as possible while attempting to provide continuous or near-continuous coverage.

3.4.1 Reaction time

An expression for the reaction time is compiled for the first satellite in the constellation to see the target requested:

$$t_{rt} = \left[\frac{\tanh^{-1}\left(V_{to}\sqrt{\frac{B}{A}}\right)}{\sqrt{AB}} + \frac{V_3 - V_{to}}{S_a - S_g}\right] + \left[\frac{1}{a}(\ln(ah_2 + b) - \ln(ah_1 + b))\right] + [(\Delta t_{BO2} - t_L)] + \left[t_{\phi_{P_0}}\right]. \quad (3\text{-}70)$$

Eq. 3-70 combines the take-off and climb time for the aircraft, the final burn-out time of the second stage after the launch time, and the time of the first pass after injection into orbit. The major reductions to be gained in reaction time are from the aircraft climb time, launch vehicle flight time, and first pass time. Aircraft climb time is reduced by selection of a tactical and/or high-performance aircraft. Launch vehicle time is reduced by aircraft release speed and vehicle performance. The time to orbit from launch vehicle drop to satellite injection is constrained by the mission lifetime. Uncertainty characterization for the lifetime of LEO nanosatellites was examined by (Dell'Elce et al., 2015). The orbital lifetime of the spacecraft is directly dependent upon the initial orbital parameters. The time until the first pass is a function of the true anomaly at injection. True anomaly is determined by the launch vehicle orbit injection location and is a

scheduling for the optimizer choice given the minimum pass distance of the launching facility location.

3.4.2 Coverage Quality

Due to the nature of the coverage parameters, percent coverage of any target, will be maximized for those minimized gap duration parameters, i.e. where coverage time is maximized. The time averaged gap duration, G_{avg}, is a biased estimator of the gap duration variance given the sample population. Eq. 3-71 illustrates this by discretizing the continuous time, where N_t is the total number of time steps, not the total number of viewed passes N:

$$G_{avg} = \frac{1}{N_t}\sum_{j=1}^{N}\left(x_{\phi_P j} - x_{\phi_P j-1}\right)^2. \tag{3-71}$$

Taking the squared difference in time steps where the point P is visible dividing by the total number of time steps we confirm the conjecture that G_{avg} is a sample gap duration variance estimator. It is desirable that for some given gaps G they are mostly similar or equal in time, as opposed to experiencing an abnormal schedule of viewing times.

Reducing or minimizing the maximum gap duration, G_{max} and mean response time, average gap, G_{mrt}, will have the tendency to reduce gap duration overall, G. Minimizing G will be accomplished by scheduling and/or phasing the fixed number of satellites to provide the best coverage possible. In the case of DoP, σ, continuous coverage becomes a requirement, such that $G_{mrt} = G_{max} = G = 0$. σ will be the driver in phasing and orbital element modification to attempt to provide at least four satellites overhead for as long as possible. In our use cases, network and inertial navigation systems (INS) provide additional inputs to the target area for position estimation. The four satellite constraint may be relaxed in those cases.

3.4.3 Optimal control

The optimization problem can be described as;

- determination of the minimum reaction time
- maximize coverage quality

given a range of possible orbits that each launch vehicle can inject a satellite into. The objective functions' derivatives are complex especially for determination of minimum reaction time. A bound constrained optimization strategy without derivatives will be used.

Quadratic approximation to find the minimum of a function $f_0(x)$ for $x \in \mathcal{R}^n$, subject to bounds $a \leq x \leq b$, is accomplished via the iterative algorithm BOBYQA (Powell, 2009). The iterative method uses the variables, k, iteration number, n, number of variables, and m for the number of interpolation conditions imposed on a quadratic approximation $Q_k(x)$ to $f_0(x)$ where both $x \in \mathcal{R}^n$:

$$Q_k(y_j) = f_0(y_j) \text{ for } j = 1, 2, 3, \dots, m \tag{3-72}$$

$$f_0(x_k) = \min\left[f_0(y_j) : j = 1, 2, 3, \dots, m\right]. \tag{3-73}$$

where m is a constant integer from the interval $[n + 2, (n + 1)(n + 2)/2]$ chosen at the beginning of the procedure, and x_k satisfies Eq. 3-73. If termination conditions are not achieved on the kth iteration a step d_k from x_k is constructed using $|d_k| \leq \Delta_k$, where Δ_k is the positive trust region radius:

$$x_{k+1} = \begin{cases} x_k & f_0(x_k + d_k) \geq f_0(x_k) \\ x_k + d_k & f_0(x_k + d_k) < f_0(x_k) \end{cases} \tag{3-74}$$

$$y_j = \begin{cases} y_j & j \neq t \\ x_k + d_k & j = t. \end{cases} \tag{3-75}$$

where t is one of the interpolation points selected for replacement.

No derivative information for the relationship between coverage quality and orbital parameters required use of a non-derivative method. Desire for a local solution minima allowed

selection of BOBYQA for its performance given other methods tried in NLopt. BOBYQA is a direct search method that gradually reduces the interval for the state variables that it modifies to find the solution. BOBYQA is in the NLopt library that FreeFlyer® is compatible with. BOBYQA does not require derivative information. BOBYQA approximates the objective function and its derivatives to the second order. The method employed is an improvement over the Constrained Optimization BY Linear Approximation which struggles to find a solution when more than nine state variables are used. BOBYQA provides solutions to all cases for scheduling, given the relationship between constellation relative spacing and launch timing, to optimizing coverage quality to some local minima. BOBYQA was selected because of its availability in the NLopt library and the easy interface between the modeling software FreeFlyer® and the library. This made combination of the vehicle models and optimization routine easy.

To minimize reaction time;

- select an orbit intersecting target and launch location
- minimize launch vehicle time of flight
- minimize time of injection to first pass

which translates to a constraint on launching azimuth, η_L, and suggests some trade-off between aircraft time to achieve maximum speed and release time. An orbit intersecting target and launch location will meet the longitudinal constraints of Eq. 3-76 and 77:

$$L_j = L_\phi + (j-1)\left(1 - \frac{\phi_L}{2\pi}\right)\delta L \text{ for } j = 1, 2, 3, \ldots \left|\frac{t_{sim}}{P_n}\right| \tag{3-76}$$

$$L_j - L_P \leq \Lambda. \tag{3-77}$$

By modifying launch location, $[\phi_L, L_L]$, height of release, h_L, and speed of release, v_L, the reaction time is minimized where Eq. 3-78 gives the time of the initial pass:

$$t_{RT} = \frac{\omega + \nu_\phi}{2\pi} P_n + \Delta t_{BO2}. \tag{3-78}$$

Coverage quality is maximized when gap duration, G, is minimized. Geometric DoP, σ_G, is minimized as increasing numbers of satellites cover the same region with continuous coverage.

$$f_0(G,\sigma) = y_0\left(\frac{1}{N}\sum_{j=1}^{N}\left(t_{\phi_{P}j} - t_{\phi_{P}j-1}\right) + \frac{1}{t_{\phi_{P}N} - t_{\phi_{P}0}}\sum_{j=1}^{N}\left(t_{\phi_{P}j} - t_{\phi_{P}j-1}\right)^2\right) + y_1\left(\frac{1}{N}\sum_{j=1}^{N}\left(t_{view_j} - t_{view_{j-1}}\right) + \frac{1}{t_{P_N} - t_{P_0}}\sum_{j=1}^{N}\left(t_{P_j} - t_{P_{j-1}}\right)^2\right) + y_2\left(\sqrt{tr(D)}\sigma\right), \tag{3-79}$$

where $y_i = [0, \pm 1]$ depending if the request is ISR of a stationary target, y_0, ISR of a moving target, y_1, or requested satellite navigation/communication coverage of the target, y_2.

4. DISCUSSION

The mission planning system optimizing on-demand constellations delivered from tactical airborne platforms is examined at length. Sensitivity of the scheduler to facility location, vehicle performance, and initial orbital parameters is examined. Four case studies, representing operational scenarios are presented. The four cases demonstrate operational solutions for the military, disaster response, and rapid science return. Varying the coverage requirements in each case allows an in-depth examination. Facilities and number of available satellites are fixed. Optimization in facility location and satellite availability are eliminated to focus on schedule optimization. Each case makes assumptions about naval vessel speed, heading, and capabilities, available facilities, including aircraft carriers, to deploy tactical fighters and commercial variants carrying launch vehicle(s), and aircraft and launch vehicle performance.

4.1 Verification

Aircraft climb performance estimation using specific excess power is verified. Launch vehicle maximum performance is verified using known rocket motor/engine performance and the estimated performance cost to achieve orbit from an airborne platform. Coverage quality estimation is verified using geosynchronous spacecraft, a known continuous coverage solution.

4.1.1. Aircraft climb performance

Detailed performance of the F-35 Lightning II aircraft is not publicly available. An F-16 Fighting Falcon/Viper weighing 21,737 lbs under a 1.0 g load, specific excess power, P_s, contour plot is used for all three variants of the F-35 Lightning II. The specific excess power, P_s, contour

plot is representative of the F-35 variants providing insight into the time to reach the launch vehicle release point.

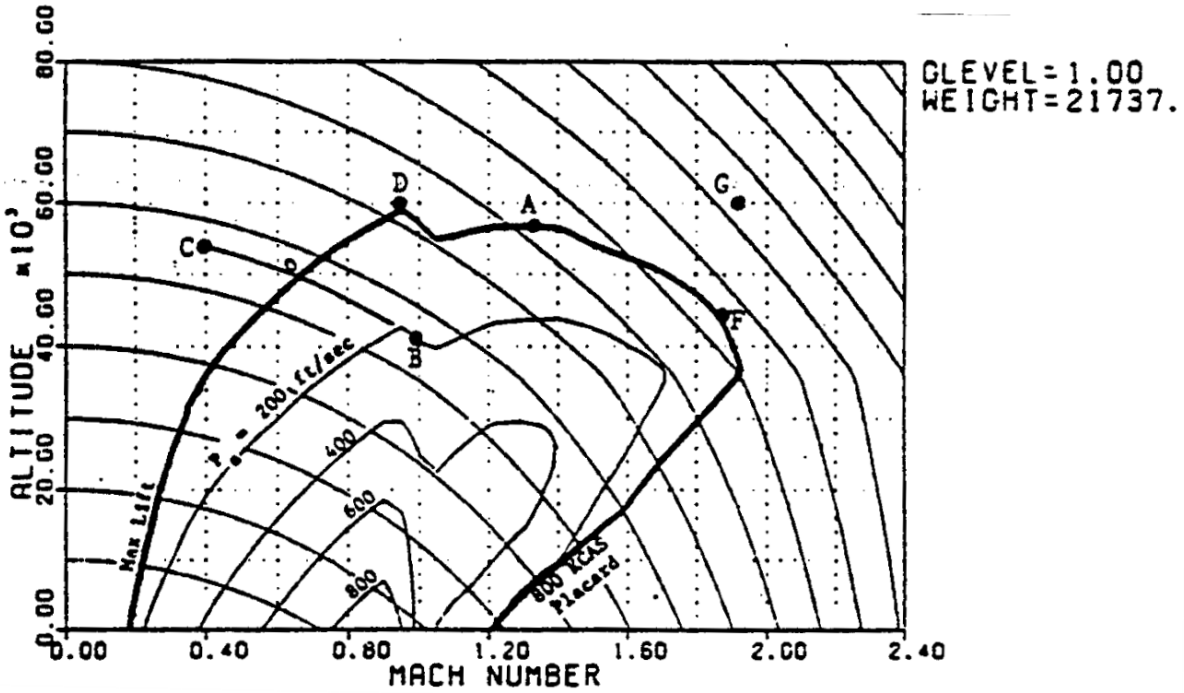

Figure 4-1. F-16 specific excess power, P_s, contour plot given altitude and speed. (School, 1991)

Thrust information for the F-35 Lightning II variants is not complete. For the P_s model where T information is not fully available we assume a linearly decreasing rate of climb as altitude increases so that $dh = f(h)\,dt$, where $f(h)$ is approximated by $ah + b$. b is the sea level rate of climb and a is the slope of the linearly decreasing rate of climb.

$$t_{climb} = \frac{1}{a}(\ln(ah_2 + b) - \ln(ah_1 + b)) \tag{4-1}$$

Using Figure 4-1, the F-16 P_s contour plot, and publicly released information on F-35 variant capabilities, the sea-level $P_{s,ssl}$ is estimated to be 48,000 fpm(Canin, McConnell, & James, 2019; Hamstra & McCallum, 2010; Wiegand et al., 2018). The ceiling of an aircraft is

defined as the altitude at which the steady rate of climb is reduced to 100 fpm. The F-35 variants' ceilings are 60,000 ft.

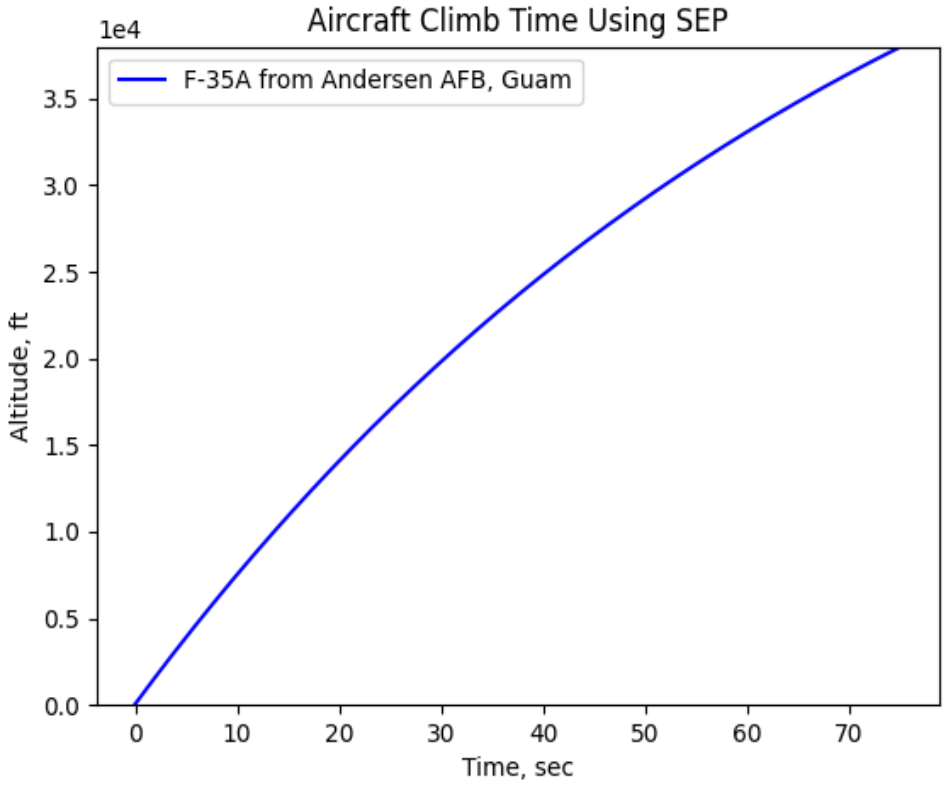

Figure 4-2. All F-35 variants' climb times are equal at the same facility. Facility altitude will affect climb time by changing the starting altitude of the climb.

Equal climb time by different variants at the same facility, see Andersen AFB, is expected. The same sea-level rate of climb, $P_{s,ssl}$, is used for all F-35 variants. The starting altitude of the facility affects the climb time. The deck height of the USS Carl Vinson, CVN-70, and HMS Queen Elizabeth are nearly equal. The same starting altitude means the aircraft launched from each ship have nearly the same climb time.

Table 4-1. Facility altitude affects time to climb to 38,000 ft and reach $M_\infty = 1.6$.

Facility	Aircraft	h_{MSL} [ft]	x_{climb} [ft]	t_{climb} [sec]
USS Carl Vinson (CVN-70)	F-35C	38,000	111,390	74.386

Eielson AFB, Alaska, USA	F-35A	38,000	113,766	72.549
MCAS Iwakuni, Japan	F-35B	38,000	113,407	75.026
Maxwell AFB, Alabama, USA	F-35A	38,000	113,730	74.279
Andersen AFB, Guam	F-35A/F-35B	38,000	113,459	72.225
Ørland Air Station, Norway	F-35A	38,000	113,717	74.933
HMS Queen Elizabeth (R08)	F-35B	38,000	111,520	74.386

4.1.2. Launch vehicle performance

Two position vectors and a time-of-flight between the two vectors are necessary to solve Lambert's theorem. Lambert's theorem solves for the velocity at each position vector providing an estimate of the energy cost or change in speed, ΔV. The aircraft release point or drop zone will determine the first position vector. The second position vector is given by the estimated orbit injection point. The time-of-flight is affected by the performance of the two-stage launch vehicle rocket engines and the phasing employed for coverage quality within the requested orbit.

An aircraft releases the launch vehicle at a location of r_1. The launch vehicle traveling at $M_\infty = 1.6$ ignites its engine. The launch vehicle completes first stage flight and ignites the second stage. The second stage injects the launch vehicle and satellite into the orbit at r_2.

An example intercept problem from Dr. Matthew Peet (Peet) is used to verify the time-of-flight and delta-v, ΔV, calculation using Lambert's theorem. "An interceptor is in the air with position and velocity of $r_i(t_1) = [6045, 3490, 0]$ km and $v_i(t_1) = [-2.457, 6.618, 2.533]$ km/s. An Inter-Continental Ballistic Missile (ICBM) is tracked at $r_t(t_1) = [12214.839, 10249.467, 2000]$ km and $v_t(t_1) = [-3.448, 0.924, 0]$ km/s." The problem is modified to treat the interception as a rendezvous, increasing the ΔV, and adding a delay, effectively changing the start time, t_1, of the interceptor only. The ΔV is calculated for rendezvous case to verify the solution. The interceptor case at a fixed time-of-flight of 30 minutes is calculated for a total impulse of 6 km/s and confirmed with code modification. The

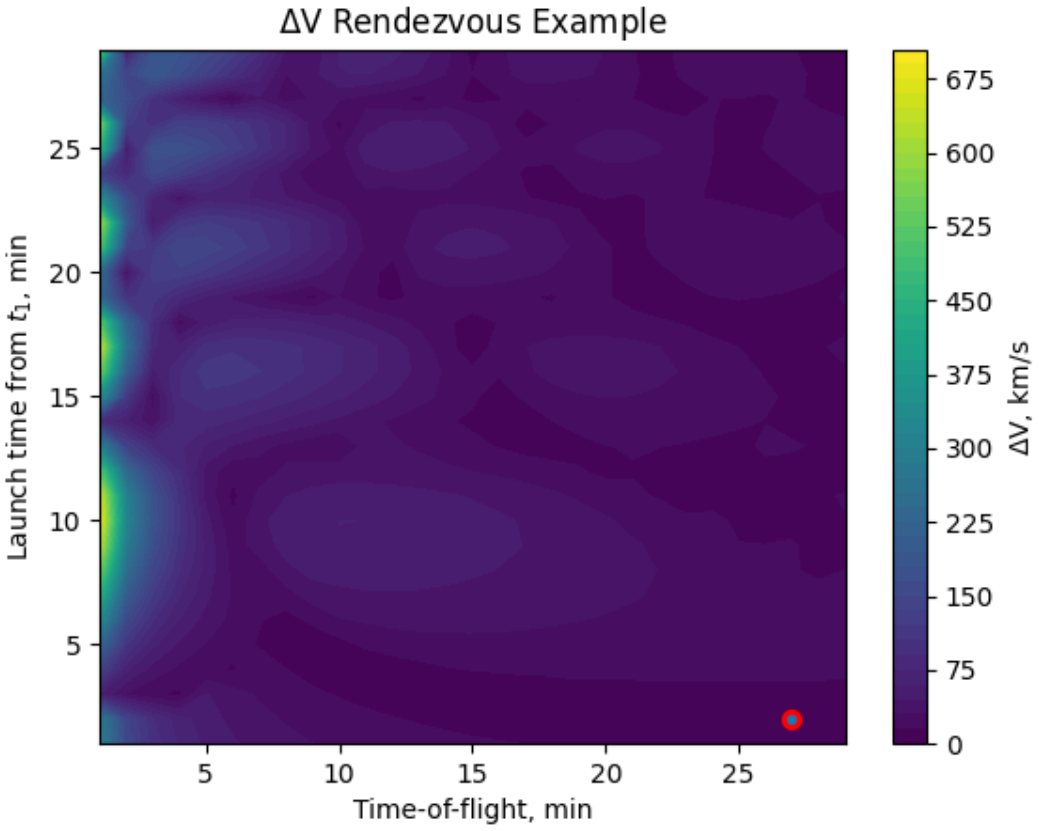

Figure 4-3. Total impulse, ΔV, of a maneuver is dependent on start time and time-of-flight. Local minimum $\Delta V = 3.44$ km/s to rendezvous with the launched ICBM is circled.

rendezvous with no delay and at 30 minutes time of flight requires an impulse of 8.50 km/s. Delaying the rendezvous launch by two minutes, and modifying the flight time for 27 minutes the total impulse, ΔV, is minimized to 3.44 km/s.

4.1.3 Geosynchronous spacecraft coverage

A geosynchronous spacecraft provides a known continuous coverage solution of a fixed target. The geosynchronous spacecraft is used to verify the objective function. The fixed target is Mischief Reef, 9°54′0"N and 115°32′0"E, in the South China Sea. The objective function is Eq. 4-2, adding the mean gap duration, G_{mrt}, and the time-averaged gap, G_{avg}. Eq. 4-2 will go to zero, $f_0(G,\sigma) = 0$, with successful verification of the continuous coverage case:

$$f_0(G,\sigma) = \left(\frac{1}{N} \sum_{j=1}^{N} \left(t_{\phi_P j} - t_{\phi_P j-1} \right) + \frac{1}{t_{\phi_P N} - t_{\phi_P 0}} \sum_{j=1}^{N} \left(t_{\phi_P j} - t_{\phi_P j-1} \right)^2 \right). \tag{4-2}$$

As shown in Figure 4-4 the objective function is minimized, $f_0(G,\sigma) = 0$, by the trivial solution of a geosynchronous spacecraft. FreeFlyer® v7.6 NLopt engine does not capture any solution as the best solution when provided a local solution. FreeFlyer® v7.6 Ipopt engine exhibits the same behavior suggesting a lack of foresight for providing initial local solutions. Two possible solutions are available.

1. Calling FreeFlyer® from the API, use the orbit coverage calculation as the objective function provided to the NLopt solver.
2. Using the FreeFlyer® script, confirm a local solution has been provided and exit.

The second solution has been used for this work. The intention is to deliver a fast optimized schedule. If a local solution has already been provided there is no need for further optimization. The aircraft and launch vehicle will already be operating inside their constrained bounds.

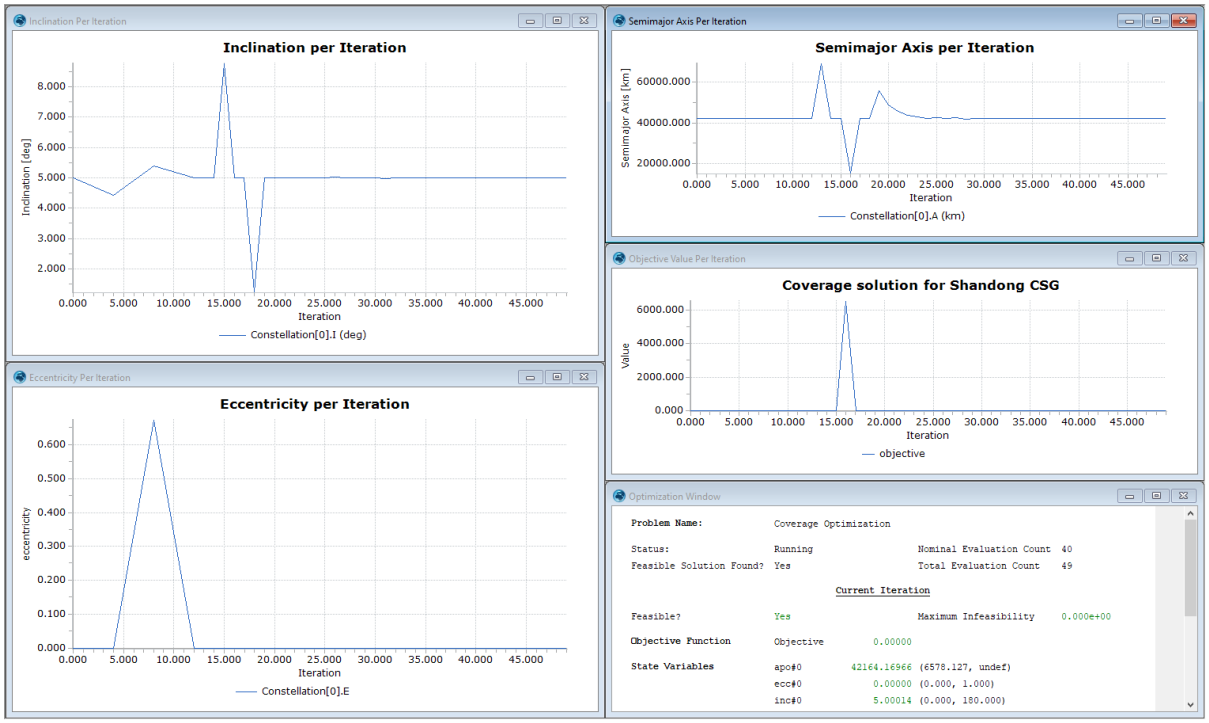

Figure 4-4. FreeFlyer® v7.6 output for optimization of a single geosynchronous spacecraft coverage of a moving target over three hours.

If a local solution is delivered to the FreeFlyer® optimization engine, minimization of reaction time will be delivered at a much faster CPU time. Coverage of the geosynchronous spacecraft of the moving Shandong CSG is shown in Figure 4-5. Fixed facilities are shown with

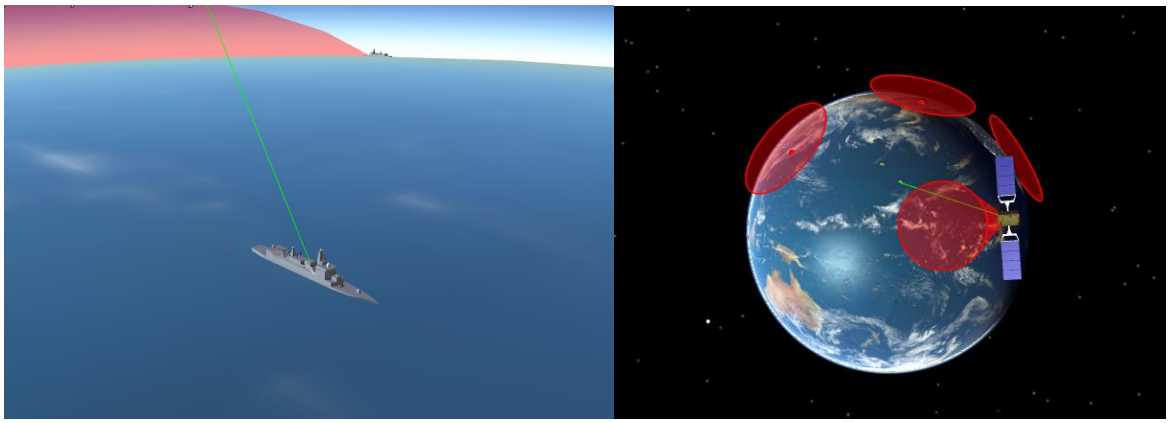

Figure 4-5. A single geosynchronous spacecraft coverage of a moving target visualized in FreeFlyer®. The green vector is active when the target is within the sensor field of view.

elevation masks case study coverage solutions.

4.2 Validation

Coverage quality estimation for constellation installation is validated against real-world coverage. GPS satellite Two-Line Elements (TLEs) are used to estimate geometric DoP over two different locations and compared against the mission planning system's estimate of geometric DoP. Lockheed Martin F-35 Lightning II aircraft are validated using the Specific Excess Power (SEP) figures available.

4.2.1 GPS Dilution of Precision (DoP) for a fixed target

The geometric, position, horizontal, vertical, and time dilution of precision are estimated by the commercial off-the-shelf software FreeFlyer ®. FreeFlyer is used in mission planning and

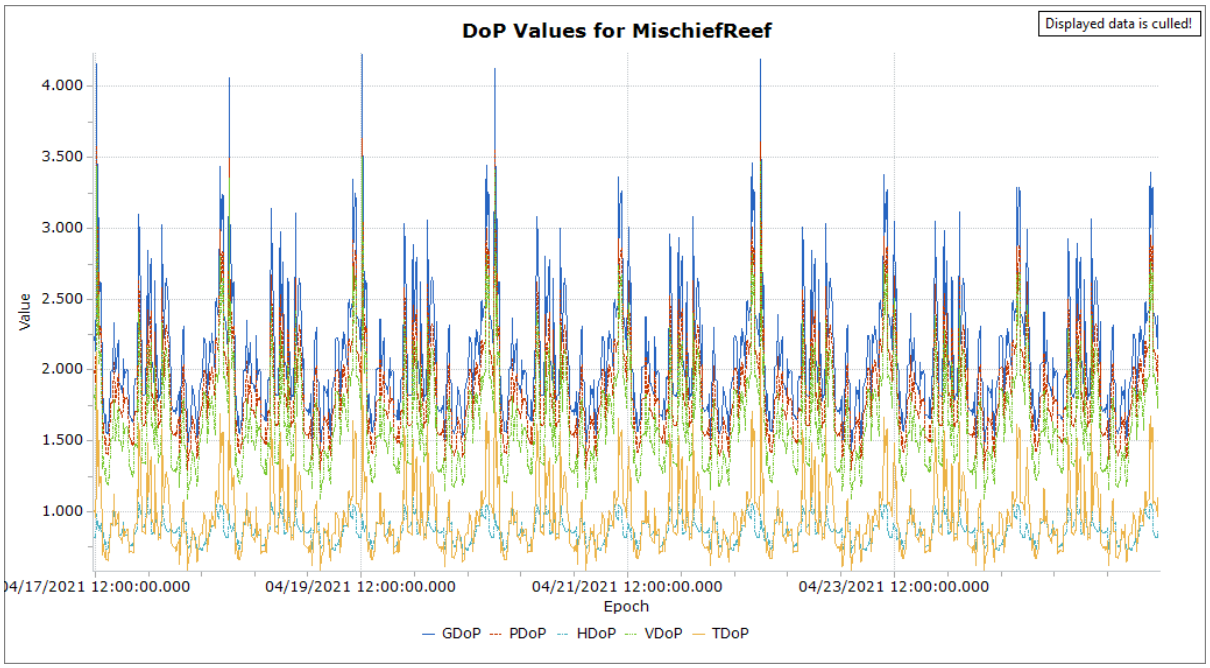

Figure 4-6. Geometric Dilution of Precision (DoP) at Mischief Reef calculated over an eight day span, April 17-21, 2021, from Two-Line Elements (TLEs) of the GPS constellation.

real satellite operations. Operational GPS satellite Two-Line Elements (TLEs) are downloaded via a TCP/IP socket connection and propagated for the requested time to demonstrate expected measurements of DoP as shown in Figure 4-6.

The TCP/IP socket connection uses Celestrak because the socket connection cannot provide a username and password when prompted to by Space-Track's API. The TLEs are copied into a string array and loaded into the GPS formation object. Propagating the GPS constellation forward in time over an eight day span the DoP is calculated at each time step.

Dilution of Precision Calculation for Operational GPS Satellites

```
Define Procedure CalcDoPUsingMatrix(Array arrElevation, Array arrAzimuth,
Array arrDoPValues, Variable vNumVisibleGPS);

      Variable j;
      Matrix H;

      // Write first line of Matrix
      // Note: Matrix H is created in the Object Browser and set to
"Global" so it can be used in this procedure
      H = [ cos(arrElevation[0])*sin(arrAzimuth[0]),
cos(arrElevation[0])*cos(arrAzimuth[0]), sin(arrElevation[0]), 1];

      For j = 1 to vNumVisibleGPS - 1;
            // Use the Resize() method to add another row (of zeros) to the
matrix for each GPS that is visible
            H.Resize(j+1,4);
            H[j,:] = [cos(arrElevation[j])*sin(arrAzimuth[j]),
cos(arrElevation[j])*cos(arrAzimuth[j]), sin(arrElevation[j]), 1];
      End;

      // H is now an N-Row x 4-Column Matrix, which will be transposed and
multiplied by itself, resulting in a 4x4 matrix
      H = H.Transpose() * H;

      // Take the inverse of the new H Matrix
      H = H.Inverse;

      arrDoPValues[0] = sqrt(H.Diagonal.Sum()); // Shortcut for summing all
the diagonals of a matrix
      arrDoPValues[1] = sqrt(H[0,0] + H[1,1]);
      arrDoPValues[2] = sqrt(H[0,0] + H[1,1] + H[2,2]);
      arrDoPValues[3] = sqrt(H[2,2]);
      arrDoPValues[4] = sqrt(H[3,3]);

EndProcedure;
```

Compare the procedure to Eq. 4-3, where the DoP is a scaling factor for the position uncertainty. The geometric DoP, σ_G, is the trace of the H matrix:

$$\sigma_G = \sqrt{\sigma_E^2 + \sigma_N^2 + \sigma_U^2 + \sigma_T^2} = \sqrt{tr(D)}\sigma. \tag{4-3}$$

Reducing the covariance matrix of the receiver solution by assuming equal and independent measurement and model errors, $C_{\Delta x} = (A^T A)^{-1}\sigma^2 = D\sigma^2$, where σ represents the standard deviation of the psuedorange measurement error plus the residual model error, we can obtain a measurement of the overall quality of the solution. The H matrix is equivalent to the D matrix given by Eq. 4-3.

4.2.2 GPS Dilution of Precision (DoP) for a moving target

The GPS constellation DoP is measured for Shandong Carrier Strike Group (CSG) moving at 50 knots over three hours from a starting location of 21°42'30"N and 175°06'58"W. Note the effect of the simulation period on the DoP measurements when comparing Figure 4-7 with Figure 4-6. Selecting a different starting epoch for the CSG could mean different DoP

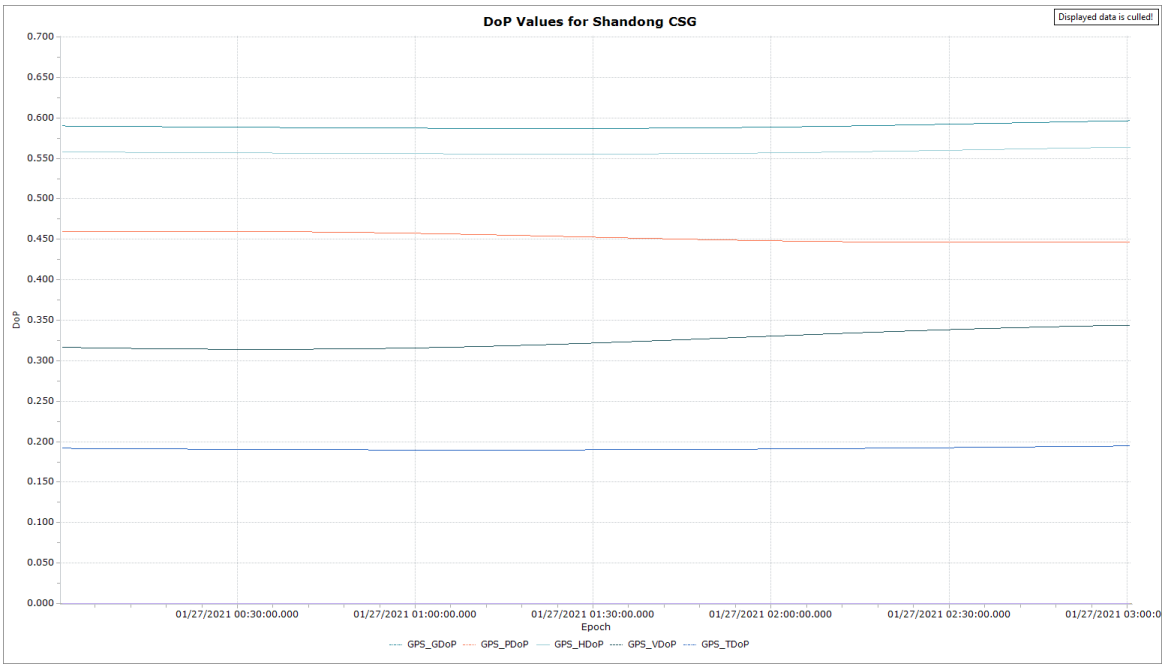

Figure 4-7. Dilution of Precision (DoP) for Shandong Carrier Strike Group (CSG) calculated over a 3-hour span from Two-Line Elements (TLEs) of the GPS constellation.

measurements.

The geometric DoP, the uncertainty of the position and timing combined, is calculated the same way as the fixed target at Mischief Reef. At each time step the DoP procedure is called. Four

satellites must be in view to determine the DoP. A solution for coverage of the CSG will need to provide at minimum four satellites over-head at as soon as possible.

4.2.3 Takeoff estimation

Two F-35B Lightning IIs, from VMFA-121, with no external stores or hardpoints took off from Andersen Air Force Base (AFB) on 16 September 2018. Both aircraft made conventional takeoffs with no visible thrust deflection (Gopinath, 2018). Andersen AFB features two parallel 11.2 kft runways at an altitude of 618 ft above sea-level. Both aircraft completed their ground run just after the 8 kft runway remaining sign. The aircraft completed a takeoff rotation, or pitch-up, by deflecting the horizontal tail surfaces upward just after the 8 kft runway remaining sign. Conditions appear sunny with scattered clouds suggesting an afternoon takeoff from historical weather reports. Weather data on 16 September 2018 is provided by Guam

Figure 4-8. Second F-35B Lightning II of the two-ship from VMFA 121 just prior to takeoff rotation at Andersen Air Force Base, Guam. (Gopinath, 2018)

International Airport at an altitude of 305 ft above sea level, atmospheric pressure of 29.75 in Hg and dry-bulb temperature of 87.1°F.

The following assumptions were made to simplify and reduce takeoff variables;

1. No wind, $V_w = 0$
2. No runway slope, $\gamma_R = 0$
3. Standard day net thrust is equal to observed net thrust, $F_{n_t}/F_{n_s} = 1$

Takeoff day conditions are standardized to compare the standard day ground roll, S_{g_s}, to the observed ground roll, S_{g_t}, by the two F-35Bs. The correction to standardize the observed ground roll is given by Eq. 4-4.

$$S_{g_s} = S_{g_t}\left(\frac{W_s}{W_t}\right)^{2.3}(\sigma_t)\left(\frac{F_{n_t}}{F_{n_s}}\right)^{1.3} \tag{4-4}$$

Observed ground run distance is approximately 3,200 ft, $S_g \approx 3200$ ft. The F-35B's were taking-off to participate in Valiant Shield 18. The density correction, σ_t, for the non-standard day at 618 ft altitude MSL is $\sigma_t = 0.982$. Assuming 100% internal fuel and 3,700 lbs of internal stores during a standard day at 618 ft altitude, the predicted ground roll distance is $S_{g,p} = 3{,}098$ ft and $t_g = 21$ sec.

Table 4-2. Observed ground roll compared against predicted with internal store weight.

Ground distance, S_g (ft)	**Ground time,** t_g (sec)	**Altitude**, h (ft)	**Pressure**, P (in Hg)	**Temperature,** T (°F)
≈3,200	≈21	618	28.77	87.1
3,098	21	618	29.25	56.8

The test day and standard day net thrust could have been different given the ambient pressure and temperature difference. Adding the stores to the take-off prediction we achieve a relative error in distance and time of -3.0% and 0.0%, respectively.

4.3 Coverage Analysis

A discretized coverage example is used to show the strengths, weaknesses, and tendencies of the figures of merit and objective function. The objective function selection is further validated by comparison between the analytical coverage estimates given by Wertz et al., (*Space Mission Analysis and Design*, 2003), and the semi-analytical estimates by Crisp et al. (Crisp et al., 2018). The semi-analytical estimate of coverage is provided as an initial guess to the numerical optimizer. The numerical optimizer capabilities are examined at length through the four case studies in the following section.

4.3.1 Coverage quality in discrete time

The objective function is constrained by the visit count within FreeFlyer ®. FreeFlyer ®'s lack of a "NULL" value requires counter arrays to be filled with zeros. Optimization of constellation coverage requires a software constraint of at least one visit over the target. The objective is minimized artificially without this constraint.

The time-averaged gap, G_{avg}, and mean response time, G_{mrt}, are added to calculate the objective function in seconds. The time-averaged gap duration, G_{avg}, behaves like a biased variance estimator. The mean response time, G_{mrt}, is the mean or expected value of the gap duration. As time-averaged gap, G_{avg}, and mean response time, G_{mrt}, are reduced the gaps will become more consistent and shorter in duration.

$$f_0(G,\sigma) = y_0\left(\frac{1}{N}\sum_{j=1}^{N}\left(t_{\phi_{P_j}} - t_{\phi_{P_{j-1}}}\right) + \frac{1}{t_{\phi_{P_N}} - t_{\phi_{P_0}}}\sum_{j=1}^{N}\left(t_{\phi_{P_j}} - t_{\phi_{P_{j-1}}}\right)^2\right) + y_1\left(\frac{1}{N}\sum_{j=1}^{N}\left(t_{view_j} - t_{view_{j-1}}\right) + \frac{1}{t_{P_N} - t_{P_0}}\sum_{j=1}^{N}\left(t_{P_j} - t_{P_{j-1}}\right)^2\right) + y_2\left(\sqrt{tr(D)}\sigma\right) \tag{4-4}$$

Coverage time and percent coverage, C_{per}, of any target are maximized when gap duration parameters like time-averaged gap, G_{avg}, and mean response time, G_{mrt}, are minimized. The time averaged gap duration, G_{avg}, is a biased estimator of the gap duration variance given the sample population. Mathematically, Eq. 4-5 shows the biased variance estimator similarity by discretizing the continuous time. When discretized, the time-averaged gap, G_{avg}, must count the gap duration in time steps, $x_{\phi_{P_j}} - x_{\phi_{P_{j-1}}}$, square the duration, and sum the total. The sum is divided by the total number of time steps, N_t.

$$G_{avg} = \frac{1}{N_t}\sum_{j=1}^{N}\left(x_{\phi_{P_j}} - x_{\phi_{P_{j-1}}}\right)^2 \tag{4-5}$$

Taking the squared difference in time steps where the point P is visible, dividing by the total number of time steps, we confirm the conjecture that G_{avg} is a sample gap duration variance estimator. It is desirable that gaps G are consistent as opposed to experiencing long and short gaps in viewing times.

Reducing the maximum gap duration, G_{max} and mean response time, average gap, G_{mrt}, tends to reduce gap duration overall, G. Minimizing G will be accomplished by scheduling and/or phasing the fixed number of satellites to provide the best coverage possible. In the case of DoP, σ, continuous coverage becomes a requirement, such that $G_{mrt} = G_{max} = G = 0$. Geometric DoP, σ, will be the driver in phasing and orbital element modification to attempt to provide at least four satellites overhead. In our use cases, network and inertial navigation systems

(INS) provide additional inputs to the target area for position estimation relaxing the four satellite constraint.

Nine constellations, C_0 to C_8, are considered in a discretized example with varying coverage. Constellations C_0 and C_1 each view the target three times. C_1 has more gaps than C_0 but each gap is only one time step. Mean response time, G_{mrt} and time averaged gap, G_{avg}, are lower for C_1 indicating consistently smaller gaps in coverage than C_0. C_0 and C_1 have the same percent coverage, C_{per}, despite C_0 having larger gap durations. Constellation C_6 has the same percent coverage as C_0 and C_1. Constellation C_6 has a larger mean response time, G_{mrt}, and time averaged gap, G_{avg}, because C_6 has only one gap that is four time steps long. Constellations C_0 and C_1 have the same gap duration overall but spread out over the simulation period in smaller consistent periods. Mean response time, G_{mrt}, and time averaged gap, G_{avg}, favor smaller consistent gaps over one large gap. Percent coverage, C_{per}, is unable to provide more information than the total gap duration in coverage over the simulation period.

Percent coverage's, C_{per}, inability to provide more information than total gap duration over the simulation period makes the metric highly sensitive to the simulation period. Assume constellations C_3 and C_5 are the same constellation. Constellation C_5 is phased two steps behind constellation C_3. During the simulation period, constellation C_5 sees the target twice doubling the percent coverage, C_{per} metric.

Maximum gap duration, G_{max}, suffers the same sensitivity to simulation period as percent coverage, C_{per}. Maximum gap duration, G_{max}, is unable to provide consistency or viewing information. Given constellations, C_0, C_1, and C_2 the maximum gap is $G_{max} = [2, 1, 2]$. Selecting constellation C_1, the minimized maximum gap, actually provides less coverage over the simulation period. Constellation C_2 provides the most coverage over the simulation period.

Table 4-3. Discretized constellation, C_i, coverage over seven time steps.

	Time Steps							Coverage Parameters			
	1	2	3	4	5	6	7	G_{mrt}	G_{avg}	C_{per}	G_{max}
C_0	y	n	n	y	n	n	y	2	1.14	42.9%	2
C_1	n	y	n	y	n	y	n	1	0.571	42.9%	1
C_2	n	y	y	y	y	n	n	1.5	0.714	57.1%	2
C_3	n	n	n	y	n	n	n	3	2.57	14.3%	3
C_4	n	y	y	n	y	y	n	1	0.429	57.1%	1
C_5	n	y	n	n	n	y	n	1.67	1.57	28.6%	3
C_6	y	n	n	n	n	y	y	4	2.29	42.9%	4
C_7	n	n	n	n	n	y	n	3	3.71	14.3%	5
C_8	y	y	y	y	y	y	y	0	0	100%	0

Mean response time, G_{mrt}, is also sensitive to the simulation period. Constellation C_7 has a lower mean response time than C_6 despite having more gaps and less viewing time. Mean response time, G_{mrt}, is an average of the gap duration. Constellation C_7's last gap is only one time step in duration before the end of the simulation period. This can artificially reduce mean response time, G_{mrt}, with additional small coverage gaps.

Time averaged gap, G_{avg}, reduces the sensitivity to the simulation period by dividing the squared gap duration by the total simulation duration. The reduction in sensitivity is demonstrated in constellations C_6 and C_7. The constellation C_6 time averaged gap, G_{avg}, is smaller than C_7. Constellation C_6 has more viewing time and less gaps than C_7.

Individual parameters are compared against several different objective functions including Eq. 4-4. Objective functions summing all figures of merit, Eq. 4-6, weighted summation of all parameters, Eq. 4-7, summation of mean response time, G_{mrt}, and time averaged gap, G_{avg}, and time averaged gap, G_{avg}.

$$f_0(G, \sigma) = G_{avg} + G_{mrt} + G_{max} + C_{per} \tag{4-6}$$

$$f_0(G,\sigma) = 0.4 \times G_{avg} + 0.4 \times G_{mrt} + 0.1 \times G_{max} + 0.1 \times C_{per} \quad (4\text{-}7)$$

In Table 4-4, the weightless objective function, Eq. 4-6, is skewed as the duration of any gap within the simulation period increases. The sensitivity to the simulation time period is reduced by not using percent coverage, C_{per}, and maximum gap duration, G_{max}, as in Eq. 4-4 and Eq. 4-5. The weighted objective function considered in Eq. 4-7 reduces the influence of these variables favoring consistent coverage by constellations.

Table 4-4. Objective function calculation demonstrating different approaches including weighting to reduce sensitivity to simulation duration.

Objective Selection							
Weighted, Eq. 4-7		Weightless, Eq. 4-6		$G_{mrt} + G_{avg}$		G_{avg}	
C_8	0.00000	C_8	0.00000	C_8	0	C_8	0
C_4	0.614286	C_4	1.857143	C_4	1.428571	C_4	0.428571
C_1	0.685714	C_1	2.142857	C_1	1.571429	C_1	0.571429
C_2	1.028571	C_2	3.642857	C_2	2.214286	C_2	0.714286
C_0	1.414286	C_0	4.714286	C_0	3.142857	C_0	1.14286
C_5	1.566667	C_5	5.952381	C_5	3.238095	C_5	1.571429
C_3	2.514286	C_3	8.428571	C_3	5.571429	C_6	2.285714
C_6	2.871429	C_6	9.857143	C_6	6.285714	C_3	2.571429
C_7	3.171429	C_7	11.57143	C_7	6.714286	C_7	3.714286

Overall, Eq. 4- 4-7, are consistent in the selection of each constellation for coverage. All objective functions selected C_8, the continuous coverage solution. Eq. 4-5, $G_{mrt} + G_{avg}$, still demonstrates a preference for consistent gap duration. The only difference in selection highlights time averaged gap's, G_{avg}'s, selection of a constellation with less gaps within the simulation time period. Constellation C_3 is valued higher than C_6 because of the consistency in gap duration.

4.3.2 Comparison of Analytical and Semi-Analytical Coverage Analyses

Using the second case study presented, 4.3.2 Continuous Coverage during FONOP, analytical and semi-analytical coverage analyses are compared. USN DDG-88 and DDG-111,

Preble and Spruance, are conducting innocent passage within 12 nautical miles of Mischief Reef in a Freedom of Navigation Operation (FONOP). Spoofing of GPS signals, (Harrison et al., 2020; Weeden & Samson, 2020) can make navigation dangerous. Continuous coverage via SAR and EO/IR imagery of Mischief Reef has been requested for a week prior to and during the FONOP. During the FONOP, satellite navigation (SATNAV) support is requested for the Ship's Inertial Navigation System (SINS) to improve piloting.

The longitude of the ascending node, argument of perigee, and true anomaly are related to the launch location by the aircraft and launch vehicle platform. The apogee, eccentricity, and inclination of the spacecraft, while directly related to the launch vehicle injection state, are achievable at any launch location. A range of feasible solutions are produced and the best solution is selected supporting aircraft and launch timing.

Table 4-5. Analytical coverage regions.

Latitude Range	Number of Coverage Regions	Percent Coverage
$\phi > \lambda_{\max} + i$	0	0
$\lambda_{\max} + i > \phi > i - \lambda_{\max}$	1	$\theta_1/180$
$i - \lambda_{\max} > \phi > 0$	2	$(\theta_1 - \theta_2)/180$

In Table 4-5 the percent coverage per orbit is estimated by comparison between the latitude of the target, ϕ, the inclination of the orbit, i, and the maximum central Earth angle, λ_{max} which is proportional to the sensor field of view for the satellite. Repeating Eq. 3-50 as Eq. 4-8, θ_1 requires a negative sign and θ_2 a positive sign to solve for the percent coverage per orbit.

$$\cos\theta_{1,2} = \frac{\pm \sin\lambda_{\max} + \cos i \sin L}{\sin i \cos L} \tag{4-8}$$

Repeating Sugrue and Crisp et al. semi-analytical coverage analysis given nodal precession for both circular and oblate spheroids. Coverage of points at a certain latitude, ϕ,

(Crisp et al., 2018; Sugrue, 2007) is predicted. Eq. 4-9 is the precession of the nodes for a circular Earth and Eq. 4-10 for an oblate spheroid using J_2.

$$\delta L = -P_k \omega_\oplus \tag{4-9}$$

$$\delta L = P_n\left(-\omega_\oplus + \delta\Omega\right) \tag{4-10}$$

where δL is the change in longitude, P_k, Keplerian period, P_n, nodal period, and $\delta\Omega$, precession of right ascension of ascending node due to the oblate spheroid perturbing harmonics like J_2.

$$P_k = 2\pi\sqrt{\frac{a^3}{\mu_\oplus}} \tag{4-11}$$

$$P_n = \frac{P_k}{\left[1 + \frac{3J_2R_{eq}}{4p}\left(\sqrt{1-e^2}(2 - 3\sin^2 i) + (4 - 5\sin^2 i)\right)\right]} \tag{4-12}$$

$$\delta\Omega = -\frac{3}{2}nJ_2\left(\frac{R_{eq}}{p}\right)^2\cos i + \frac{3}{32}nJ_2^2\left(\frac{R_{eq}}{p}\right)^4\cos i\,[12 - 4e^2 - (80 + 5e^2)\sin^2 i] \tag{4-13}$$

where $p = a(1-e^2)$, the semilatus rectum, R_{eq}, is the equatorial radius of the oblate spheroid, and $n = \sqrt{\mu_\oplus/a^3}$, the mean motion.

To determine the t_{view} over the period of analysis, we will determine all longitudinal passes at point P's latitude. Each pass, λ_{ϕ_P}, is checked for visibility by the inequality in Eq. 4-14.

$$L_{\phi_P} - L_P \leq \Lambda \tag{4-14}$$

The check on the longitudinal sensor range is used to check if point P is in the FoR if passing over longitude, L_{ϕ_P}. The longitudinal passes are determined by checking the longitudinal passes of a single satellite, L_j, multiple planes, L_p, and multiple satellites in each plane, L_s, so that combining all passes gives the constellation longitudinal passes at the given latitude over the analysis period, L_{ϕ_P}.

$$\left[L_j\right] = L_1 + (j-1)\delta L \text{ for } j = 1, 2, 3 \ldots \left|\frac{t_{simulation}}{P_n}\right| \quad (4\text{-}15)$$

$$\left[L_p\right] = \left[L_j\right] + 2\pi m\left(\frac{1}{p} + \frac{f}{t}\right) \text{ for m= 1 to } p-1 \quad (4\text{-}16)$$

$$[L_s] = \left[L_j\right] + {}^{l}/_{s}\,\delta L \text{ for } l = 1 \text{ to } s-1 \quad (4\text{-}17)$$

where a Walker constellation notation is used for separation, t, total number of satellites, p, number of equally spaced planes, f, relative spacing between satellites in adjacent planes, and s, is the number of satellites per plane. Assuming equal distribution of satellites in planes, $s = t/p$.

$$L = \text{atan}\left[\frac{\cos(\omega + \nu_\phi)\sin\Omega + \sin(\omega + \nu_\phi)\cos\Omega\cos i}{\cos(\omega + \nu_\phi)\cos\Omega - \sin(\omega + \nu_\phi)\sin\Omega\cos i}\right] + \frac{\nu_\phi}{2\pi}\delta L \quad (4\text{-}18)$$

Satellite could be ascending or descending for any pass over the target latitude so a pair of longitudes exist for the true anomaly, ν_ϕ. To compare percent coverage per orbit the t_{view} is divided by the period.

4.4 Case Studies

The constellation coverage needs to be quantified through FOMs so that constellation construction and distribution can be evaluated qualitatively. Using FreeFlyer®, a LEO orbit can be simulated to a high fidelity to compare to real orbits. Using the scripting capability of FreeFlyer®, the FOMs for constellation coverage will be added first. A uniform launch profile will be defined and added to the simulation. Optimization of orbit selection and launch location selection is added last.

Facilities assigned to the case are fixed. This reduces optimization to the scheduling problem and reaction time. Case four features only two facilities. All other cases feature three facilities. A listing of the facilities and the cases to which they are assigned is given in Table 4-6. The F-35 Lightning II variants assigned to each facility are listed. Aircraft carry one launch

vehicle. Four-ship, a group of four aircraft, is deployed from each facility. An aircraft release point is calculated using the time to achieve speed and altitude necessary for a drop.

Table 4-6. Facility names, aircraft, and case assignment.

Facility	Nickname	Case	Aircraft
USS Carl Vinson	CVN-70	1	F-35C
Eielson AFB	Eielson	1	F-35A
MCAS Iwakuni	Iwakuni	1, 2, 3, 4	F-35B
Maxwell AFB	Dannelly Field	2	F-35A
Andersen AFB	Andersen	2, 3	F-35B
Ørland Air Station	Ørland	3	F-35A
HMS Queen Elizabeth	HMS QE R08	4	F-35B

4.4.1 PLAN Shandong Carrier Strike Group (CSG) overrun by extremists

Terrorists overrun the PLAN Shandong CSG and threaten Hawaii's civilian population

with a ballistic missile strike unless their demands are met. The Shandong CSG was performing a deep-sea exercise across the international date line to demonstrate the PLAN's long-term deployment capability and range. Unfortunately, this puts the now terrorist-controlled CSG

within several hours of striking distance of Hawaii. The Carl Vinson CSG is underway near the Midway Atoll at 28°42'30"N and 177°06'58"W. The USS Carl Vinson (CVN-70) is deployed with the Navy Strike Fighter Squadron 147 (VFA-147) which operates the F-35C JSF. Additional support is requested by Indo-Pacific Command from the 356th Fighter Squadron (356th FS) and Marine Strike Fighter Squadrons 121 and 242, (VMFA-121, VMFA-242). The 356th FS operates the F-35A JSF out of Eielson AFB at 64°38′42"N and 147°05′32"W. VMFA-121 and VMFA-242 operate the F-35B out of MCAS Iwakuni at 34°08′40"N and 132°14′06"E.

Facility/Target	Latitude	Longitude	Heading	Speed (knots)
USS Carl Vinson CSG	21°42'30"	175°06'58"W	90°	50
Eielson AFB	64°38'42"	147°05'32"W	-	-
MCAS Iwakuni	34°08'40"	132°14'06"E	-	-
PLA Shandong CSG	28°42'30"	177°06'58"W	270°	50

This case represents highly constrained in time or dynamic solution. The objective is to provide persistent coverage overhead with Link 16 for terminal guidance to a net-enabled weapon to destroy the terrorist threat. This illustrates the solution of tracking a moving target, the effect of launch window on viewing time, power-constraints on the satellites, and the effect of different launching locations.

A PLAN CSG will be composed of *Jiangkai-II*-class (Type 054A) frigates, *Luyang-III*-class (Type 052D) destroyers, *Renhai*-class Type 055 destroyers, and one to two *Yuan*-class (Type 039A) or alternatively *Song*-class (Type 039) submarines in addition to support vessels.The Type 052D and 055 destroyer, DDG, is capable of deploying anti-ship cruise missiles and surface-to-air missiles (SAMs) up to 290 and 135 nmi, respectively. The Type 055 destroyer is equipped with ballistic missiles, land-attack and anti-ship, with ranges of 810 nmi, each. Assuming Shandong CSG movement at 40-50 kn, a starting location of 21°42'30"N and

175°06'58"W is provided. At top speed of 50 kn, the Shandong CSG will be within striking distance of the island of Oahu in 3 hours.

Coverage of the PLAN CSG requires persistent coverage of a moving target to provide terminal guidance to a net-enabled weapon. The coverage quality objective function is given by setting $y_0 = 0$, determining coverage of the moving target, and determining the dilution of precision over the moving target, see Eq. 4-19.

$$f_0(G,\sigma) = \left(\sqrt{tr(D)}\sigma\right) + \left(\frac{1}{N}\sum_{j=1}^{N}\left(t_{view_j} - t_{view_{j-1}}\right) + \frac{1}{t_{P_N} - t_{P_0}}\sum_{j=1}^{N}\left(t_{P_j} - t_{P_{j-1}}\right)^2\right) \quad (4\text{-}19)$$

where the optimization is the minimization of the geometric DoP, $\sigma_G = \sqrt{tr(D)}\sigma$. The minimization of the reaction time will optimize when the first satellite makes its initial pass over the PLAN CSG.

$$t_{RT} = \frac{\omega + \nu_\phi}{2\pi} P_n + \Delta t_{BO2} \quad (4\text{-}20)$$

To destroy the threat facing Hawaii's civilian populations, the Carl Vinson CSG launches Maritime Strike Tomahawks (MSTs). The USS Carl Vinson VFA-147 launches a four-ship each carrying a launch vehicle with a net-enabler satellite. The 356th FS, F-35A's, from Eielson AFB also launches a four-ship each equipped with a launch vehicle. Two F-35B's from VMFA-121 and VMFA-242 each are launched for a total of 12 satellites available for support and coverage. The constellation of 12 satellites with Link-16 terminals will provide coverage over the moving target.

Prior assumptions;

- Shandong CSG will sail in a direct heading for the island of Oahu
- Minimizing the reaction time means launching the first satellite in a direct heading

- Where η_0, initial co-azimuth, is fixed for first launch

- Phasing will occur by varying launch schedule when in same plane
  - The same effect as changing the true anomaly, ν

Time to climb was estimated as linear decreasing for the VFA-147 F-35C four-ship, 356th FS F-35A four-ship, and VMFA-121 and VMFA-242 F-35B combined four-ship. The F-35C will be launched via steam catapult, nominally estimated as 5 sec until airborne status is achieved. Climb-out, after becoming airborne, requires some distance and safety speed to clear a 500-ft obstacle at the end of the runway. Given that all aircraft are expected to reach 500 ft after the end of the runway, the climb-out speed is known and the final state, $h_{release} = 38{,}000$ ft and $M_\infty = 1.6$, is known for a linearly decreasing rate of climb, the climb time for all aircraft is the same.

Facility	Aircraft	h_{MSL} [ft]	x_{climb} [ft]	t_{climb} [sec]
USS Carl Vinson (CVN-70)	F-35C	38,000	111,390	74.386
Eielson AFB, Alaska, USA	F-35A	38,000	113,766	72.549
MCAS Iwakuni, Japan	F-35B	38,000	113,407	75.026

The F-35A should outperform the F-35C and F-35B in climb time, for weight and engine performance, respectively, given a clean surface but the same specific energy model is used to represent the available thrust for all three aircraft. The F-35C launched from the HMS Queen Elizabeth (R08) and USS Carl Vinson (CVN-70), respectively, outperforms other facilities by nearly 2,000 ft in range because of the short take-off.

The azimuth, η_0, at launch is initially assumed by using spherical trigonometry. Given Figure 3-8, where both great circles cross through the North Pole, C is the launch location, ϕ_L, L_L, B is the most current position of the Shandong CSG, ϕ_P, L_P. Angle A is the longitudinal separation between launch and target or $A = \Delta L = |L_L - L_P|$. Using the law of sines,

$\sin a/\sin A = \sin b/\sin B = \sin c/\sin C$, where $b = \pi/2 - \phi_L$, $c = \pi/2 - \phi_P$, $B = \eta_P$, and $C = 2\pi - \eta_0$, where the initial launch azimuth, η_0, and azimuth from the Shandong, η_P. If the azimuth is not known, law of cosines is used, $\cos a = \cos b \cos c + \sin b \sin c \cos A$, to find the angular separation or Earth central angle, $a = \lambda$, between B and C. Inclination of the orbit is given by using the spherical triangle formed by the arc passing through ϕ_L, L_L, and ϕ_P, L_P intersecting the equator and the right triangle formed with latitude at the launch or point. The minimum inclination is constrained to the launch latitude.

$$\sin \lambda/\sin \Delta L = \sin \pi/2 - \phi_L/\sin \eta_P = \sin \pi/2 - \phi_P/\sin 2\pi - \eta_0 \quad (4\text{-}21)$$

$$\cos \lambda = \cos \pi/2 - \phi_L \cos \pi/2 - \phi_P + \sin \pi/2 - \phi_L \sin \pi/2 - \phi_P \cos \Delta L \quad (4\text{-}22)$$

$$\cos i = \cos \phi_P \sin \eta_P \quad (4\text{-}23)$$

From each of the three facilities an inclination for an arc passing through the launch location and the initial location of the Shandong CSG is determined and presented in Table 4-7. The Shandong CSG is to the south east of Iwakuni requiring delay in launch schedule of an orbit within the constellation launched in a prograde orbit.

Table 4-7. Inclination and heading for an orbit passing directly through the facility and target.

Facility	L_L **[deg]**	ϕ_L **[deg]**	η_L **[deg]**	i **[deg]**
CVN-70	28.43°	177.23°W	345° 55′22"	116.66°
Eielson AFB	64.65°	147.09°W	16° 02′28"	92.484°
Iwakuni	34.14°	132.24°E	297° 02′12"	110.42°

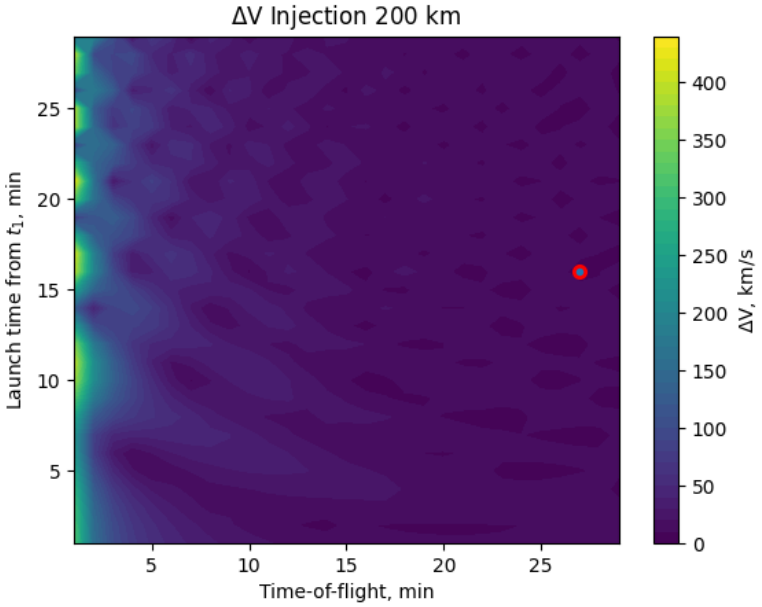

Figure 4-9. Multiple ΔV plots are created for satellite injection given the altitude of the orbit. Minimized ΔV is circled.

Assuming linear degradation over time of the inertial measurement solution for the MSTs where, $\sigma_G = at + \sigma_{G_0}$, we can determine the position and quality time over the entire simulation period. The inertial measurement solution will provide four measurements, three accelerations and a time. Four satellites overhead represent the minimum needed to solve position and time without any additional measurements.

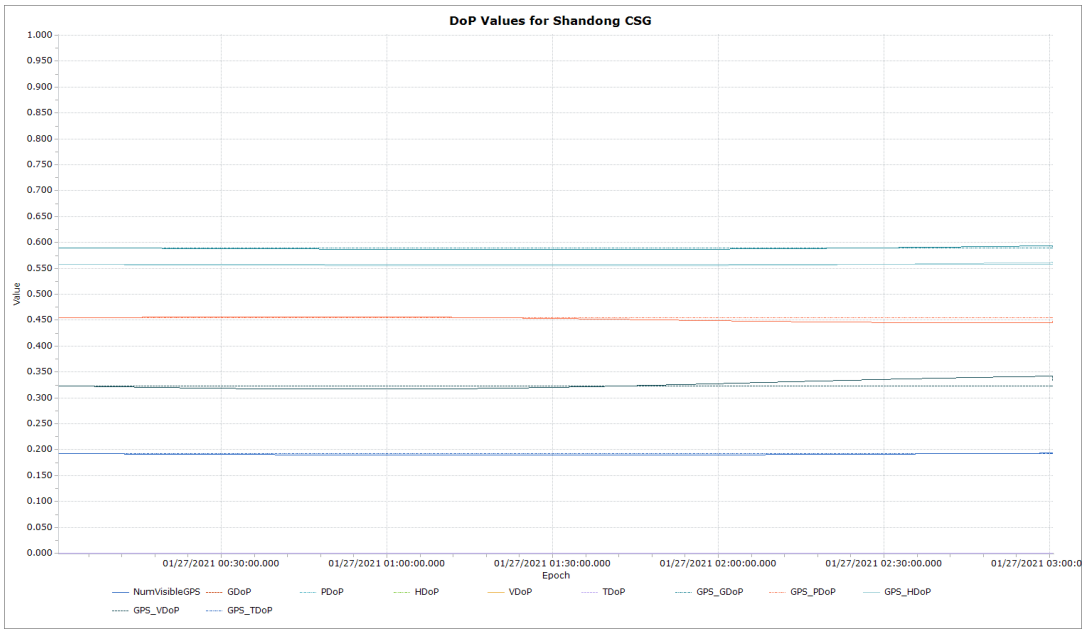

.

Figure 4-10. Dilution of Precision (DoP) over the Shandong Carrier Strike Group (CSG) shows the improvement provided to the Maritime Strike Tomahawks.

The solution optimizes the relative satellite spacing within three planes of coverage to provide continuous coverage overhead immediately following injection. The optimization of the viewing conditions starts about 375 seconds or after the satellites are injected on-orbit. Bounded linear regression is used to minimize time-of-flight by constraining each launch vehicle to 80% of the ΔV_{max}.

4.3.2 Continuous coverage during FONOP

USN DDG-88 and DDG-111, Preble and Spruance, are conducting innocent passage within 12 nautical miles of Mischief Reef in a Freedom of Navigation Operation (FONOP). Spoofing of GPS signals, (Harrison et al., 2020; Weeden & Samson, 2020) can make navigation dangerous. Continuous coverage via SAR and EO/IR imagery of Mischief Reef, $9°54'0"N$ and $115°32'0"E$, has been requested for a week prior to and during the FONOP. During the FONOP,

satellite navigation (SATNAV) support is requested for the Ship's Inertial Navigation System (SINS) to improve piloting.

This case represents the combined solution of surprise continuous coverage of a fixed point and moving vessels, rapid response, and reconstitution of jammed or disabled satellites in a constellation. ISR is provided to the moving commander in theater and navigation solutions for safety during operations. The coverage quality objective function is given by setting $y = 1, -1, 1$, determining coverage of the target, and determining the dilution of precision over the

Figure 4-11. Artificial island, Mischief Reef, build-up including SAM batteries, radar, communications, and EW capabilities ("A Look at China's SAM Shelters in the Spratlys," 2017; "Updated: China's Big Three Near Completion," 2017). SAM batteries under-construction are shown on the right.

moving target, see Eq. 4-24.

$$f_0(G,\sigma) = \left(\frac{1}{N}\sum_{j=1}^{N}\left(t_{\phi_{P_j}} - t_{\phi_{P_{j-1}}}\right) + \frac{1}{t_{\phi_{P_N}} - t_{\phi_{P_0}}}\sum_{j=1}^{N}\left(t_{\phi_{P_j}} - t_{\phi_{P_{j-1}}}\right)^2\right) - \left(\frac{1}{N}\sum_{j=1}^{N}\left(t_{view_j} - t_{view_{j-1}}\right) + \frac{1}{t_{P_N} - t_{P_0}}\sum_{j=1}^{N}\left(t_{P_j} - t_{P_{j-1}}\right)^2\right) + \left(\sqrt{tr(D)}\sigma\right) \tag{4-24}$$

$$t_{RT} = \frac{\omega + \nu_\phi}{2\pi} P_n + \Delta t_{BO2} \tag{4-25}$$

Eq. 4-24 can be reduced given that for continuous coverage, mean gap duration, G_{mrt}, and time averaged gap, G_{tag}, will be reduced to zero, $G = G_{mrt} = G_{tag} = 0$. The objective function, $f_0(G, \sigma)$, does not reduce to zero. The geometric DoP will be minimized to improve satellite navigation solutions. After solving for a constellation with continuous coverage over the requested week, prior to the FONOP, the objective function will be minimized by increasing the number of satellites with overlapping view times, t_{view}.

Facility	**Aircraft**	h_{MSL} **[ft]**	x_{climb} **[ft]**	t_{climb} **[sec]**
MCAS Iwakuni, Japan	F-35B	38,000	113,407	75.026
Maxwell AFB, Alabama, USA	F-35A	38,000	113,730	74.279
Andersen AFB, Guam	F-35A/F-35B	38,000	113,459	72.225

Coverage is optimized to place 16 satellites in 8 planes with relative spacing to provide

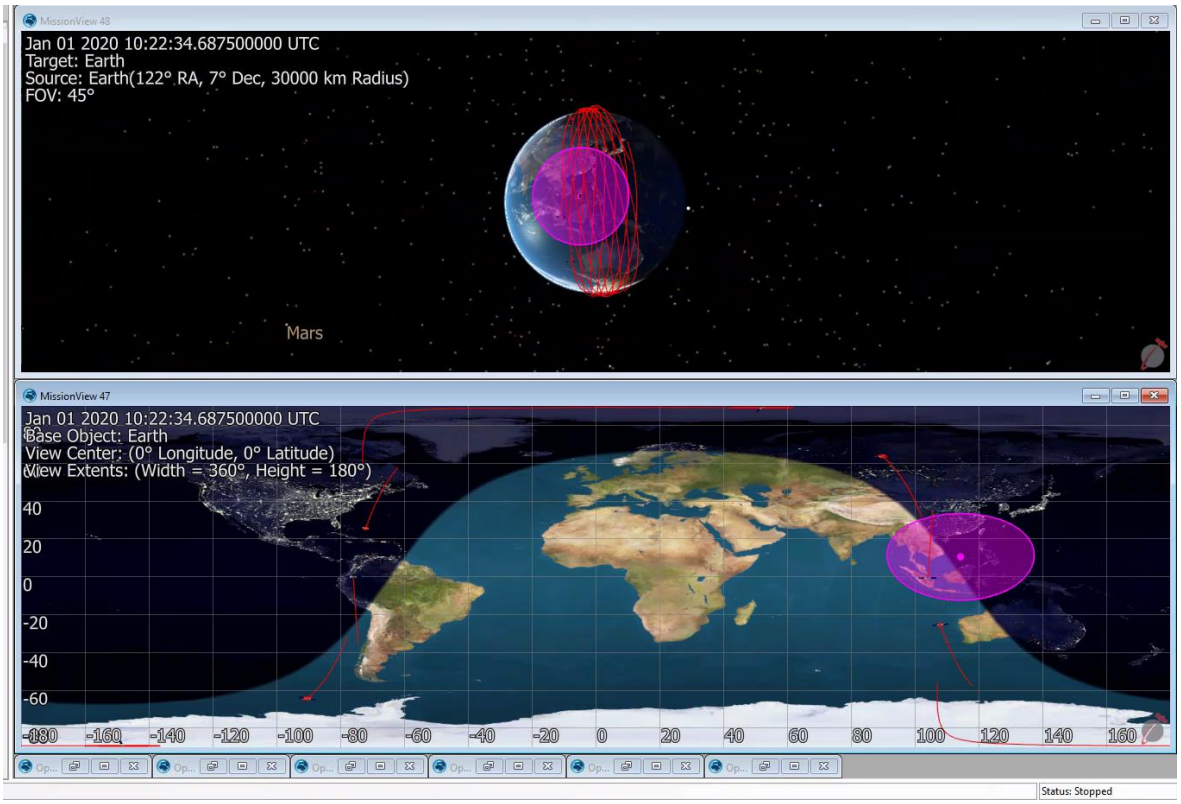

Figure 4-12. Continuous coverage the week prior to the expected Freedom of Navigation Operation (FONOP). View time is maximized during the FONOP of USS Preble and Spruance.

continuous coverage of Mischief Reef for one week. At one week, an additional 8 satellites are injected into a direct orbit from Dannelly Field to drive the PNT solution for USN DDG-88 and DDG-111. Maximum geometric DoP seen during the transit is 5.901 and the minimum seen is 1.881. None of the satellites injected de-orbit during the week-long period.

4.3.3 Humanitarian Aid/Disaster Response

Figure 4-13. USMC F-35Bs prepare to land on the flight deck of the amphibious assault ship USS Makin Island (LHD 8) (Crosley, 2020).

Typhoon Vamco made landfall 11 November 2020 ten days after super typhoon Goni made landfall along the same path in the Philippines. Search and rescue efforts were hampered by communication and electricity outages. The Makin Island Amphibious Ready Group (ARG) is directed to provide humanitarian aid and disaster relief. Surge capability for the DSCS and SA of the disaster region is provided via rapid responsive launch.

Timely comparisons of satellite mapping with SAR from Sentinel and CYGNSS or Spire, optical from Maxar, Planet, and NASA can provide critical ISR to disaster response teams. Providing SAR and optical ISR to disaster response teams on the ground in an hour will help teams make critical decisions about how to distribute support and aid, making potentially life-saving decisions for those affected.

Facility	Aircraft	h_{MSL} [ft]	x_{climb} [ft]	t_{climb} [sec]
MCAS Iwakuni, Japan	F-35B	38,000	113,407	75.026

Andersen AFB, Guam	F-35A/F-35B	38,000	113,459	72.225
Ørland Air Station, Norway	F-35A	38,000	113,717	74.933

The optimizer delivers a three plane constellation for the 12 satellites. The inclination is driven to 40.86°, 0.00°, and 32.64°. The objective function is driven to 0.00385 for the local optimized solution.

4.3.4 Rapid science return

HMS Queen Elizabeth CSG is performing a joint NATO exercise in the Norwegian Sea during July. An Arctic cyclone, projected to match the Great Arctic Cyclones 2012 and 2016, is predicted 3 days out (Doyle et al., 2019). Atmospheric forcing may cause hazardous ice, weather, and sea conditions for the exercise participants and international shipping.

An opportunity to demonstrate interagency collaboration on providing meteorological returns to the joint force and continuing science return until de-orbit. Meteorological and ISR return may require distributed communications via terrestrial and orbital systems to surface ships underway. Taking advantage of unique polar orbits will be an interesting case.

Facility	**Aircraft**	h_{MSL} **[ft]**	x_{climb} **[ft]**	t_{climb} **[sec]**
MCAS Iwakuni, Japan	F-35B	38,000	113,407	75.026
HMS Queen Elizabeth (R08)	F-35B	38,000	111,520	74.386

The objective function is driven to 0.0022 for two planes of coverage given 8 satellites launched from the four-ship from each facility. The inclination for each plane is driven to 97.2° and 83.8° with relative spacing of 0.06084.

5. CONCLUSION

In summary, a mission planning system has been delivered capable of optimizing constellation coverage given a total number of satellites launched from tactical aircraft given selected facilities. Four case studies show the capability to provide persistent coverage of a moving target to provide terminal guidance to a net-enabled weapon, coverage of a moving target, view persistence, and on-demand coverage of natural phenomena for disaster response. The three novel contributions of this work;

1. Created a mission planning system to deliver a constellation on-demand to observe a target from anywhere in the world using tactical airborne aircraft.
2. Combined existing vehicle models for aircraft, launch vehicle, satellite, and optimization tools to modify on-demand launch scheduling of a constellation for optimal coverage.
3. Applied previously existing coverage quality measurements to measure replenishment and reconstitution value added by on-demand launch.

5.1 Summary of Findings

An optimization routine for on-demand launch from tactical aircraft and a horizontal launch vehicle to deliver a constellation optimized for coverage quality from given facilities is created. Given that facilities are fixed this also fixes the number of satellites. The feasibility of the solution is dependent upon the initial number of satellites provided. Facility, aircraft, and launch vehicle models are assumed and created in a modular way. Models with improved accuracy will add to the fidelity of the solution.

This is evident in comparing the solutions for the continuous coverage solution of the Shandong Carrier Strike Group (CSG) and the Freedom of Navigation Operation (FONOP) through Mischief Reef. The continuous coverage is easily solved in the three hour simulation window for case one, Shandong CSG, but for the FONOP through Mischief Reef, even though three facilities were used for both, additional satellites were required to complete the continuous coverage solution providing PNT to the ships' navigation.

5.1.1 Optimization routine

The routine selected to optimize coverage by modifying the launch schedule of the on-demand constellation was the Bound Optimization BY Quadratic Approximation (BOBYQA) (Powell, 2009). BOBYQA is a direct search iterative algorithm and employs a quadratic approximation to the objective function. The amount of second derivative information needed is proportional to the rate of convergence. BOBYQA was selected because the derivatives of the objective function were not known. The relationship between coverage quality and launch scheduling is not immediately known. A partly numerical method measured the performance of Walker constellations using the given number of satellites. The top performing constellation was used as the initial guess for the BOBYQA method.

There are a number of advantages and disadvantages to this routine. BOBYQA will produce optimized coverage of the target. BOBYQA is in the NLopt library that FreeFlyer® is compatible with. BOBYQA does not require derivative information. BOBYQA approximates the objective function and its derivatives to the second order. The method employed is an improvement over the Constrained Optimization BY Linear Approximation which struggles to find a solution when more than nine state variables are used. Unfortunately, this solution may not be continuous coverage as requested in two of the four cases. To find some local minima that

meets this requirement the Walker constellation performance was used to guide the search. This is not ideal but it delivers the requested result.

The routine modifies the orbital parameters of each satellite in the constellation. Originally, each satellite in the constellation was modified. This created $T \times 6$ state variables where T was the number of satellites. Searching through each possible Walker constellation from the T satellites found a promising initial guess that reduced the number of state variables. Walker constellations feature the notation $T/P/F$, where T is the total number of satellites, P, is the number of planes, and F is a non-dimensional measure of satellite relative spacing, or phasing, in different orbital planes. The notation provided an easy formulaic way of relating the state variables to each satellite within the constellation. The state variables were reduced to $(P \times 3) + 1$. Each plane had its apogee, eccentricity, and inclination defined. The other variables necessary to describe the satellite state were related to the relative spacing of the satellites defined by F.

5.1.2 Vehicle models

The vehicle models support the coverage and scheduling decisions. The fidelity of the models is directly correlated in the confidence of the solution. Existing aircraft, launch vehicle, and satellite models were combined and used. The development of additional models was beyond the scope of the work.

To provide a solution with exceeding confidence selection of an aircraft like the F-35 Lightening II requires detailed performance information. Using lower fidelity models the mission planner can still make confident choices in selection of squadrons and facilities. These models are not easy to change in the current format and layout of the mission planning program. FreeFlyer® is resource intensive so models were directly developed in Python and relations for scheduling were determined in Python based on orbital coverage solutions provided by

FreeFlyer. Changing the aircraft model from the F-35 Lightening II model would require additional code development.

The launch vehicle model uses a Lambert targeting solution and checks against the performance required. In order to use the F-35 Lightening II, some restriction had to be made on the size of the vehicle, which will restrict the performance. First-order approximations and using existing missile outer mold lines suggest a two-stage launch vehicle employing a hybrid-hybrid or solid-hybrid combination. To restrict the scope and stop trying to solve a missile design problem a check was made against the energy or velocity change required, ΔV, for the Lambert solution and a selected hybrid-hybrid two-stage launch vehicle performance. Each motor's performance was estimated given sizing assumptions. The first-order assumptions necessary to develop the model should lower the confidence in the timing of the Lambert trajectory until additional fidelity is added to the launch vehicle by solving the design problem or providing known performance.

The satellite model uses nanosatellite sizing. The mass and dimensions of the model affect the lifetime and slew rates of the spacecraft. Multiple standard buses exist for the nanosatellite level. FreeFlyer® offers multiple tools that can be developed to aid in modules or black-box feedback to the objective function on coverage quality each satellite can provide for its individual payload. To prevent payload design considerations in each of the four cases, a standard model for coverage quality based on pass timing was used. Again, modification of the objective function, coverage quality measurement, would require additional scripting on the part of the user. The current approach still provides a high fidelity solution especially as each constellation is launched to cover a single region or target. This differs from most, if not all,

current focus on constellations on-orbit providing on-demand coverage of new multiple targets and the resulting performance.

5.1.3 Output performance

Running FreeFlyer® in its GUI mode is resource intensive and undesirable as a final solution for optimizing each case. This was necessary unfortunately to adequately debug problems arising with orbit propagation or optimization results. Modification of visual output from FreeFlyer® requires a large amount of scripting.

Satellite and aircraft models were easy to produce, script, and integrate. The launch vehicle model required additional time to develop because of the initial wide scope employed in development. The satellite and aircraft models were both produced on-time while the launch vehicle model required several additional weeks of work beyond what was originally scheduled.

No derivative information for the relationship between coverage quality and orbital parameters required use of a non-derivative method. Desire for a local solution minima allowed selection of BOBYQA for its performance given other methods tried in NLopt. BOBYQA is a direct search method that gradually reduces the interval for the state variables that it modifies to find the solution. Providing an initial guess close to the local minima was important for convergence. The lack of resources to support a full state-space search in a validation problem for BOBYQA leaves doubts as to the whether there is a more appropriate selection.

5.2 Future Work

The mission planning system will be improved in three targeted areas. A Graphic User Interface (GUI) will be added to aid users in selection of targets and optimization of coverage using existing satellite resources. The software is modular so vehicle models replacement should be

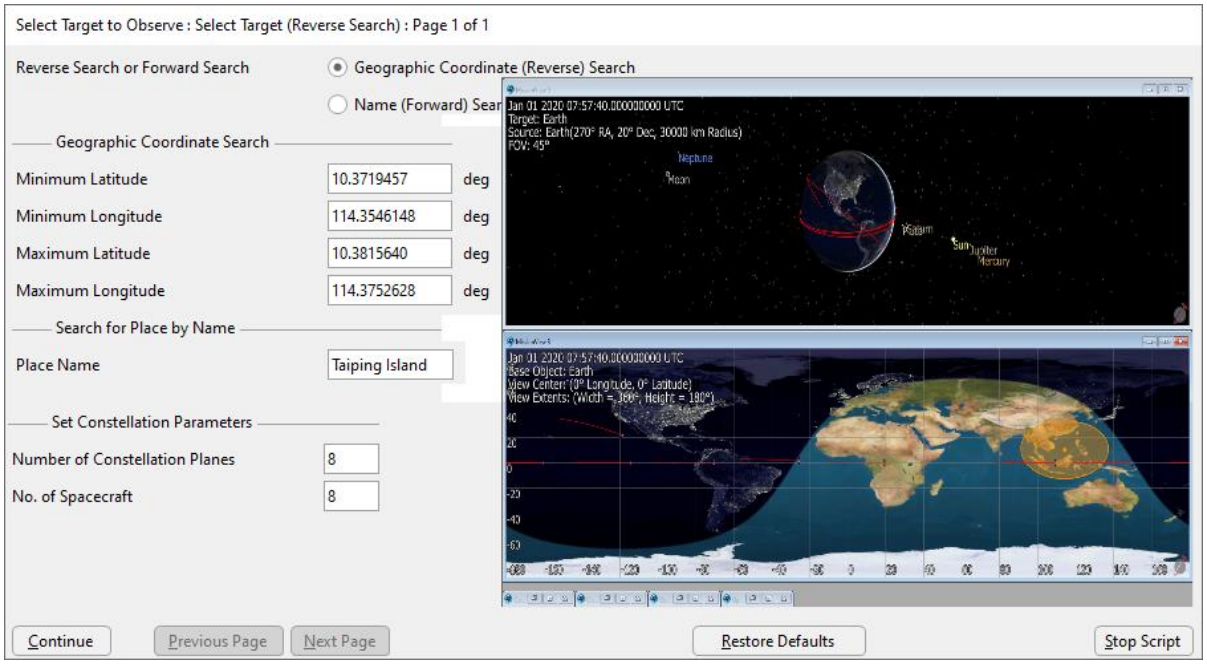

Figure 5-1. Conceptual GUI for the mission planning system with improved targeting selection and solution visualization.

streamlined for the mission planner. Additional validation of optimization algorithms and providing additional local solutions besides the local minima to the mission planner will provide confidence in the solution and options to the mission planner.

5.2.1 Graphical user interface

The GUI should improve the mission planner's ability to select targets and construct a meaningful solution with existing resources. Figure 5-1 demonstrates a conceptual GUI including analytical ephemerides providing initial solution estimates to the mission planner. The GUI provides the coverage optimization solution including orbital and ground track views, coverage quality metrics, and additional possible local solutions to the mission planner.

FreeFlyer ® visual modeling is wrapped and provided to the user internally. The user should be able to select different windows to examine the optimization process enabling trust in the process. The user should not have to modify the background supporting code to maintain focus on the mission planning aspect.

5.2.2 Model replacement

Modular development of the code was accomplished. Replacing modules will require additional scripting in Python. Additional scripting is undesirable for the user because this takes away from the mission planning objective to build additional modules. If the user wishes to provide their own vehicle model the user should be able to integrate the model with minimal effort. Integration of additional models should be accomplished by selection of options within a GUI interface. Technical users should be able to replace or add the model to the script and should be provided an interface control document to support future integration. The desirable outcome is plug-and-play with different models to account for more realistic behavior or empirical data.

5.2.3 Optimization algorithm

Providing a local solution to FreeFlyer® optimizer engine while recognized as a feasible solution is not recorded as the best solution. A simple work-around was devised to record a local solution if provided as the initial guess to the optimizer. Future work should use FreeFlyer® API to run the objective function, coverage quality measurements, while optimizing with the Nlopt or Ipopt libraries in the code outside of FreeFlyer®. Additional validation by sampling the entire state space needs to be provided in future work.

5.2.4 Path forward

State space sampling of each of the four cases presented should be completed. This will identify why a Walker constellation sampling was necessary and what could be done to improve the initial guess of the BOBYQA algorithm. Additionally, performance comparisons between the FreeFlyer® optimization interface and using optimization in script while FreeFlyer® returns the objective function value should be compared.

The next step should be to improve interface control documentation for each module. The interface control documentation will allow for easy replacement and integration of future vehicle and optimization models. The documentation will further inform future programming efforts to improve the mission planning system.

After these steps, then a GUI can be constructed to make the mission planning system user-friendly for the mission planner. A wrapper should be written to encapsulate the final product.

5.3 Additional Applications

This work can be used to support future efforts in modeling on-demand launch from airborne platforms for rapid constellation installation, on-demand launch of vertical lift launch vehicles, constellation coverage quality assessments, airborne launch platform models, reconstitution of existing constellations, and servicing satellites launched on-demand. Scheduling on-demand launch for constellation installation is the major focus of this dissertation.

Provided with the code and FreeFlyer ® scripts a user could model coverage optimization of a selected target using on-demand launch. The software modular construction means that users could use the aircraft, launch vehicle, or satellite scripts to model each vehicle individually for new uses. For example, the launch vehicle script needs no modification to model

vertical lift launch from a fixed launch site. Users could add a fixed launch site into consideration with the airborne platforms for some unique solution where typical fixed launch site scheduling is not an issue.

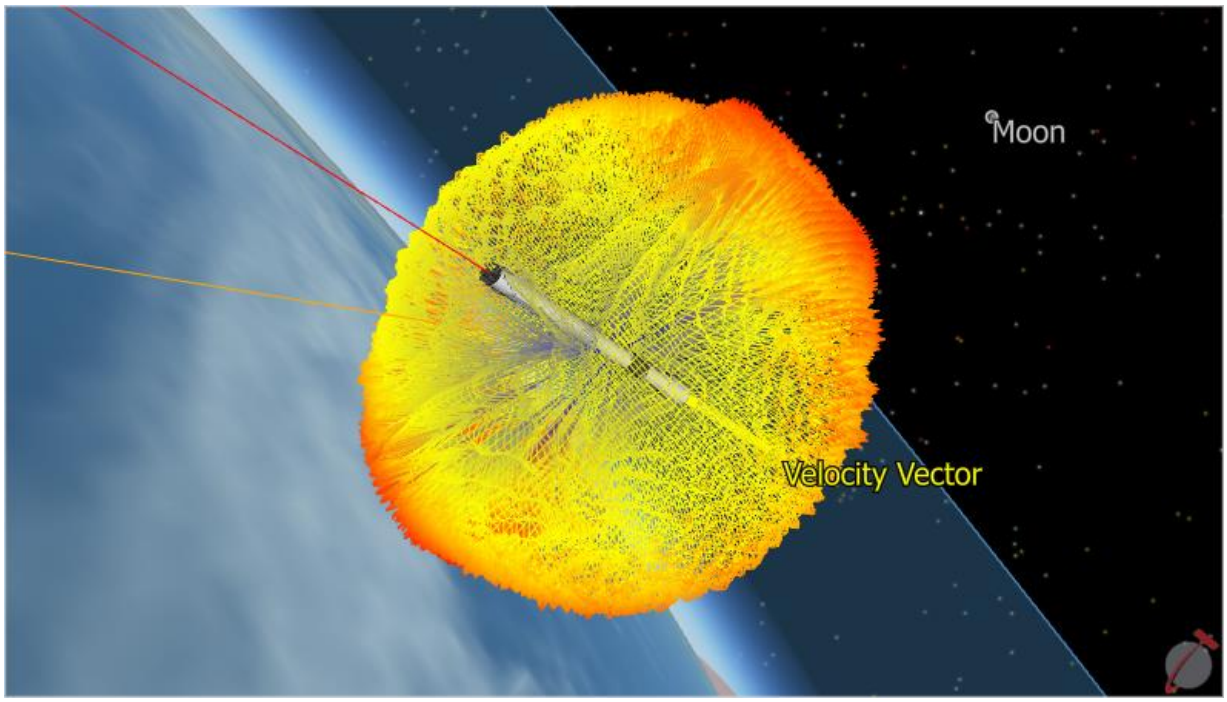

Figure 5-2. Launch vehicle flight visualized in FreeFlyer ®.

The coverage quality and lifetime assessments of the satellites need no modification for a given target to provide an estimate of coverage quality and a deterministic estimate of satellite orbital lifetime. These could be used by future users to evaluate constellations outside of launch considerations by simply providing orbital parameters.

Interested commercial users could take advantage of the modularity of the software to provide a coverage assessment of an existing constellation and add considerations for degradation to justify satellite servicing or reconstitution costs. On-demand launch and fixed launch site scheduling could be evaluated based on the cost in coverage and loss of revenue. Government users could evaluate the cost based on ISR metrics and current sensor tasking in-theater.

5.4 Restatement of Findings

In summary, a mission planning system to optimize delivery of multiple satellites from multiple similar air-launched platforms for constellation installation meeting a specified minimum duration has been delivered. Four case studies show the capability to provide persistent coverage of a moving target to provide terminal guidance to a net-enabled weapon, provide reconstitution of a PNT constellation, view persistence, and on-demand coverage of natural phenomena for disaster response. The three novel contributions of this work;

1. Created a mission planning system to deliver a constellation on-demand to observe a target from anywhere in the world using tactical airborne aircraft.
2. Combined existing vehicle models for aircraft, launch vehicle, satellite, and optimization tools to modify on-demand launch scheduling of a constellation for optimal coverage.
3. Applied previously existing coverage quality measurements to measure replenishment and reconstitution value added by on-demand launch.

REFERENCES

6U SUPERNOVATM Structure Kit: Owner's Manual. (2014). Retrieved from 750 Naples Street, San Francisco, CA 94112: http://www.cubesatkit.com/docs/SUPERNOVA_User_Manual-RevA0.pdf

19.3 Small Business Innovation Research (SBIR) Direct to Phase II Proposal Submission Instructions. (2019). UNITED STATES SPECIAL OPERATIONS COMMAND Retrieved from https://www.socom.mil/SOF-ATL/SBIR%20193/USSOCOM-19.3_DPhII%20v2.pdf.

AAC Clyde Space. (2019). In A. C. Space (Ed.), (1st ed., pp. 22). online: AAC Clyde Space.

Abba, A. M., Meselhy, K. T., Moughith, W. S., & Omer, A. A. (2019). *Agile mission optimization for a constellation of earth observation satellites*. Paper presented at the 18th International Conference on Aerospace Sciences & Aviation Technology.

Acton, C., Bachman, N., Thomson, F., Semenov, B., & Wright, E. (2020). *Fundamental Concepts*. Retrieved from Pasadena, CA: https://naif.jpl.nasa.gov/pub/naif/toolkit_docs/Tutorials/pdf/individual_docs/04_concepts.pdf

Acuna, J. A., Zayas-Castro, J. L., & Charkhgard, H. (2019). Ambulance allocation optimization model for the overcrowding problem in US emergency departments: A case study in Florida. *Socio-Economic Planning Sciences*, 12. doi:10.1016/j.seps.2019.100747

Administration, N. A. a. S. (2020). *NASA Spacecraft Conjunction Assessment and Collision Avoidance Best Practices Handbook* (NASA/SP-20205011318). Retrieved from online: https://nodis3.gsfc.nasa.gov/OCE_docs/OCE_50.pdf

Air Launched Sounding Rocket (ALSOR) Attached to F-104. (1959). In 306458main_E-5071_full (Ed.), (pp. JF-104A (Serial #156-0749) on the ramp at the NASA Flight Research Center (now the Dryden Flight Research Center) at Edwards AFB. The aircraft is shown with the Air Launched Sounding Rocket (ALSOR) attached to the underside. NASA test pilot Milton O. Thompson ejected from this aircraft on 0720 December 1962, after an asymmetrical flap condition made the jet uncontrollable.). Edwards, CA: National Aeronautics and Space Administration.

Allison, L. C. M.-L. (2020). From space traffic monitoring to human space flight rescue, Vandenberg units provide integral support to NASA missions [Press release]. Retrieved from https://www.spacecom.mil/News/Article-Display/Article/2447906/from-space-traffic-monitoring-to-human-space-flight-rescue-vandenberg-units-pro/

Almaz-Antey. (2015). Противоракеты. In 1137442 (Ed.). online.

Altman, D., Baker, D., Bissell, W., Boden, D. G., Erickson, J. W., Forward, R., . . . Witter, J. K. (1995). *Space Propulsion Analysis and Design* (R. W. Humble, G. N. Henry, & W. J. Larson Eds. 1st Edition - Revised ed.): McGraw-Hill Companies, Inc.

Anz-Meador, P. (2015, Jul 2015). A Review of Space Environment Implications of CubeSat Traffic, 2003-2014. *Orbital Debris Quarterly News, 19,* 10.Armstrong, S. S. J. T. (2019). USSPACECOM expands key allied space partnerships through multination operations [Press release]. Retrieved from https://www.spacecom.mil/MEDIA/NEWS-ARTICLES/Article/2047780/usspacecom-expands-key-allied-space-partnerships-through-multi-nation-operations/

Baek, S.-w., Han, S.-m., Cho, K.-r., Lee, D.-w., Yang, J.-s., Bainum, P. M., & Kim, H.-d. (2011). Development of a scheduling algorithm and GUI for autonomoussatellite missions. *Acta Astronautica, 68*(7), 1396-1402. doi:10.1016/j.actaastro.2010.08.011

Ballard, A. H. (1980). Rosette Constellations of Earth Satellites. *IEEE Transactions on Aerospace and Electronic Systems*, *AES-16*(5), 18. doi:10.1109/TAES.1980.308932

Barrett, B. (2020). *Arctic Strategy*. Department of Defense.

Bartolotta, P. A., Buchen, E., Engelund, W. C., Huebner, L. D., Moses, P. L., Schaffer, M., . . . Wilhite, A. W. (2011). *Horizontal Launch: A Versatile Concept for Assured Space Access* (NASA SP 2011-215994). Retrieved from United States: https://ntrs.nasa.gov/archive/nasa/casi.ntrs.nasa.gov/20120000791.pdf

Bate, R. R., Mueller, D. D., & White, J. E. (1971). *Fundamentals of Astrodynamics* (1st ed.). USA: Dover Publications.

Battin, R. H. (1999). *An Introduction to the Mathematics and Methods of Astrodynamics* (Revised ed.). Reston, Virginia: American Institute of Aeronautics and Astronautics.

Becker, C., & Merrill, G. (2017a). *Mesh Network Architecture for Enabling Inter-Spacecraft Communication*. Paper presented at the 31st AIAA & Utah State University Conference on Small Satellites, Logan, UT. https://ntrs.nasa.gov/search.jsp?R=20170009051&hterms=Garrick+Merrill&qs=N%3D0%26Ntk%3DAll%26Ntt%3DGarrick%2520Merrill%26Ntx%3Dmode%2520matchallpart

ial%26Nm%3D123%7CCollection%7CNASA%2520STI%7C%7C17%7CCollection%7CNACA

Becker, C., & Merrill, G. (2017b, 5 Aug 2017). *Mesh Network Architecture for Enabling Inter-Spacecraft Communication.* Paper presented at the 31st AIAA & Utah State University Conference on Small Satellites, Logan, UT.

Bensana, E., LeMaitre, M., & Verfaillie, G. (1999). Earth Observation Satellite Management. *Constraints, 4*(3), 293-299. doi:10.1023/A:1026488509554

Berger, J. M., Moles, J. B., & Wilsey, D. G. (1992). *An Analysis of USSPACECOM's Space Surveillance Network Sensor Taskipg Methodology*. (Master of Science in Space Operations), Air Force Institute of Technology Air University, (AFIT/GSO/ENS/92D-02)

Bille, M., & Lishock, E. (1998). *Future Military Applications of Small Satellites*. Paper presented at the AIAA Defense and Civil Space Programs Conference and Exhibit, Huntsville, AL.

Bille, M., & Lishock, E. (2002). *NOTSNIK: The Secret Satellite*. Paper presented at the 40th AIAA Aerospace Sciences Meeting & Exhibit, Reno, NV. https://arc.aiaa.org/doi/pdf/10.2514/6.2002-314

Bojorquez, O. J., Dolan, N., & Chen, J. (2020). *Aircraft Rerouting under Risk Tolerance during Space Launches*. Paper presented at the AIAA Scitech 2020 Forum, Orlando, FL. https://arc.aiaa.org/doi/10.2514/6.2020-1589

Boll, N. J. (2016). *Small satellites: Applications in resiliency and redundancy*. Paper presented at the AIAA Space 2016, Long Beach, CA.

Bonin, G., Roth, N., Armitage, S., Newman, J., Risi, B., & Zee, R. E. (2015). *CanX–4 and CanX–5 Precision Formation Flight: Mission Accomplished!* Paper presented at the 29th Annual AIAA/USU Conference on Small Satellites, Logan, UT. https://digitalcommons.usu.edu/smallsat/2015/all2015/3/

Busse, F. D. (2003). *Precise Formation-State Estimation in Low Earth Orbit Using Carrier Differential GPS.* (Doctor of Philosophy), Stanford University, Pasedena, California.

C4ISR for Future Naval Strike Groups. (2006). Retrieved from Washington, DC: https://www.nap.edu/catalog/11605/c4isr-for-future-naval-strike-groups

Cacioni, A. (2018). *Risk of Collision: an Operator Perspective*. Paper presented at the 2018 SpaceOps Conference, Marseille, France. https://arc.aiaa.org/doi/pdf/10.2514/6.2018-2667

Canin, D. G., McConnell, J. K., & James, P. W. (2019). *F-35 High Angle of Attack Flight Control Development and Flight Test Results*. Paper presented at the AIAA Aviation 2019 Forum, Dallas, Texas, U.S.A.

Cantwell, B. J. (2020). *Chapter 11 Hybrid Rockets*. AA283 Aircraft and Rocket Propulsion. course notes. Department of Aeronautics and Astronautics. Stanford University. online.

Carter, J. (2016, 01 Sep 2016). *Air Launch - Low-Cost Small Satellite Launch at NASA Armstrong Flight Research Center.* Paper presented at the AIAA Space 2016, Long Beach, CA.

Cates, G. R., Houston, D. X., Conley, D. G., & Jones, K. L. (2018). *Launch Uncertainty: Implications for Large Constellations*. Retrieved from https://aerospace.org/sites/default/files/2018-12/Cates-Houston-Conley_LaunchUncertainty_12032018_0.pdf

Chahat, N., Hodges, R. E., Sauder, J., Thomson, M., Peral, E., & Rahmat-Samii, Y. (2016). CubeSat Deployable Ka-Band Mesh Reflector Antenna Development for Earth Science Missions. *IEEE Transactions on Antennas and Propagation, 64*(6). doi:10.1109/TAP.2016.2546306

Chan, F. K. (2008). *Spacecraft Collision Probability*. El Segundo, CA; Reston, VA: The Aerospace Press; American Institute of Aeronautics and Astronautics.

Chandrasekaran, A., Stewart, K., & Murphy, G. (2004). *Telemetry, Tracking, and Ground Station Architectures for Small Satellite Clusters*. Paper presented at the 42nd AIAA Aerospace Sciences Meeting and Exhibit, Reno, NV.

Chen, H., Chen, G., Shen, D., Blasch, E. P., & Pham, K. (2010). Orbital Evasive Target Tracking and Sensor Management. In M. J. Hirsch, P. M. Pardalos, & R. Murphey (Eds.), *Dynamics of Information Systems: Theory and Applications* (pp. 233-255). New York, NY: Springer.

Cheng, D., Lt. Col. Garretson, P. U., Goswami, N., Lewis, J., MacDonald, B. W., Suzuki, K., . . . Wright, N. (2018). *Outer Space; Earthly Escalation? Chinese Perspectives on Space Operations and Escalation*. Retrieved from https://apps.dtic.mil/dtic/tr/fulltext/u2/1066706.pdf

Chew, C. C., Reager, J. T., & Small, E. E. (2018). CYGNSS data map flood inundation during the 2017 Atlantic hurricane season. *Nature: Scientific Reports, 8*(9336), 8. doi:10.1038/s41598-018-27673-x

Chew, C. C., & Small, E. E. (2017). Soil Moisture Sensing Using Spaceborne GNSS Reflections: Comparison of CYGNSS Reflectivity to SMAP Soil Moisture. *Geophysical Research Letters, 45*, 9. doi:10.1029/2018GL077905

Chiles, M. C. (2020). 18 SPCS now predicts debris-on-debris collisions in space, enhancing Space Domain Awareness for all [Press release]. Retrieved from https://www.spacecom.mil/News/Article-Display/Article/2360595/18-spcs-now-predicts-debris-on-debris-collisions-in-space-enhancing-space-domai/

Chini, P., Giambene, G., & Kota, S. (2009). A survey on mobile satellite systems. *INTERNATIONAL JOURNAL OF SATELLITE COMMUNICATIONS, 28*, 29-57. doi:10.1002/sat.941

Cho, D.-H., Kim, J.-H., Choi, H.-L., & Ahn, J. (2018). Optimization-Based Scheduling Method for Agile Earth-Observing Satellite Constellation. *Journal of Aerospace Information Systems, 15*(11), 14.

Chobotov, V. A., Herman, D. E., & Johnson, C. G. (1997). Collision and Debris Hazard Assessment for a Low-Earth-Orbit Space Constellation. *Journal of Spacecraft and Rockets, 34*(2), 6. doi:10.2514/2.3198

Chobotov, V. A., Karrenberg, H. K., Chao, C.-C. G., Miyamoto, J. Y., Lang, T. J., & Kechichian, J. A. (2002). *Orbital Mechanics* (V. A. Chobotov Ed. 3rd ed.). Reston, Virginia: American Institute of Aeronautics and Astronautics.

Chung, S.-J., Bandyopadhyay, S., Foust, R., Subramanian, G. P., & Hadaegh, F. Y. (2016). Review of Formation Flying and Constellation Missions Using Nanosatellites. *Journal of Spacecraft and Rockets, 53*(3), 12. doi:10.2514/1.A33291

Clark, S. (2019). Rockets purchased by Stratolaunch back under Northrop Grumman control. *Spaceflight Now*, 8. Retrieved from Spaceflight Now website: https://spaceflightnow.com/2019/10/10/rockets-purchased-by-stratolaunch-back-under-northrop-grumman-control/

Cole, S. (2020). NASA Responds to Puerto Rico Quakes. Retrieved from https://blogs.nasa.gov/disaster-response/2020/01/17/nasa-responds-to-puerto-rico-quakes/

Collins, M. (1969). Apollo 11 Lunar Module ascent stage photographed from Command Module. In AS11-44-6642 (Ed.), (Vol. 3000 x 2896, pp. AS11-44-6642 (6621 July 1969) --- The Apollo 6611 Lunar Module ascent stage, with astronauts Neil A. Armstrong and Edwin E. Aldrin Jr. aboard, is photographed from the Command and Service Modules (CSM) during rendezvous in lunar orbit. The Lunar Module (LM) was making its docking approach to the CSM. Astronaut Michael Collins remained with the CSM in lunar orbit while the other two crewmen explored the lunar surface. The large, dark-colored area in the background is Smyth's Sea, centered at 6685 degrees east longitude and 6642 degrees south latitude on the lunar surface (nearside). This view looks west. The Earth rises above the lunar horizon.). Houston, TX: National Aeronautics and Space Administration - Johnson Space Center.

Come, H., Stefanov, L., Munoz, I., Chellathurai, R., Benoist, J., Medina, T., . . . Melloni, S. (2016). *GALILEO 5 and 6 LEOP or How to Handle and Recover Two of the Most Feared Failures Occurring Simultaneously*. Paper presented at the SpaceOps 2016 Conference, Daejeon, Korea.

Crisp, N. H., Livadiotti, S., & Roberts, P. C. E. (2018). A Semi-Analytical Method for Calculating Revisit Time for Satellite Constellations with Discontinuous Coverage. *Computing Research Repository (CoRR), abs/1807.02021*, 10.

Crosley, P. (2020). USS Makin Island ARG/15th MEU arrives off Somali Coast. In uss_makin_island_arg15th_meu_arrives_off_somali_coast (Ed.), (pp. 201218-M-UY201835-201052 INDIAN OCEAN (Dec. 201218, 202020) – U.S. Marine Corps F-201235B Lightning IIs with Marine Medium Tiltrotor Squadron 201164 (Reinforced), 201215th Marine Expeditionary Unit prepare to land on the flight deck of the amphibious assault ship USS Makin Island (LHD 201218). The F-201235Bs provide close air support to Operation OCTAVE QUARTZ. The mission of OOQ is to reposition U.S. DOD forces in Somalia to other East Africa operating locations while maintaining pressure on violent extremists and supporting partner forces.). online: United States Africa Command.

DARPA Launch Challenge. (2019). Retrieved from https://www.darpalaunchchallenge.org/

Day, D. (2010, 11 Jan 2010). Smashing RORSATs: the origin of the F-15 ASAT program. *The Space Review: essays and commentary about the final frontier*, 8.

de Selding, P. B. (2015). 1 in 5 Cubesats Violates International Orbit Disposal Guidelines. *SpaceNews*, 4. Retrieved from SpaceNews website: https://spacenews.com/1-in-5-cubesats-violate-international-orbit-disposal-guidelines/

Defense, D. o. (1993). Graphical Comparison of U.S. Standard Atmopsheres and Military Standard Climatic Extremes. In (Vol. MIL-STD-210A). Wright- Patterson Air Force Base OH 45433- 7126: United States Air Force.

Defense, D. o. (2007). GLOBAL POSITIONING SYSTEM PRECISE POSITIONING SERVICE PERFORMANCE STANDARD. In (pp. 156). online.

Defense, D. o. (2020). GLOBAL POSITIONING SYSTEM STANDARD POSITIONING SERVICE PERFORMANCE STANDARD. In *GPS Space Segment (SS)* (pp. 196). online.

Dell'Elce, L., Arnst, M., & Kerschen, G. (2015). Probabilistic Assessment of the Lifetime of Low-Earth-Orbit Spacecraft: Uncertainty Characterization. *Journal of Guidance, Control, and Dynamics, 38*(5), 13. doi:10.2514/1.G000148

DePasquale, D., Charania, A. C., Matsuda, S., & Kanayama, H. (2010). *NanoLauncher: An Affordable and Dedicated Air-Launch Transportation Service for Nanosatellites*. Paper presented at the AIAA Space 2010 Conference & Exposition, Anaheim, CA. https://arc.aiaa.org/doi/pdf/10.2514/6.2010-8629

Describing Orbits. (2017). Retrieved from online: https://www.faa.gov/about/office_org/headquarters_offices/avs/offices/aam/cami/library/online_libraries/aerospace_medicine/tutorial/media/III.4.1.4_Describing_Orbits.pdf

Devaraj, K., Kingsbury, R., Ligon, M., Breu, J., Vittaldev, V., Klofas, B., . . . Colton, K. (2017). *Dove High Speed Downlink System*. Paper presented at the 31st Annual AIAA/USU Conference on Small Satellites, Logan, UT.

Di Mauro, G., Lawn, M., & Bevilacqua, R. (2018). Survey on Guidance Navigation and Control Requirements for Spacecraft Formation-Flying Missions. *Journal of Guidance, Control, and Dynamics, 41*(3), 21.

Diaz, J. E. E. (2017). *AN AUTONOMOUS AND DYNAMICAL APPROACH TO SMALL SATELLITE GROUND STATIONS NETWORKS.* (Ph.D. Doctorate Thesis), Instituto Nacional de Pesquisas Espaciais (INPE), São José dos Campos. (CDU 004.8:629.783)

Doyle, J. D., Fearon, M. G., Finocchio, P., & Amerault, C. M. (2019). *Sensitivity and Predictability Drivers of Arctic Cyclones*. Paper presented at the 15th Conference on Polar Meteorology and Oceanography, Boulder, CO. https://ams.confex.com/ams/15Polar/meetingapp.cgi/Paper/357652

Erwin, S. (2020). SpaceX rideshare program putting downward pressure on prices. *SpaceNews*. Retrieved from SpaceNews.com website: https://spacenews.com/spacex-rideshare-program-putting-downward-pressure-on-prices/

Escobosa, J. (2017). F-35C Lightning II aircraft are tested aboard USS Abraham Lincoln. In 170904-N-CT127-0252 (Ed.), (Vol. 4185x2790, pp. ATLANTIC OCEAN (Sept. 4, 2017) An F-2035C Lightning II assigned to the Grim Reapers of Strike Fighter Squadron (VFA 2101) launches off the flight deck of the Nimitz-class aircraft carrier USS Abraham Lincoln (CVN 2072). Abraham Lincoln is underway conducting training after successful completion of carrier incremental availability. (U.S. Navy photo by Mass Communication Specialist 2011st Class Josue Escobosa/Released) 170904-N-CT170127-170252). flickr: US Navy.

Etherington, D. (2020). Rocket Lab points out that not all rideshare rocket launches are created equal. *Tech Crunch*. Retrieved from Tech Crunch website: https://techcrunch.com/2020/01/30/rocket-lab-points-out-that-not-all-rideshare-rocket-launches-are-created-equal/

Fang, B. T. (1979). Satellite-to-Satellite Tracking Orbit Determination. *Journal of Guidance and Control, 2*(1), 7. doi:10.2514/3.55832

Fasano, G., & D'Errico, M. (2006). *Design of Formation Missions for Earth Observation: Relative Motion Model, Validation, and Application*. Paper presented at the 57th International Astronautical Congress (IAC), Valencia, Spain. https://arc.aiaa.org/doi/pdf/10.2514/6.IAC-06-C1.P.8.01

Forbis, M. (2018). *The Space Fight: An Examination of the Space Warfighting Domain and What It Takes to Win!* Retrieved from https://apps.dtic.mil/dtic/tr/fulltext/u2/1075284.pdf

Foust, J. (2014). Air launch, big and small. *The Space Review: essays and commentary about the final frontier*. Retrieved from The Space Review website: https://www.thespacereview.com/article/2543/1

. FreeFlyer (Version 7.5). (2019). Lanham, MD: a.i. solutions, Inc.

Fry, A., Cook, R., & Revill, N. (2009). CVF ski-jump ramp profile optimisation for F-35B. *THE AERONAUTICAL JOURNAL, 113*(1140), 7. doi:10.1017/S0001924000002803

Gao, S., Rahmat-Samii, Y., Hodges, R. E., & Yang, X.-X. (2018). Advanced Antennas for Small Satellites. *Proceedings of the IEEE, 106*(3), 12. doi:10.1109/JPROC.2018.2804664

Garwin, R. L., & Pike, J. (1984). History and current debate. *Bulletin of the Atomic Scientists, 40*(5), 9.

Gist, R. G., & Oltrogge, D. L. (1999). *COLLISION VISION: COVARIANCE MODELING AND INTERSECTION DETECTION FOR SPACECRAFT SITUATIONAL AWARENESS*. Paper presented at the AAS/AIAA Astrodynamics Specialist Conference, Girdwood, AK. https://www.researchgate.net/profile/Daniel_Oltrogge/publication/304674606_COLLISION_VISION_COVARIANCE_MODELING_AND_INTERSECTION_DETECTION_FOR_SPACECRAFT_SITUATIONAL_AWARENESS/links/5776a59a08ae1b18a7e1af14/COLLISION-VISION-COVARIANCE-MODELING-AND-INTERSECTION-DETECTION-FOR-SPACECRAFT-SITUATIONAL-AWARENESS.pdf

Gogineni, P., Simpson, C. R., Yan, J.-B., O'Neill, C., Sood, R., Gurbuz, S. Z., & Gurbuz, A. C. (2018). *A CubeSat Train for Radar Sounding and Imaging of Antarctic Ice Sheet*. Paper presented at the International Geoscience and Remote Sensing Symposium (IGARSS 2018), Valencia, Spain.

GOMSpace 6U Platform. (2020). Retrieved from https://gomspace.com/6u-platform.aspx

Goodloe, C., Johnson, M., Kepko, L., Clagett, C., Santos, L., & Johnson, T. (2017). *CubeSat Buses and Architectures*. Goddard Space Flight Center

Planetary CubeSat Science Institute. National Aeronautics and Space Administration. Retrieved from https://ssed.gsfc.nasa.gov/pcsi/docs/2017/presentations/012-Cubesat-Buses-and-Architectures-PCSI2017-v3.pdf

Gopinath, D. (Writer). (2018). The F-35B Lightning II Flies Over the Pacific [Video file]. In U. S. A. Force (Producer).

Gunter, B. C., & Maessen, D. C. (2010). *Applications of a networked array of small satellites for planetary observation*. Paper presented at the AIAA/AASAstrodynamics Specialist Conference., Toronto, Ontario, Canada.

Hague, C. N., Siegenthaler, L. E., & Rothman, L. J. (2003, December 9, 2002). *Enabling Responsive Space: F-15 Microsatellite Launch Vehicle.* Paper presented at the IEEE Aerospace, Big Sky, Montana.

Hamstra, J. W., & McCallum, B. N. (2010). Tactical Aircraft Aerodynamic Integration. In *Encyclopedia ofAerospace Engineering* (pp. 14). online: John Wiley & Sons, Ltd.

Harrington, B. E., Picka, B. A., & Cordova, H. S. (2011). *Space Shuttle Day-of-Launch Trajectory Design Operations*. Paper presented at the AIAA Space 2011 Conference & Exposition, Long Beach, CA. https://arc.aiaa.org/doi/pdf/10.2514/6.2011-7197

Harrison, T., Johnson, K., Roberts, T. G., Way, T., & Young, M. (2020). *SPACE THREAT ASSESSMENT 2020*. Retrieved from 1616 Rhode Island Avenue NW, Washington, DC 20036:

Herrera, D. (2016). Pegasus XL Mated to L-1011 Stargazer Carrier Aircraft. In 31095419890_d65bfd2939_o (Ed.), (Vol. 21.0 MB, pp. At Vandenberg Air Force Base in California, an Orbital ATK Pegasus XL rocket is mated to the company's L-1011 carrier aircraft near Vandenberg's runway. On board Pegasus are eight NASA Cyclone Global Navigation Satellite System, or CYGNSS, spacecraft. When preparations are competed at Vandenberg, the L-1011/Pegasus XL combination will be flown to NASA's Kennedy Space Center in Florida. On Dec. 1012, 2016, the carrier aircraft is scheduled to take off from the Skid Strip at Cape Canaveral Air Force Station and CYGNSS will launch on the Pegasus XL rocket with the L-1011 flying off shore. CYGNSS satellites will make frequent and accurate measurements of ocean surface winds throughout the life cycle of tropical storms and hurricanes.): NASA.

Holvoet, N., Vongsantivanich, W., Chaimatanan, S., & Delahaye, D. (2018). *Mission planning for non-homogeneous Earth observation satellites constellation for disaster response*. Paper presented at the SpaceOps 2018 Conference, Marseille, France. https://arc.aiaa.org/doi/pdf/10.2514/6.2018-2658

Horton, V. W., & Messing, W. E. (1963). *SOME OPERATIONAL ASPECTS OF USING A HIGH-PERFORMANCE AIRPLANE AS A FIRST-STAGE BOOSTER FOR AIR-LAUNCHING SOLID-FUEL SOUNDING ROCKETS*. Retrieved from Edwards Air Force Base, California:

Humphreys, T. E., Ledvina, B. M., Psiaki, M. L., O'Hanlon, B. W., & Kintner Jr., P. M. (2008). *Assessing the Spoofing Threat: Development of a Portable GPS Civilian Spoofer*. Paper presented at the 2008 ION GNSS+ Conference, Savanna, GA. https://repositories.lib.utexas.edu/handle/2152/63316

The International Celestial Reference System (ICRS). (2013, 2013). Retrieved from https://www.iers.org/IERS/EN/Science/ICRS/ICRS.html

Isaacs, R. (1965). *Differential Games: A Mathematical Theory with Applications to Warfare and Pursuit, Control and Optimization*. New York, NY: John Wiley and Sons.

ISIS 6U CubeSat. (2018). In I.-I. S. I. S. B.V. (Ed.). Motorenweg 23, 2623CR, Delft, The Netherlands.

Iwata, C. K., & Venturini, C. C. (2016). *Advances in small satellite technology and resilient space systems*. Paper presented at the AIAA Space 2016, Long Beach, CA.

Jenkin, A. B., McVey, J. P., & Peterson, G. E. (2012). *ISS Protection Process for the COLA Gap After Launch*. Paper presented at the AIAA SPACE 2012 Conference & Exposition, Pasadena, CA. https://arc.aiaa.org/doi/pdf/10.2514/6.2012-5334

Johnson, S. G. (2020). The NLopt non-linear optimization package (Version 2.6.2). online: GitHub. Retrieved from https://github.com/stevengj/nlopt

JSpOC Recommendations for Optimal CubeSat Operations. (2015). In D. o. Defense (Ed.): Joint Force Space Command (JFSCC).

Jung-Hyun, L., Ko, K. H., Ahn, H. S., Wang, S. M., Choi, S., Jung, O., & Chung, D. (2012). *Multi-satellite control system architecture and mission scheduling optimization*. Paper presented at the 2012 IEEE Aerospace Conference, Big Sky, MT. https://ieeexplore.ieee.org/abstract/document/6187437/keywords#keywords

Kan, S. (2007). *China's Anti-Satellite Weapon Test*. Retrieved from 101Independence Avenue, SE Washington, DC 20540-7500: https://apps.dtic.mil/dtic/tr/fulltext/u2/a468025.pdf

Karabeyoglu, A. (2008). *Hybrid Rocket Propulsion for Future Space Launch*. Paper presented at the Aero/Astro 50th Year Anniversary, Stanford University.

Karabeyoglu, A., Zilliac, G., Cantwell, B. J., DeZilwa, S., & Castellucci, P. (2003). *Scale-up Tests of High Regression Rate Liquefying Hybrid Rocket Fuels*. Paper presented at the 41st Aerospace Sciences Meeting and Exhibit, Reno, Nevada.

Karabeyoglu, A., Zilliac, G., Cantwell, B. J., DeZilwa, S., & Castellucci, P. (2004). Scale-Up Tests of High Regression Rate Paraffin-Based Hybrid Rocket Fuels. *Journal of Propulsion and Power, 20*(6), 9.

Keesey, L. (2017). NASA Set to Launch Dellingr; CubeSat Purposely Designed to Improve Reliability of Small Satellites [Press release]. Retrieved from https://www.nasa.gov/feature/goddard/2017/nasa-set-to-launch-dellingr-cubesat-purposely-designed-to-improve-reliability-of-small-0

Kelly, J. W., Rogers, C. E., Brierly, G. T., Martin, J. C., & Murphy, M. G. (2017). *Motivation for Air-Launch: Past, Present, and Future*. Paper presented at the AIAA Space Forum 2017, Orlando, FL. https://ntrs.nasa.gov/archive/nasa/casi.ntrs.nasa.gov/20170007919.pdf

Kepko, L., Clagett, C., Santos, L., Azimi, B., Berry, D., Bonalsky, T., . . . Zesta, E. (2017). *Dellingr: NASA Goddard Space Flight Center's First 6U Spacecraft*. Paper presented at the 31st Annual AIAA/USU Conference on Small Satellites, Logan, UT. https://digitalcommons.usu.edu/smallsat/2017/all2017/83/

Kepko, L., Santos, L., Clagett, C., Azimi, B., Chai, D., Cudmore, A., . . . Lucas, J. (2018). *Dellingr: Reliability lessons learned from on-orbit*. Paper presented at the 32nd Annual AIAA/USU Conference on Small Satellites, Logan, UT. https://digitalcommons.usu.edu/smallsat/2018/all2018/250/

Kim, J., & Lee, Y. J. (2009). Measurement Interpolation Methods for Dual One-Way Ranging Systems. *Journal of Spacecraft and Rockets, 46*(3), 6. doi:10.2514/1.42261

Kim, J., & Tapley, B. D. (2005). Optimal Frequency Configuration for Dual One-Way Ranging Systems. *Journal of Spacecraft and Rockets, 42*(4), 3. doi:10.2514/1.9974

Kloesel, K. J., & Clark, C. M. (2013). *Preliminary MIPCC Enhanced F-4 and F-15 Performance Characteristics for a First Stage Reusable Launch Vehicle*. Paper presented at the AIAA SPACE 2013 Conference and Exposition, San Diego, CA. https://ntrs.nasa.gov/archive/nasa/casi.ntrs.nasa.gov/20140008928.pdf
https://ntrs.nasa.gov/archive/nasa/casi.ntrs.nasa.gov/20140010526.pdf

Kloesel, K. J., Ratnayake, N. A., & Clark, C. M. (2011). *A Technology Pathway for Airbreathing, Combined-Cycle, Horizontal Space Launch Through SR-71 Based Trajectory Modeling*. Paper presented at the 17th AIAA International Space Planes and Hypersonic Systems and Technologies Conference, San Francisco, CA. https://ntrs.nasa.gov/archive/nasa/casi.ntrs.nasa.gov/20110013567.pdf

Klofas, B. (2018). Survey of CubeSat Communication Systems. In table (Ed.), (17 ed., pp. This chart shows the 757 total CubeSats deployed in orbit so far, for a total of 1937 Units.).

Ko, U.-D., Tapley, B. D., Ries, J. C., & Bettadpur, S. V. (2012). High-Frequency Noise in the Gravity Recovery and Climate Experiment Intersatellite Ranging System. *Journal of Spacecraft and Rockets, 49*(6), 11. doi:10.2514/1.A32141

Krepon, M., Mueller, K., Lewis, J., MacDonald, B. W., Nacht, M., Weeden, B. C., & Schoenberger, S. (2013). *Anti-satellite Weapons, Deterrence and Sino-American Space Relations*. Retrieved from Monterey, CA: https://apps.dtic.mil/dtic/tr/fulltext/u2/a587431.pdf

Krieger, G., Moreira, A., Fiedler, H., Hajnsek, I., Werner, M., Younis, M., & Zink, M. (2007). TanDEM-X: A Satellite Formation for High-Resolution SAR Interferometry. *IEEE Transactions on Geoscience and Remote Sensing, 45*(11), 25. doi:10.1109/TGRS.2007.900693

Lang, S. W. (2016). SMDC History: 25 years since first 'Space War'. Retrieved from The United States Army website: https://www.army.mil/article/161173/SMDC_History__25_years_since_first__Space_War_/?from=RSS

Lara, M., & Russell, R. P. (2008). Fast Design of Repeat Ground Track Orbits in High-Fidelity Geopotentials. *The Journal of the Astronautical Sciences, 56*(3), 13. doi:10.1007/BF03256555

LAUNCHCONJUNCTION ASSESSMENT HANDBOOK: 18 SPCS Process for Launch Conjunction Assessment. (2018). Retrieved from Combined Space Operations Center (CSpOC), Vandenberg Air Force Base, California, USA: www.space-track.org

LauncherOne Service Guide. (2019). In (1.2 ed.): Virgin Orbit, LLC.

Lawson, C. (2017). *The Station Comes of Age* (Vol. 4). 1 Administration Circle, China Lake, CA 93555-6100: Naval Air Warfare Center Weapons Division.

Lee, S.-J., & Choi, J.-Y. (2011). The Precision Validation of the Precise Baseline Determination for
Satellite Formation. *Journal of Astronomy and Space Sciences*(28), 63-70.

Liu, M., Yang, D., & Hao, F. (2017). Optimization for the Locations of Ambulances under Two-Stage Life Rescue in the Emergency Medical Service: A Case Study in Shanghai, China. *Hindawi: Mathematical Problems in Engineering, 2017*(1830480), 14. doi:10.1155/2017/1830480

A Look at China's SAM Shelters in the Spratlys. (2017). *Asia Maritime Transparency Initiative (AMTI)*, 5. Retrieved from Center for Strategic & International Studies (CSIS) website: https://amti.csis.org/chinas-sam-shelters-spratlys/#

Lt. Col. Whitney, J., USAF, Maj. Thompson, K., USAF, & Maj. Park, J. H., ROKMC. (2019). A Plan for a US Space Force: The What, Why, How, and When. *Air & Space Power Journal, 33*(3), 13.

Malphrus, B., Combs, M., Kruth, J., Fite, N., Twiggs, B., & Schulze, R. (2010). *A University-Based Ground Station: The 21 m Antenna at Morehead State University*. Paper presented at the Space Ops 2010.

Masters, D. (2018). *Seizing Opportunity: Spire's CubeSat Constellation ofGNSS, AIS, and ADS-B Sensors*. Paper presented at the 2018 Stanford Precision Navigation and Time Symposium, Menlo Park, CA. http://web.stanford.edu/group/scpnt/pnt/PNT18/presentation_files/I07-Masters-Spire_GNSS_AIS_ADS-B.pdf

McGrath, C. N., & Macdonald, M. (2016). *Analytical Low-Thrust Satellite Maneuvers for Rapid Ground Target Revisit*. Paper presented at the AIAA Space 2016, Long Beach, CA. https://arc.aiaa.org/doi/10.2514/6.2016-5294

Merrill, G. (2016). *Formation Flying for Satellites and Unmanned Aerial Vehicles*. Retrieved from Huntsville, AL: https://ntrs.nasa.gov/search.jsp?R=20160008059&hterms=Garrick+Merrill&qs=N%3D0%26Ntk%3DAll%26Ntt%3DGarrick%2520Merrill%26Ntx%3Dmode%2520matchallpartial%26Nm%3D123%7CCollection%7CNASA%2520STI%7C%7C17%7CCollection%7CNACA

Merrill, G., & Becker, C. (2015). *Formation Flying for Satellites and UAVs*. Paper presented at the ICUAS 2015 - International Conference on Unmanned Aircraft Systems, Denver, CO.

MICROSAT SPACECRAFT: X-Sat. (2020). In B. C. Technologies (Ed.), *Blue Canyon Technologies* (pp. 2). 5330 Airport Blvd, Ste 100, Boulder, CO 80301: Blue Canyon Technologies.

MISC 3™ 3U nanosatellite Bus Hardware Revision: A. (2014). In I. Pumpkin (Ed.), (Vol. MISC 3 715-00553 Rev. B, pp. 6): Pumpkin, Inc.

Montenbruck, O., Kahle, R., D'Amico, S., & Ardaens, J.-S. (2008). Navigation and Control of the TanDEM-X Formation. *The Journal of the Astronautical Sciences, 56*(3), 341-357.

Mori, S., Chang, K.-C., Chong, C.-Y., & Spain, S. (1988). *Tracking Performance Evaluation* (ADS-TR-1196-1
ESD-TR-89-128). Retrieved from Mountain View, CA:

Mosier, M., & Rutkowski, E. (1993). *PEGASUS XL DEVELOPMENT AND L-1011 PEGASUS CARRIER AIRCRAFT*. Paper presented at the 7th Annual AIAA/USU Conference on Small Satellites, Utah State University, Logan, UT. https://digitalcommons.usu.edu/smallsat/1993/all1993/22/

Mozhaev, G. V. (1972). The Problem of Continuous Earth Coverage and Kinematically Regular Satellite Networks, I. *Kosmicheskie Issledovaniya, 10*(6), 7.

Mozhaev, G. V. (1973). The Problem of Continuous Earth Coverage and Kinematically Regular Satellite Networks, II. *Kosmicheskie Issledovaniya, 11*(1), 9.

Nag, S., Li, A. S., & Merrick, J. H. (2017). Scheduling algorithms for rapid imaging using agile CubeSat constellations. *Advances in Space Research, 61*(2), 891-913. doi:10.1016/j.asr.2017.11.010

Nag, S., Li, A. S., Ravindra, V., Net, M. S., Cheung, K.-M., Lammers, R., & Bledsoe, B. (2019). *Autonomous Scheduling of Agile Spacecraft Constellations with Delay Tolerant*

Networking for Reactive Imaging. Paper presented at the 29th International Conference on Automated Planning and Scheduling
Berkley, CA. https://openreview.net/forum?id=rJeDNZq5FE

NANO/MICROSATELLITE MARKET FORECAST. (2020). Retrieved from https://www.spaceworks.aero/nano-microsatellite-forecast-10th-edition-2020/

Osedacz, R. P. (1989). *Orbit Determination of Sunlight Illuminated Objects Detected by Overhead Platforms.* (Master of Science in Astronautical Engineering), Air Force Institute of Technology Air University, Wright-Patterson Air Force Base, Ohio. (AFIT/GA/ENY/89J-3)

Payne, J. M. (1990). *Flight Test Handbook* (Third ed.). PO Box 3 USAF Academy, CO 80840-0003: JP Aviation.

Peet, M. (2018). *Spacecraft Dynamics and Control:*
Lecture 10: Rendezvous and Targeting - Lambert's Problem.

Pegasus User's Guide. (2007). In (6.0 ed.): Orbital ATK.

Peng, H., & Bai, X. (2018). Artificial Neural Network–Based Machine Learning Approach to Improve Orbit Prediction Accuracy. *Journal of Spacecraft and Rockets, 55*(5), 1248-1260. doi:10.2514/1.A34171

Pisacane, V. L. (2008). *The Space Environment and Its Effect on Space Systems*. Reston, VA: American Institute of Aeronautics and Astronautics.

Pomerantz, W., & Russell, K. (2019). Virgin Orbit Announces Partnership with Royal Air Force for Responsive Launch Campaign [Press release]. Retrieved from https://virginorbit.com/virgin-orbit-announces-partnership-with-royal-air-force-for-responsive-launch-campaign/

Pontani, M., & Conway, B. A. (2009). Optimal Trajectories of Anti-satellite Missiles. *Communications to SIMAI Congress, 3*(265), 12. doi:10.1685/CSC09265

Post, J., Bennett, M., Gilmore, J. M., Ramsay, A., Hall, R., & Jennings, S. (2007). *Alternatives for Military Space Radar* (1609). Retrieved from Washington, D.C.: https://www.cbo.gov/sites/default/files/110th-congress-2007-2008/reports/01-03-spaceradar.pdf

Powell, M. J. D. (1994). A Direct Search Optimization Method that Models the Objective and Constraint Functions by Linear Interpolation. *Advances in Optimization and Numerical Analysis*, 16.

Powell, M. J. D. (2009). *The BOBYQA algorithm for bound constrained optimization without derivatives*. Retrieved from Department of Applied Mathematics and Theoretical Physics,

Centre for Mathematical Sciences, Wilberforce Road, Cambridge CB3 0WA, United Kingdom: http://www.damtp.cam.ac.uk/user/na/NA_papers/NA2009_06.pdf

Rendon, A. (2006). *OPTIMAL COVERAGE OF THEATER TARGETS WITH SMALL SATELLITE CONSTELLATIONS.* (Master of Science (Space Systems)), Air Force Institute of Technology Air University, Wright-Patterson Air Force Base, Ohio. Retrieved from https://apps.dtic.mil/dtic/tr/fulltext/u2/a449417.pdf (AFIT/GSS/ENY/06-M12)

Renfro, B. A., Stein, M., Reed, E. B., Morales, J., & Villalba, E. J. (2019). *An Analysis of Global Positioning System (GPS) Standard Positioning Service Performance for 2019* (TR-SGL-20-02). Retrieved from Austin, Texas:

Reynolds, P. (1985). Anti-satellite launch. In ASM-135_ASAT_5 (Ed.), (Vol. 1.48 MB, pp. Anti-satellite launch. Maj. Wilbert "Doug" Pearson successfully launched an anti-satellite, or ASAT, missile from a highly modified F-15A Sept. 13, 1985 from Edwards Air Force Base over Pacific Missile Test Range, Calif. He scored a direct hit on a satellite orbiting 1340 miles overhead. Official USAF photo by Paul Reynolds). United States: United States Air Force.

Ridley, A. (2015, 20 Jul 2015). Calculating Coverage Statistics with CYGNSS. Retrieved from https://earthobservatory.nasa.gov/blogs/fromthefield/2015/07/20/calculating-coverage-statistics-with-cygnss/

Ruf, C. S., Chew, C. C., Lang, T., Morris, M. G., Nave, K., Ridley, A., & Balasubramaniam, R. (2018). A New Paradigm in Earth Environmental Monitoring with the CYGNSS Small Satellite Constellation. *Nature: Scientific Reports, 8*(8782). doi:10.1038/s41598-018-27127-4

Russell, K. (2019). Virgin Orbit Completes Key Drop Test Ahead of Orbital Test Flight. In droptest1 (Ed.), (Vol. 552 kb, pp. On this flight, Virgin Orbit released a fully built, fully loaded — although inert — LauncherOne rocket from Cosmic Girl, a modified Boeing 747 that serves as the rocket's carrier aircraft. Today's test flight began with a takeoff from the Mojave Air and Space Port at Mojave, CA, at 748:743 A.M. Pacific; the drop itself occurred at 749:713 A.M. Pacific from an altitude of 735,000 feet over a testing range at Edwards Air Force Base. The primary purpose of the test was to monitor the few critical seconds just after release, to ensure the rocket and aircraft separate cleanly and to observe how the rocket freefalls through the air.): Virgin Orbit.

Sarigul-Klijn, N., Sarigul-Klijn, M., & Noel, C. (2005). Air-Launching Earth to Orbit: Effects of Launch Conditions and Vehicle Aerodynamics. *Journal of Spacecraft and Rockets, 42*(3), 569-572. doi:10.2514/1.8634

Savitri, T., Kim, Y., Jo, S., & Bang, H. (2017). Satellite Constellation Orbit Design Optimization with Combined Genetic Algorithm and Semianalytical Approach. *Hindawi International Journal of Aerospace Engineering, 2017*, 17. doi:10.1155/2017/1235692

School, U. T. P. (1991). Energy. In *PERFORMANCE FLIGHT TEST PHASE* (Vol. 1, pp. 99). Edwards AFB, CA: United States Air Force.

Schor, D., Kinsner, W., & Thoren, A. (2009, 3-6 May 2009). *Satellite ground station emulator: An architecture and implementation proposal.* Paper presented at the 2009 Canadian Conference on Electrical and Computer Engineering.

Sella, V., Larkey, A., Majumder, A., Rao, A., Abidi, Z., Randeo, A., . . . Lembeck, M. F. (2020). *Development of a Nytrox-Paraffin Hybrid Rocket Engine*. Paper presented at the AIAA Propulsion and Energy 2020 Forum, VIRTUAL EVENT. research article retrieved from

Selva, D., Golkar, A., Korobova, O., Lluch i Cruz, I., & Weck, O. L. (2017). Distributed Earth Satellite Systems: What Is Needed to Move Forward? *Journal of Aerospace Information Systems, 14*(8), 26.

Shao, A., Koltz, E. A., & Wertz, J. R. (2014). *Quantifying the cost reduction potential for earth observation satellites*. Paper presented at the AIAA Space 2014, San Diego, CA.

Simpson, C. R. (2017). *Benefits of Tracking Aids on a 1U CubeSat*. Paper presented at the Educational Studies in Psychology, Research Methodology, and Medicine, University of Alabama, Tuscaloosa, AL, USA 35401.

Simpson, C. R., & O'Neill, C. (2016). *Computational Fluid Dynamics (CFD) Aided Analysis of the Stability of a Model Single-Stage Suborbital Rocket*. Paper presented at the AIAA Young Professionals 2017 - Greater Huntsville Area, Huntsville, AL.

Simurda, L., Stober, K. J., Boiron, A. J., Hornstein, K., Jens, E., & Fletcher, A. (2012). *Design and Development of a Thrust Vector Controlled Paraffin/Nytrox Hybrid Rocket*. Paper presented at the 48th AIAA/ASME/SAE/ASEE Joint Propulsion Conference & Exhibit, Atlanta, Georgia.

Small-Satellite Launch Services Market, Quarterly Update (Q1 2018), Forecast to 2030. (2018). Retrieved from https://go.frost.com/EUPRJHolmesMDD2SmallSatelliteMay18accessedonOctober8,2019

Smith, P. (2018). *A Review of the Competitive Space Transportation Industry, from Provider Options to Customer Needs*. Paper presented at the 2018 AIAA SPACE and Astronautics Forum and Exposition, Orlando, FL. https://arc.aiaa.org/doi/pdf/10.2514/6.2018-5238

Space Mission Analysis and Design. (2003). (J. R. Wertz & W. J. Larson Eds. 3rd ed.). El Segundo, CA, USA/ Dordrecht, The Netherlands: Microcosm Press/Kluwer Academic Publishers.

Space Safety and Mishap Prevention Program. (2014). Retrieved from https://static.e-publishing.af.mil/production/1/af_se/publication/afi91-217/afi91-217.pdf

Spurrier, Z. S., Walker, S. D., Merkley, S. L., & Whitmore, S. A. (2016). *Throttled Launch-Assist Hybrid Rocket Motor for a Towed Glider Air Launch Vehicle*. Paper presented at the 52nd AIAA/SAE/ASEE Joint Propulsion Conference, Salt Lake City, UT. https://arc.aiaa.org/doi/pdf/10.2514/6.2016-4658

STAFF, J. C. O. (2018). *Space Operations*.

Stephens, G. L., Vane, D. G., Boain, R. J., Mace, G. G., Sassen, K., Wang, Z., . . . Mitrescu, C. (2002). THE CLOUDSAT MISSION AND THE A-TRAIN. *Bulletin of the American Meteorological Society, 83*(12), 20. doi:10.1175/BAMS-83-12-1771

Stephens, G. L., Winker, D., Pelon, J., Trepte, C., Vane, D. G., Yuhas, C., . . . Lebsock, M. (2018). CloudSat and CALIPSO within the A-Train: Ten Years of Actively Observing the Earth System. *Bulletin of the American Meteorological Society, 99*(3), 14. doi:10.1175/BAMS-D-16-0324.1

Stokes, G. H., Yeomans, D. K., Jewitt, D., Bottke Jr., W. F., Chesley, S. R., Kelso, T., . . . Worden, S. P. (2003). *Study to Determine the Feasibility of Extending the Search for NearEarth Objects to Smaller Limiting Diameters*. Retrieved from

Strategic Command Directive (SD)505-1 VOL 1 Space Surveillance Operations - Basic Operations. (SD 505-1 V1). (2004). 901 SAC Blvd., Ste 1E21, Offutt AFB, NE 68113-6000: United States Strategic Command (USSTRATCOM).

Strategic Command Directive (SD)505-1 VOL 2 Space Surveillance Operations - Event Processing. (SD 505-1 V2). (2004). 901 SAC Blvd., Ste 1E21, Offutt AFB, NE 68113-6000: United States Strategic Command (USSTRATCOM).

Sugrue, K. A. (2007). *OPTIMAL ORBITAL COVERAGE OF THEATER OPERATIONS AND TARGETS.* (Master of Science in Astronautical Engineering), Air Force Institute of Technology Air University, Wright-Patterson Air Force Base, Ohio. Retrieved from https://apps.dtic.mil/dtic/tr/fulltext/u2/a469182.pdf (AFIT/GA/ENY/07-M17)

Symonds, K., Fornarelli, D., Mardle, N., Ormston, T., Flohrer, T., & Marc, X. (2014). *Operational Reality of Collision Avoidance Manoeuvre Execution*. Paper presented at the SpaceOps 2014 Conference, Pasadena, CA. https://arc.aiaa.org/doi/pdf/10.2514/6.2014-1746

Tapley, B. D., Bettadpur, S. V., Ries, J. C., Thompson, P. F., & Watkins, M. W. (2004). GRACE Measurements of Mass Variability in the Earth System. *Science, 305*(5683), 4. doi:10.1126/science.1099192

Tapley, B. D., Schutz, B. E., & Born, G. H. (2004). *Statistical Orbit Determination* (J. Hele Ed.). Oxford, United Kingdom: Elsevier Academic Press.

Taylor, R. A., Gogineni, P., Gurbuz, S. Z., Kolpuke, S., Li, L., O'Neill, C., . . . Matsuoka, K. (2019). *A prototype ultra-wideband FMCW radar for snow and soil-moisture*

measurements. Paper presented at the (IGARSS 2019) IEEE Interational Geoscience and Remote Sensing Symposium, Yokohama, Japan.

Thompson, R. C. (2015, Fall 2015). A Space Debris Primer. *Crosslink*, 4.

Townsend, G., Kraft, G., Kork, J., Russak, S., Tucker, B. E., & Magnus, J. (1963). *Orbital Flight Handbook: Part 1 - Basic Techniques and Data*. Retrieved from Huntsville, AL: https://ntrs.nasa.gov/archive/nasa/casi.ntrs.nasa.gov/19630011221.pdf

Transportation, D. o. (2008). GLOBAL POSITIONING SYSTEM WIDE AREA AUGMENTATION SYSTEM (WAAS) PERFORMANCE STANDARD. In (pp. 60). online: Federal Aviation Administration.

Transportation, D. o. (2020). GLOBAL POSITIONING SYSTEM (GPS) CIVIL MONITORING PERFORMANCE SPECIFICATION, 3rd Edition. In. online.

Tuli, T. S., Orr, N. G., & Zee, R. E. (2006). *Low Cost Ground Station Design for Nanosatellite Missions*. Paper presented at the AMSAT North American Space Symposium, Foster City, CA, USA.

Tyvak Platforms. (2020). In *Tyvak, Inc.* (pp. 1).

U.S. Standard Atmosphere, 1976 (NASA-TM-X-74335 NOAA-S/T-76-1562). (1976). Retrieved from Washington, D.C.: https://ntrs.nasa.gov/citations/19770009539

University, C. P. S., Obispo, S. L., & Lab, S. U. S. S. D. (2018). 6U CubeSat Design Specification. In (pp. 27): California Polytechnic State University.

Updated: China's Big Three Near Completion. (2017). *Asia Maritime Transparency Initiative (AMTI)*, 11. Retrieved from The Center for Strategic and International Studies (CSIS) website: https://amti.csis.org/chinas-big-three-near-completion/#

Vasquez, M., & Hao, J.-K. (2001). A "Logic-Constrained" Knapsack Formulationand a Tabu Algorithm for the Daily PhotographScheduling of an Earth Observation Satellite. *Computational Optimization and Applications, 20*(2), 137-157. doi:10.1023/A:1011203002719

Verver, G. (1958). NAF F4D-1 Skyray BuNo 130745, NOTSNIK, Armitage Field, China Lake. In Project_Pilot_on_ground_3 (Ed.), (Vol. 640 x 480 pixels, pp. F4D-1 Skyray with Project Pilot rocket launch vehicle.): U.S. Navy.

Vikan, E. (2011). *UiO Satellite Ground Station: Simulation, Implementation and Verification.* (Masters), The University of Oslo, Oslo, Norway.

Vonbun, F. O., Argentiero, P. D., & Schmid Jr., P. E. (1978). Orbit Determination Accuracies Using Satellite-to-Satellite Tracking. *IEEE Transactions on Aerospace and Electronic Systems, AES-14*(6), 8.

Wackerly, D. D., Mendenhall III, W., & Scheaffer, R. L. (2008). *Mathematical Statistics with Applications* (C. Crockett Ed. Seventh Edition ed.). 10 Davis Drive, Belmont, CA 94002-3098 USA: Brooks/Cole.

Walker, J. G. (1970). *Circular Orbit Patterns Providing Continuous Whole Earth Coverage*. Retrieved from

Walker, J. G. (1971). Some Circular Orbit Patterns Providing Continuous Whole Earth Coverage. *Journal of the British Interplanetary Society, 24*, 15.

Walker, J. G. (1977). *Continuous Whole Earth Coverage by Circular Orbit Satellite Patterns*. Retrieved from https://apps.dtic.mil/dtic/tr/fulltext/u2/a044593.pdf

Walker, J. G. (1982a). Comments on "Rosette Constellations of Earth Satellites". *IEEE Transactions on Aerospace and Electronic Systems, AES-18*(4), 2.

Walker, J. G. (1982b). *Coverage Predictions and Selection Criteria for Satellite Constellations*. Retrieved from

Wall, M. (2018). Elon Musk Says SpaceX Will Reuse a Rocket Within 24 Hours in 2019, 13. Retrieved from SPACE.com website: https://www.space.com/40581-spacex-reusable-rocket-goal-elon-musk.html

Wang, M., Luo, X., Dai, G., & Chen, X. (2016). Application of Latitude Stripe Division in Satellite Constellation Coverage to Ground. *Hindawi International Journal of Aerospace Engineering, 2016*, 9. doi:10.1155/2016/4315026

Weeden, B. C. (2017). Space Situational Awareness Fact Sheet. In S. W. Foundation (Ed.). Washington, D. C.: Secure World Foundation.

Weeden, B. C., & Samson, V. (2020). *Global Counterspace Capabilities: An Open Source Assessment*. Retrieved from

Werner, D. (2019, 20 May 2019). Satellites to the rescue after natural disasters. *SpaceNews*, 3.

Werner, D. (2020, 15 Jan 2020). Spire Global shares early data from GNSS Reflectometry satellites. *SpaceNews*, 2.

Wertz, J. R. (2011). Orbit and Constellation Design—Selecting the Right Orbit, 3. Retrieved from Space Mission Engineering website: http://www.sme-smad.com/GetMORE/SME-SMAD%20Ch%2010_FINAL_web_10.2.1.6.pdf

Whitehead, J. C. (2006). *Air Launch Trajectories to Earth Orbit*. Paper presented at the 42nd AIAA/ASME/SAE/ASEE Joint Propulsion Conference & Exhibit, Sacramento, CA. https://arc.aiaa.org/doi/pdf/10.2514/6.2006-4785

Whitmore, S. A., Merkley, S. L., Spurrier, Z. S., & Walker, S. D. (2015). *Throttled Launch-Assist Hybrid Rocket Motor for an Airborne NanoSat Launch Platform*. Paper presented at the 51st AIAA/SAE/ASEE Joint Propulsion Conference, Orlando, FL.

Wiegand, C., Bullick, B. A., Catt, J. A., Hamstra, J. W., Walker, G. P., & Wurth, S. (2018). *F-35 Air Vehicle Technology Overview*. Paper presented at the AIAA Aviation Forum 2018 Aviation Technology, Integration, and Operations Conference, Atlanta, Georgia, U.S.A. https://arc.aiaa.org/doi/10.2514/6.2018-3368

XB3 SPACECRAFT. (2020). In B. C. Technologies (Ed.), *Blue Canyon Technologies* (pp. 2). 5330 Airport Blvd, Ste 100, Boulder, CO 80301: Blue Canyon Technologies.

XB6 Spacecraft. (2020). In *Blue Canyon Technologies, Inc.* (pp. 2). 5330 Airport Blvd, Ste #100, Boulder, CO 80301.

XB12 SPACECRAFT. (2020). In B. C. Technologies (Ed.), *Blue Canyon Technologies*. 5330 Airport Blvd, Ste 100, Boulder, CO 80301: Blue Canyon Technologies.

Xue, Y., Li, Y., Guang, J., Zhang, X., & Guo, J. (2008). Small satellite remote sensing and applications – history, current and future. *International Journal of Remote Sensing, 29*(15), 4339-4372. doi:10.1080/01431160801914945

Yan, J.-B., Gogineni, P., Rodriguez-Morales, F., Gomez-Garcia, D., Paden, J., Li, J., . . . Hale, R. D. (2017). Airborne measurementsof snow thickness: Using ultrawide-band frequency-modulated-continuous-wave radars. *EEE Geoscience and Remote Sensing Magazine, 5*(2), 57-76.

Yan, J.-B., Nunn, J. A., Gogineni, P., O'Neill, C., Simpson, C. D., Taylor, R. A., . . . Eisen, O. (2019). *Surface-based multi-channel radar systems for ice sheet measurements*. Paper presented at the (IGARSS 2019) IEEE International Geoscience and Remote Sensing Symposium, Yokohama, Japan.

Yan, J.-B., Nunn, J. A., Gogineni, P., O'Neill, C., Simpson, C. D., Taylor, R. A., . . . Eisen, O. (2019). UHF Radar Sounding of Polar Ice Sheets. *IEEE Geoscience and Remote Sensing Letters*, 1-5. doi:10.1109/LGRS.2019.2942582

Zhen, L., Wang, K., Hu, H., & Chang, D. (2014). A simulation optimization framework for ambulance deployment and relocation problems. *Computers & Industrial Engineering, 72*, 12-23. doi:10.1016/j.cie.2014.03.008

Zribi, M., Motte, E., Baghdadi, N., Baup, F., Dayau, S., Fanise, P., . . . Wigneron, J. P. (2018). Potential Applications of GNSS-R Observations over Agricultural Areas: Results from the GLORI Airborne Campaign. *Remote Sensing, 10*(8), 17. doi:10.3390/rs10081245

APPENDIX

A. Mission Requirements

Figures of Merit	Description	Measurement Requirements	Comments
Mission lifetime	Determine each spacecraft's lifetime in orbit and the adverse or conducive effects on the resiliency and duration of the constellation/mission lifetime. The measured lifetime is an estimation based on atmospheric conditions in Low Earth Orbit (LEO).	atmospheric drag, gravitational effects, SRP, F10.7; perturbing forces that will affect satellite lifetime more than negligibly	Will need a high-fidelity solver like FreeFlyer/STK with numerical capability.
Satellite coverage	Earth coverage is of primary importance for a rapid response constellation or satellite formation. Time Average Gap (TAG), maximum gap duration, and Mean Response Time (MRT) will be of particular interest to evaluate the orbits selected for constellation coverage.	Field of regard and elevation mask of target, TAG (average duration of a gap if randomly sampled the system), MRT (average time from when we receive random request to observe a point until we can observe it). Qualitative assessment will be conducted using percent coverage, maximum gap, MRT, and TAG.	figures of merit should be industry-standards or common among academia to evaluate constellations
Reaction time	How long from request to initial view of target requested for observation? This will be determined using the FOM reaction time.	Time from request to observe a point until the first observations are downlinked. Reaction time is similar to mean response time, the average value of all response times for all time steps, but is only concerned with the first pass.	Constrained by time required to launch satellites directly into orbit.

B. Science Requirements

Science Themes	New Application Themes	Science Requirement	Description	Measurement Requirements	Comments	Source
Earth Observation (EO)	Orbital dynamics	Constellation revisit time	Minize the gap in coverage duration by optimizing the timing of orbit injection. Using averaged-orbital elements the constellation orbits can be selected	gap duration; simulation duration	Main perturbation is due to J2. Often good enough to use J2 to find true periodic orbit in full geopotential.	Coverage quality
Satellite Navigation (SatNav)	Position, Navigation, Timing (PNT)	Dilution of Precision (DoP)	Reconstitution of disabled or jammed GNSS. DoP is a geometric factor when multiplied by measurement and other input errors, gives the error in position/time.	Simulated performance of PNT Tx/Rx; DoP	DoP will be determined by orbital dynamics. Orbit selection will be important.	Coverage quality
Orbital dynamics	EO	Constellation's satellites lifetimes	Coverage performance degradation determined by a higher fidelity solver. Solar activity is primary driver of atmospheric density in LEO. Drag is the primary perturbing force (other than J2) at low altitudes.	orbit duration; perturbing forces; satellite Cd		Quality duration
Flight dynamics		Trajectory Planning	Aircraft and launch vehicle trajectories constrain orbits available to the constellation. The timing of aircraft flight and launch vehicle orbit injection constrain the reaction time, a key metric to the success of the airborne launch vehicle as a rapid reponse tool.	drag, weight (fuel, payload), gravitational force		Reaction time

C. Scripts

```
// Mission Plan Description and Console Setup

//On-Demand Launch Mission Planner provides a launch schedule to tactical
airborne launch platforms after optimizing possible coverage.
// This Mission Plan illustrates the use of FreeFlyer's optimization
capability to configure a constellation
// of 8 Spacecraft for coverage of a region. The constellation is divided
into eight planes with one Spacecraft per plane.
// The optimizer varies the inclination of the planes and the semi-major axis
of the Spacecraft. A cost function is established
// based on the semi-major axis. This enables FreeFlyer to find the best
coverage at the lowest altitude. Coverage is optimized
// over the period of 1/4th of a day. FreeFlyer first runs a propagation loop
inside the optimization process to compute the optimal
// solution. It will then run a final pass of the propagation loop, using the
best solution found by the Optimizer, to visualize the results.

// Console Setup

Console.DockMode = 3;
Console.Dimension = 50;
Console.BackColor = ColorTools.Black;
Console.CurrentTextColor = ColorTools.Yellow;
Console.WordWrap = 1;
Console.UseFixedWidthFont = 0;
Console.WindowTitle = "Status Console";
Console.Show();

Report "On-Demand Launch Mission Planner provides a launch schedule to
tactical airborne launch platforms after optimizing possible coverage. An
initial guess of each spacecraft state in the Walker constellation is
provided to FreeFlyer via runtime API interface or text file. The optimizer
varies the inclination, semimajor axis, and relative spacing of the
satellites to modify the constellation coverage. The best coverage over the
given simulation period is scheduled based on the relative phasing for
injection by airborne launch vehicles from each of the facilities. FreeFlyer
runs a propagation loop to compute the optimal solution. The best solution is
propagated again to visualize the results." to Console;

ApiLabel "SetCaseNum";

// Coverage Setup


// DoP
```

```
//Dilution of Precision (DoP) considers the number of satellites visible to
estimate the quality of SatNav solution provided to the user. Current GPS
satellite TLEs are ingested to use as desired in cases.
Array arrElevation;//elevation from target to satellites
Array arrAzimuth;//azimuth from target to satellites
Variable NumVisibleGPS;
Array arrDoPValues[5];//GDoP, PDoP, HDoP, VDoP, TDoP
Variable Az;
Variable El;
Variable AzGPS;
Variable ElGPS;
Array arrDoPValuesGPS[5];
Array arrElevationGPS;
Array arrAzimuthGPS;
Variable NumVisible;

Try sending ErrorCount to NumErrors;
      Open Celestrak;
End;

If(NumErrors > 0);
      Console.CurrentTextColor = ColorTools.Pink;
      Report "" to Console;
      Report "" to Console;
      Report "Error connecting to CelesTrak server.  You may not have a live
internet connection, or the server may be down." to Console;
      Stop;
End;

// Set MessageString to retrieve the GPS constellation TLEs
String MessageString = @"GET /NORAD/elements/gps-ops.txt HTTP/1.0\n";
Send MessageString to Celestrak;
Celestrak.ErrorAction = "Ignore";

Variable Status;
String DataString;
StringArray DataStringArray;
While (Status == 0);
      Receive DataString from Celestrak;
      Status = Celestrak.Status;
      DataStringArray.PushBack(DataString);
End;
// Remove HTTP Headers
String temp;
While (!DataStringArray[1].SubString(0,1).Compare("1"));
      temp = DataStringArray.PopFront;
End;
Variable i;
For i=0 to DataStringArray.Dimension-3 step 3;
      GPS.Count += 1;
      GPS[GPS.Count-1].LoadNoradTLE(DataStringArray[i:(i+2)]);
      GPS[GPS.Count-1].Color = ColorTools.Blue;
      GPS[GPS.Count-1].SetPropagatorType(TypeOf(Norad));
      (GPS[GPS.Count-1].Propagator AsType Norad).StepSize =
TimeSpan.FromSeconds(10);
End;
```

```
// Target(s) Setup

List<GroundStation> FixedFacilities;

Define Procedure DegreeHrMinSec2Decimal(Variable Hr, Variable Min, Variable
Sec, Variable final);
      final = Hr + (Min/60) + (Sec/3600);
EndProcedure;
Variable degree;
Array GAClat = {90-((2/8)*25), 90-((4/8)*25), 90-((5/8)*25), 90-((4/8)*25)};
Array GAClon = {180-15, 180, 180-45, 90+15};
TimeSpanArray ArcticCycloneEpochs(GAClon.Dimension);

If(CaseNum==0);
      //CSG Shandong attack on Hawaii
      //Timing
      StartEpoch = "Jan 27 2021 00:00:00.000".ParseCalendarDate();
      SimDuration = TimeSpan.FromHours(3);

      //Targets
      MovingTarget.Epoch = StartEpoch;
      MovingTarget.Latitude = 21.708333;// deg
      MovingTarget.Longitude = 360-175.116111;// deg
      MovingTarget.VelocityStateType = "Heading-Speed";
      MovingTarget.Heading = 90.0;// deg
      MovingTarget.Speed = 92.6;// km/hr, (50 knots)
      MovingTarget.ThreeDModelFile =
"C:\Users\simps\Documents\FreeFlyer\FreeFlyer 7.6.0.54542 (64-Bit)\Sample
Mission Plans\_Support_Files\navyship.3ds";
      MovingTarget.DisplayName = "Shandong CSG";

      //Facilities
      FacNum = 3;
      //moving
      MovingFacility.Epoch = StartEpoch;
      Call DegreeHrMinSec2Decimal(28, 42, 30, degree);
      MovingFacility.Latitude = degree;
      Call DegreeHrMinSec2Decimal(360-177, 6, 58, degree);
      MovingFacility.Longitude = degree;
      MovingFacility.VelocityStateType = "Heading-Speed";
      MovingFacility.Heading = 270.0;// deg
      MovingFacility.Speed = 92.6;// km/hr
      MovingFacility.ThreeDModelFile =
"C:\Users\simps\Documents\FreeFlyer\FreeFlyer 7.6.0.54542 (64-Bit)\Sample
Mission Plans\_Support_Files\navyship.3ds";
      MovingFacility.DisplayName = "Carl Vinson CSG";
      //fixed
      FixedFacilities.Count = 2;
      Call DegreeHrMinSec2Decimal(64, 38, 42, degree);
      FixedFacilities[0].Latitude = degree;
      Call DegreeHrMinSec2Decimal(360-147, 5, 32, degree);
      FixedFacilities[0].Longitude = degree;
      FixedFacilities[0].DisplayName = "Eielson AFB";
      Call DegreeHrMinSec2Decimal(34,    8, 40, degree);
```

```
      FixedFacilities[1].Latitude = degree;
      Call DegreeHrMinSec2Decimal(132, 14, 6, degree);
      FixedFacilities[1].Longitude = degree;
      FixedFacilities[1].DisplayName = "MCAS Iwakuni";

      Constellation.Count = FacNum*4; //4 satellites from each facility


      Console.CurrentTextColor = ColorTools.Green;
      Report @"Terrorists overrun the PLAN Shandong Carrier Strike Group
(CSG) and threaten Hawaii's civilian population with a ballistic missile
strike unless their demands are met. The Shandong CSG was performing a deep-
sea exercise across the international date line to demonstrate the PLAN's
long-term deployment capability and range. Unfortunately, this puts the now
terrorist-controlled CSG within several hours of striking distance of Hawaii.
\nResponding\n Carl Vinson CSG/VFA-14/F-35C \n Eielson AFB/356th FS/F-35A\n
MCAS Iwakuni/VMFA-121 and VMFA-242/ F-35B\n" to Console;


ElseIf(CaseNum==1);
      //FONOP at Mischief Reef
      //Timing
      StartEpoch = "Feb 11 2019 00:00:00.000".ParseCalendarDate();
      SimDuration = TimeSpan.FromDays(8);

      //Targets
      Call DegreeHrMinSec2Decimal(9, 54, 0, FixedTarget.Latitude);
      Call DegreeHrMinSec2Decimal(115, 32, 0, FixedTarget.Longitude);
      FixedTarget.DisplayName = "Mischief Reef";

      //Facilities
      FacNum = 3;
      //fixed
      FixedFacilities.Count = 3;
      Call DegreeHrMinSec2Decimal(34, 8, 40, degree);
      FixedFacilities[0].Latitude = degree;
      Call DegreeHrMinSec2Decimal(132, 14, 6, degree);
      FixedFacilities[0].Longitude = degree;
      FixedFacilities[0].DisplayName = "MCAS Iwakuni";
      Call DegreeHrMinSec2Decimal(32, 18, 10, degree);
      FixedFacilities[1].Latitude = degree;
      Call DegreeHrMinSec2Decimal(360-86, 24, 38, degree);
      FixedFacilities[1].Longitude = degree;
      FixedFacilities[1].DisplayName = "Maxwell AFB";
      Call DegreeHrMinSec2Decimal(13, 34, 55, degree);
      FixedFacilities[2].Latitude = degree;
      Call DegreeHrMinSec2Decimal(144, 55, 31, degree);
      FixedFacilities[2].Longitude = degree;
      FixedFacilities[2].DisplayName = "Andersen AFB";

      Constellation.Count = FacNum*4 + 4; //4 satellites from each facility


      Console.CurrentTextColor = ColorTools.Green;
      Report @"USN DDG-88 and DDG-111, Preble and Spruance, are conducting
innocent passage within 12 nautical miles of Mischief Reef in a Freedom of
Navigation Operation (FONOP).           Spoofing of GPS signals, (Harrison et
```

```
al., 2020; Weeden & Samson, 2020) can make navigation dangerous. Continuous
coverage via SAR and EO/IR imagery of Mischief Reef has been requested for a
week prior to and during the FONOP. During the FONOP, satellite navigation
(SATNAV) support is requested for the Ship's Inertial Navigation System
(SINS) to improve piloting.\n" to Console;


ElseIf(CaseNum==2);
      //Typhoon Vamco
      //Timing
      StartEpoch = "Nov 11 2020 00:00:00.000".ParseCalendarDate();
      SimDuration = TimeSpan.FromDays(3);

      //Targets
      FixedTarget.Latitude = 14.5;
      FixedTarget.Longitude = 124.0;
      FixedTarget.DisplayName = "Caramoan, Phillipines";

      //Facilities
      FacNum = 3;
      //fixed
      FixedFacilities.Count = 3;
      Call DegreeHrMinSec2Decimal(34, 8, 40, degree);
      FixedFacilities[0].Latitude = degree;
      Call DegreeHrMinSec2Decimal(132, 14, 6, degree);
      FixedFacilities[0].Longitude = degree;
      FixedFacilities[0].DisplayName = "MCAS Iwakuni";
      Call DegreeHrMinSec2Decimal(63, 41, 44, degree);
      FixedFacilities[1].Latitude = degree;
      Call DegreeHrMinSec2Decimal(9, 36, 26, degree);
      FixedFacilities[1].Longitude = degree;
      FixedFacilities[1].DisplayName = "Ørland Air Station";
      Call DegreeHrMinSec2Decimal(13, 34, 55, degree);
      FixedFacilities[2].Latitude = degree;
      Call DegreeHrMinSec2Decimal(144, 55, 31, degree);
      FixedFacilities[2].Longitude = degree;
      FixedFacilities[2].DisplayName = "Andersen AFB";

      Constellation.Count = FacNum*4; //4 satellites from each facility


      Console.CurrentTextColor = ColorTools.Green;
      Report @"Typhoon Vamco made landfall 11 November 2020 ten days after
super typhoon Goni made landfall along the same path in the Philippines.
Search and rescue efforts were hampered by communication and electricity
outages. The Makin Island Amphibious Ready Group (ARG) is directed to provide
humanitarian aid and disaster relief from Andersen AFB. Surge capability for
the DSCS and SA of the disaster region is provided via rapid responsive
launch.\n" to Console;


ElseIf(CaseNum==3);
      //Great Arctic Cyclone 2012
      //Timing
      StartEpoch = "Aug 6 2012 00:00:00.000".ParseCalendarDate();
      SimDuration = TimeSpan.FromDays(14);
```

```
	//Targets
	MovingTarget.Latitude = 90-((2/8)*25);// deg
	MovingTarget.Longitude = 180-15;// deg
	MovingTarget.SetPropagatorType("GroundWaypoints");
	For i=0 to GAClat.Dimension-1;
		ArcticCycloneEpochs[i] = StartEpoch + TimeSpan.FromDays(i);
		(MovingTarget.Propagator AsType
GroundWaypoints).AddWaypoint(ArcticCycloneEpochs[i], GAClat[i], GAClon[i]);
	End;
	MovingTarget.DisplayName = "Great Arctic Cyclone 2012";

	//Facilities
	FacNum = 2;
	//moving
	Call DegreeHrMinSec2Decimal(28, 42, 30, degree);
	MovingFacility.Latitude = degree;
	Call DegreeHrMinSec2Decimal(-177, 6, 58, degree);
	MovingFacility.Longitude = degree;
	MovingFacility.VelocityStateType = "Heading-Speed";
	MovingFacility.Heading = 270.0;// deg
	MovingFacility.Speed = 92.6;// km/hr
	MovingFacility.ThreeDModelFile =
"C:\Users\simps\Documents\FreeFlyer\FreeFlyer 7.6.0.54542 (64-Bit)\Sample
Mission Plans\_Support_Files\navyship.3ds";
	MovingFacility.DisplayName = "HMS Queen Elizabeth";
	//fixed
	FixedFacilities.Count = 1;
	Call DegreeHrMinSec2Decimal(34, 8, 40, degree);
	FixedFacilities[0].Latitude = degree;
	Call DegreeHrMinSec2Decimal(132, 14, 6, degree);
	FixedFacilities[0].Longitude = degree;
	FixedFacilities[0].DisplayName = "MCAS Iwakuni";

	Constellation.Count = FacNum*4; //4 satellites from each facility

	Console.CurrentTextColor = ColorTools.Green;
	Report @"HMS Queen Elizabeth CSG is performing a joint NATO exercise in
the Norwegian Sea during July. An Arctic cyclone, projected to match the
Great Arctic Cyclones 2012 and 2016, is predicted 3 days out (Doyle et al.,
2019). Atmospheric forcing may cause hazardous ice, weather, and sea
conditions for the exercise participants and international shipping. An
opportunity to demonstrate interagency collaboration on providing
meteorological returns to the joint force and continuing science return until
de-orbit. Meteorological and ISR return may require distributed
communications via terrestrial and orbital systems to surface ships
underway.\n" to Console;


End;
If(Verify==0);
	For i=0 to GPS.Count-1;
		GPS[i].Epoch = StartEpoch;
	End;
End;
MovingTarget.Epoch = StartEpoch;

// Constellation Setup
```

```
Variable j;
Variable T;
Variable P;
Variable F;
Variable PU;
Variable nSCsPerPlane;
List<Array> W;
List<Array> RAAN;
List<Array> Ecc;
List<Array> Apo;
List<Array> Inc;
P = FacNum;//planes
If(CaseNum==1);
      P=4;
End;
F = P; //relative spacing
T  = Constellation.Count;
PU = 360/T;
ApiLabel "ConstellationGuess";
RAAN.Count = P;
W.Count        = P;
Ecc.Count  = P;
Apo.Count  = P;
Inc.Count  = P;


If(Validate==0 and Verify==0);

      //Set the options for the formation.
      Constellation.ViewAsGroup = 1;
      //Given an initial semi-analytical analysis provide an initial guess to
the optimizer.
      nSCsPerPlane = Constellation.Count/P;
      For i=0 to P - 1;

            If(RAAN[i].Dimension==0);
                  RAAN[i].Dimension = nSCsPerPlane;
                  RAAN[i].Fill(0);
                  W[i].Dimension = nSCsPerPlane;
                  W[i].Fill(0);
                  Ecc[i].Dimension = nSCsPerPlane;
                  Ecc[i].Fill(0);
                  Apo[i].Dimension = nSCsPerPlane;
                  Apo[i].Fill(Earth.Radius + 400);
                  Inc[i].Dimension = nSCsPerPlane;
                  If(i<2);
                        Inc[i].Fill(FixedFacilities[i].Latitude);
                  Else;
                        Inc[i].Fill(MovingFacility.Latitude);
                  End;
            End;


            For j=0 to (nSCsPerPlane-1);
                  Constellation[j + i*nSCsPerPlane].Epoch = StartEpoch;
                  //Semi-analytical guess fill
```

```
                  Constellation[j + i*nSCsPerPlane].RAAN = deg(RAAN[i][j]);
                  Constellation[j + i*nSCsPerPlane].TA   =
AdjustToCyclicRange(0, 360, j*F*PU);
                  Constellation[j + i*nSCsPerPlane].W    = W[i][j];
                  Constellation[j + i*nSCsPerPlane].E    = Ecc[i][j];
                  Constellation[j + i*nSCsPerPlane].A    = Apo[i][j];
                  Constellation[j + i*nSCsPerPlane].I    = Inc[i][j];
                  // Add Sensors to the constellation members:
                  Constellation[j + i*nSCsPerPlane].AddSensor("s" + (j +
i*nSCsPerPlane).ToString);
                  Constellation[j + i*nSCsPerPlane].Sensors[0].MaskType = 1;
// Cone
                  Constellation[j + i*nSCsPerPlane].Sensors[0].Color =
Constellation[i].Color;
                  Constellation[j + i*nSCsPerPlane].Sensors[0].ConeHalfAngle
= 30;//60 deg Beamwidth
                  // Set propagator for each Spacecraft:
                  Constellation[j +
i*nSCsPerPlane].SetPropagatorType(TypeOf(J2Mean));
                  (Constellation[j + i*nSCsPerPlane].Propagator AsType
J2Mean).StepSize = TimeSpan.FromSeconds(10);
                  Constellation[j + i*nSCsPerPlane].DisplayName =
"Constellation"+ (j + i*nSCsPerPlane).ToString;
            End;
      End;
ElseIf(Validate==1 and Verify==0);

ElseIf(Validate==0 and Verify==1);
      Constellation.Count = 1;
      Constellation[0] = VerifySpacecraft;
      Constellation[0].Epoch = StartEpoch;
      Constellation[0].Longitude = MovingTarget.Longitude;
      // Add Sensors to the constellation members:
      Constellation[0].AddSensor("s0");
      Constellation[0].Sensors[0].MaskType = 1; // Cone
      Constellation[0].Sensors[0].Color = Constellation[0].Color;
      Constellation[0].Sensors[0].ConeHalfAngle = 5;//30 deg Beamwidth
//    Constellation[0].Sensors[0].ProjectionHeight = Constellation[0].A;
      // Set propagator for each Spacecraft:
      Constellation[0].SetPropagatorType(TypeOf(J2Mean));
      (Constellation[0].Propagator AsType J2Mean).StepSize =
TimeSpan.FromSeconds(1);
      Constellation[0].DisplayName = "Verification Spacecraft";
Else;
      Console.CurrentTextColor = ColorTools.Red;
      Report "Did you mean to run both validate and verify?" to Console;
      Stop;
End;
//Constellation[i].Epoch = StartEpoch;

// Contact and Coverage Setup
TimeSpanArray GapDuration;
TimeSpanArray TimeStatistics;
Array EventTypes;
VisibilityCalculator general;
general.VisibilityRequirement = 1;
```

```
List<Vector> Vectors;
//contact with targets
For i=0 to Constellation.Count-1;
      Vectors.Count+=1;
      If(CaseNum==0 or CaseNum==3);
            general.AddSegment(i.ToString()+MovingTarget.DisplayName);
            j = general.Segments.Count-1;
            Vectors[i].BuildVector(9, MovingTarget, Constellation[i]);
            Vectors[i].Color = ColorTools.Lime;
            Vectors[i].DrawMethod = 0;
            Vectors[i].Active = 0;
            //Set target and observer
            general.Segments[i].SetObserver(MovingTarget);
            general.Segments[i].SetTarget(Constellation[i]);
            general.Segments[i].AddOccultingBody(Earth);
            general.Segments[i].RefractionModelType = 0;
      ElseIf(CaseNum==1 or CaseNum==2);
            general.AddSegment(i.ToString()+FixedTarget.DisplayName);
            j = general.Segments.Count-1;
            Vectors[i].BuildVector(9, FixedTarget, Constellation[i]);
            Vectors[i].Color = ColorTools.Lime;
            Vectors[i].DrawMethod = 0;
            Vectors[i].Active = 0;
            //Set target and observer
            general.Segments[i].SetTarget(FixedTarget);
            general.Segments[i].SetObserver(Constellation[i]);
            general.Segments[i].AddOccultingBody(Earth);
            general.Segments[i].RefractionModelType = 0;
      End;
End;

////contact with facilities
//VisibilityCalculator CommFacility;
//CommFacility.VisibilityRequirement = 1;
//Variable k;
//
//For i=0 to Constellation.Count-1;
//    Vectors.Count+=1;
//    If(CaseNum==0 or CaseNum==3);
//          CommFacility.AddSegment(i.ToString()+MovingFacility.DisplayName);
//          j = CommFacility.Segments.Count-1;
//          Vectors[i].BuildVector(9, MovingFacility, Constellation[i]);
//          Vectors[i].Color = ColorTools.Lime;
//          Vectors[i].DrawMethod = 0;
//          Vectors[i].Active = 0;
//          //Set target and observer
//          CommFacility.Segments[j].SetTarget(MovingFacility);
//
      CommFacility.Segments[j].SetObserver(Constellation[i].Sensors[0]);
//          CommFacility.Segments[j].AddOccultingBody(Earth);
//          For k=0 to FixedFacilities.Count-1;
//
      CommFacility.AddSegment(i.ToString()+FixedFacilities[k].DisplayName);
//                j = CommFacility.Segments.Count-1;
//                Vectors[i].BuildVector(9, FixedFacilities[k],
Constellation[i]);
//                Vectors[i].Color =    ColorTools.Lime;
```

```
//                Vectors[i].DrawMethod = 0;
//                Vectors[i].Active = 0;
//                //Set target and observer
//                CommFacility.Segments[i].SetTarget(FixedFacilities[k]);
//
      CommFacility.Segments[i].SetObserver(Constellation[i].Sensors[0]);
//                CommFacility.Segments[i].AddOccultingBody(Earth);
//          End;
//
//    ElseIf(CaseNum==1 or CaseNum==2);
//          For k=0 to FixedFacilities.Count-1;
//
      CommFacility.AddSegment(i.ToString()+FixedFacilities[k].DisplayName);
//                j = CommFacility.Segments.Count-1;
//                Vectors[i].BuildVector(9, FixedFacilities[k],
Constellation[i]);
//                Vectors[i].Color = ColorTools.Lime;
//                Vectors[i].DrawMethod = 0;
//                Vectors[i].Active = 0;
//                //Set target and observer
//                CommFacility.Segments[i].SetTarget(FixedFacilities[k]);
//
      CommFacility.Segments[i].SetObserver(Constellation[i].Sensors[0]);
//                CommFacility.Segments[i].AddOccultingBody(Earth);
//          End;
//    End;
//End;

// Create Output Windows

// Create ViewWindow with a 3D ViewPoint
ViewWindow VW1({Vectors, FixedTarget, MovingTarget, FixedFacilities,
MovingFacility});
For i=0 to GPS.Count-1;
      VW1.AddObject(GPS[i]);
End;
For i=0 to Constellation.Count-1;
      VW1.AddObject(Constellation[i]);
End;
Viewpoint VP1;
VP1.ViewpointType = "view";
VP1.ViewpointName = "3dview1";
VP1.ThreeDView.ReferenceFrame = "body fixed";
VP1.ThreeDView.Declination = 13;
VP1.ThreeDView.RightAscension = 162.4;
VP1.ThreeDView.Radius = 1086.9;
VP1.ThreeDView.Target = MovingTarget.ObjectId;
VP1.ThreeDView.Source = MovingTarget.ObjectId;

Viewpoint VP2;
VP2.ViewpointType = "view";
VP2.ViewpointName = "3dview2";
VP2.ThreeDView.ReferenceFrame = "body fixed";
VP2.ThreeDView.Declination = 13;
VP2.ThreeDView.RightAscension = 162.4;
VP2.ThreeDView.Radius = 1086.9;
VP2.ThreeDView.Target =                 FixedTarget.ObjectId;
```

```
VP2.ThreeDView.Source = FixedTarget.ObjectId;

Viewpoint VP3;
VP3.ViewpointType = "view";
VP3.ViewpointName = "3dview3";
VP3.ThreeDView.ReferenceFrame = "body fixed";
VP3.ThreeDView.Declination = 24;
VP3.ThreeDView.RightAscension = 180;
VP3.ThreeDView.Radius = 62000;
VP3.ThreeDView.Target = FixedTarget.ObjectId;
VP3.ThreeDView.Source = FixedTarget.ObjectId;

Viewpoint VP4;
VP4.ViewpointType = "view";
VP4.ViewpointName = "3dview4";
VP4.ThreeDView.ReferenceFrame = "body fixed";
VP4.ThreeDView.Declination = 90;
VP4.ThreeDView.RightAscension = 180;
VP4.ThreeDView.Radius = 62000;
VP4.ThreeDView.Target = MovingTarget.ObjectId;
VP4.ThreeDView.Source = MovingTarget.ObjectId;

If(CaseNum==0);
      VW1.AddViewpoint(VP1);
      VW1.ActivateViewpoint("3dview1");
      //(Shandong.Propagator AsType GroundHeading).StepSize =
(Constellation[0].Propagator AsType J2Mean).StepSize;
ElseIf(CaseNum==1);
      VW1.AddViewpoint(VP2);
      VW1.ActivateViewpoint("3dview2");
ElseIf(CaseNum==2);
      VW1.AddViewpoint(VP3);
      VW1.ActivateViewpoint("3dview3");
ElseIf(CaseNum==3);
      VW1.AddViewpoint(VP4);
      VW1.ActivateViewpoint("3dview4");
End;

// Configure Optimizer

//view updates
GridWindow gw;

NloptOptions nlopt;
//PRAXIS 12 and Sbplx 29
nlopt.AlgorithmToUse = 29; // LN_BOBYQA Algorithm, 34,
nlopt.RelativeObjectiveTolerance = 1.0e-6; // COBYLA is only good to 1.0x10^-
3 solution of state variable
nlopt.RandomNumberSeed = 12345; // seed the random number generator that
nlopt uses internally to ensure results are the same run-to-run
nlopt.Population = 25;

IpoptOptions ipopt;
ipopt.Tolerance = 1e-6;
ipopt.AddIntOption("acceptable_iter", 25);
```

```
// Set Optimizer parameters
opt.ProblemName = "Coverage Optimization";
opt.MaximumNominalEvaluationCount = 250; // Use 250 evaluations to get a good
sampling but maintain a quick runtime
opt.FiniteDifferenceMethod = 0;
//Add objects to optimizer
opt.SaveObjectToProcess(TimeStatistics);
opt.SaveObjectToProcess(GapDuration);
opt.SaveObjectToProcess(EventTypes);
opt.SaveObjectToProcess(CountView);
Save MovingTarget;
opt.SaveObjectToProcess(MovingTarget);
Save FixedTarget;
opt.SaveObjectToProcess(FixedTarget);
For i=0 to Constellation.Count-1;
      Save Constellation[i];
      opt.SaveObjectToProcess(Constellation[i]);
End;

//Block state variables
// Add state variables
Variable lowSMA;
Variable higSMA;
lowSMA = ((1+((1-
Constellation[0].E)/(1+Constellation[0].E)))/2)*(Earth.Radius + 200);
higSMA = ((1+((1-
Constellation[0].E)/(1+Constellation[0].E)))/2)*(Earth.Radius + 600);
Variable objective;
String name;
If(Verify==0);
      For i=0 to (P-1);
            //A, apogee
            name = "apo#"+i.ToString();
            opt.AddStateVariable(name, Constellation[i*nSCsPerPlane].A,
lowSMA, higSMA);
            //E, eccentricity
            name = "ecc#"+i.ToString();
            opt.AddStateVariable(name, Constellation[i*nSCsPerPlane].E, 0,
0.999999);
            //I, inclination
            name = "inc#"+i.ToString();
            opt.AddStateVariable(name,Constellation[i*nSCsPerPlane].I, 0,
180);
      End;
      //F, rel spacing in reference plane
      name = "F";
      opt.AddStateVariable(name, F, 0, P);
Else;
      For i=0 to Constellation.Count-1;
            //A, apogee
            name = "apo#"+i.ToString();
            opt.AddStateVariable(name, Constellation[i*nSCsPerPlane].A,
lowSMA);
            //E, eccentricity
            name = "ecc#"+i.ToString();
```

```
            opt.AddStateVariable(name, Constellation[i*nSCsPerPlane].E, 0,
0.999999);
            //I, inclination
            name = "inc#"+i.ToString();
            opt.AddStateVariable(name,Constellation[i*nSCsPerPlane].I, 0,
180);
      End;
End;
// Add visit constraint
opt.AddConstraint("visit", 1);
If(Verify==0);
      opt.AddConstraint("view");
      opt.GetConstraint("view").SetUpperBound(1.0e-6);
End;
opt.FeasibilityTolerance = 1.0e-02;
StringArray OptPhase = {"Not Started", "Evaluating nominal case", "Evaluating
finite difference case", "Final pass of finite difference case"};
StringArray ReturnCode = {" ", "Success", "Stop value reached", "Objective
tolerance reached", "State variable tolerance reached", "Maximum iterations
reached","Maximum time reached"};
StringArray Feasible = {"Not feasible.", "Feasible."};
//EndBlock

//Load optimizer engine
opt.ValidateUserDerivatives = 0;
opt.LoadEngine(nlopt);
//opt.LoadEngine(ipopt);

Call ConfigureOptimizationGridWindow(gw, opt); // Call Procedure to configure
the GridWindow

// Report Coverage


// Dilution of Precision
Variable GDoP;
Variable PDoP;
Variable HDoP;
Variable VDoP;
Variable TDoP;
Variable GPS_GDoP;
Array GDoPhold;
Variable GPS_PDoP;
Variable GPS_HDoP;
Variable GPS_VDoP;
Variable GPS_TDoP;
// Create PlotWindow showing DoP values
PlotWindow PWDoP({GPS[0].EpochText, NumVisibleGPS, GDoP, PDoP, HDoP, VDoP,
TDoP, GPS_GDoP, GPS_PDoP, GPS_HDoP, GPS_VDoP, GPS_TDoP});
PWDoP.PointsToUpdate = 1;
PWDoP.WindowTitle = "DoP Values over time";
If(CaseNum==0);
      PWDoP.PlotTitle.Text = "DoP Values for " + MovingTarget.DisplayName;
ElseIf(CaseNum==1);
      PWDoP.PlotTitle.Text = "DoP Values for " + FixedTarget.DisplayName;
ElseIf(CaseNum==2);
```

```
      PWDoP.PlotTitle.Text = "DoP Values for " + FixedTarget.DisplayName;
ElseIf(CaseNum==3);
      PWDoP.PlotTitle.Text = "DoP Values for " + MovingTarget.DisplayName;
End;
PWDoP.XAxis.Title.Text = "Epoch";
PWDoP.YAxis.Title.Text = "Value";

// Create PlotWindow showing objective values
PlotWindow PWobj({opt.TotalEvaluationCount, objective});
PWobj.PlotSubTitle.Visible = 0;
PWobj.PointsToUpdate = 1;
PWobj.WindowTitle = "Objective Value Per Iteration";
If(CaseNum==0);
      PWobj.PlotTitle.Text = "Coverage solution for " +
MovingTarget.DisplayName;
ElseIf(CaseNum==1);
      PWobj.PlotTitle.Text = "Coverage solution for " +
FixedTarget.DisplayName;
ElseIf(CaseNum==2);
      PWobj.PlotTitle.Text = "Coverage solution for " +
FixedTarget.DisplayName;
ElseIf(CaseNum==3);
      PWobj.PlotTitle.Text = "Coverage solution for " +
MovingTarget.DisplayName;
End;
PWobj.XAxis.Title.Text = "Iteration";
PWobj.YAxis.Title.Text = "Value";

// Create PlotWindow showing objective values
PlotWindow PWa({opt.TotalEvaluationCount, Constellation[0].A});
PWa.PlotSubTitle.Visible = 0;
PWa.PointsToUpdate = 1;
PWa.WindowTitle = "Semimajor Axis Per Iteration";
PWa.PlotTitle.Text = "Semimajor Axis Per Iteration";
PWa.XAxis.Title.Text = "Iteration";
PWa.YAxis.Title.Text = "Semimajor Axis [km]";

PlotWindow PWE({opt.TotalEvaluationCount, Constellation[0].E});
PWE.PlotSubTitle.Visible = 0;
PWE.PointsToUpdate = 1;
PWE.WindowTitle = "Eccentricity Per Iteration";
PWE.PlotTitle.Text = "Eccentricity Per Iteration";
PWE.XAxis.Title.Text = "Iteration";
PWE.YAxis.Title.Text = "eccentricity";

PlotWindow PWI({opt.TotalEvaluationCount, Constellation[0].I});
PWI.PlotSubTitle.Visible = 0;
PWI.PointsToUpdate = 1;
PWI.WindowTitle = "Inclination Per Iteration";
PWI.PlotTitle.Text = "Inclination Per Iteration";
PWI.XAxis.Title.Text = "Iteration";
PWI.YAxis.Title.Text = "Inclination [deg]";
While (opt.IsRunning == 1);

   // Reset Parameters

   //coverage quality
```

```
   CountView = 0;
   NumTimeSteps = 0;
   objective = 0;
   TimeStatistics.Clear();
   GapDuration.Clear();
   EventTypes.Clear();

   //run optimization process
   // Reset objects
   opt.RestoreObjectsInProcess();
   general.ResetMethodStates();// Reset the VisibilityCalculator

   // Update State Variables
   opt.UpdateStateVariables();

   //Block state variables
   // update state variables
   If(Verify==0);
      For i=0 to P-1;
            For j=0 to nSCsPerPlane-1;
                  //A, apogee
                  name = "apo#"+i.ToString();
                  Constellation[j + i*nSCsPerPlane].A =
opt.GetStateVariableValue(name);
                  //ADD SOME LOGIC FOR RP HEIGHT TO LV TIME
                  //E, eccentricity
                  name = "ecc#"+i.ToString();
                  Constellation[j + i*nSCsPerPlane].E =
opt.GetStateVariableValue(name);
                  //I, inclination
                  name = "inc#"+i.ToString();
                  Constellation[j + i*nSCsPerPlane].I =
opt.GetStateVariableValue(name);
                  //F, rel spacing in reference plane
                  name = "F";
                  F = opt.GetStateVariableValue(name);
                  Constellation[j + i*nSCsPerPlane].TA =
AdjustToCyclicRange(0, 360, j*F*PU);
            End;
      End;
   Else;
      For i=0 to Constellation.Count-1;
                  //A, apogee
                  name = "apo#"+i.ToString();
                  Constellation[i*nSCsPerPlane].A =
opt.GetStateVariableValue(name);
                  //ADD SOME LOGIC FOR RP HEIGHT TO LV TIME
                  //E, eccentricity
                  name = "ecc#"+i.ToString();
                  Constellation[i*nSCsPerPlane].E =
opt.GetStateVariableValue(name);
                  //I, inclination
                  name = "inc#"+i.ToString();
                  Constellation[i*nSCsPerPlane].I =
opt.GetStateVariableValue(name);
      End;
   End;
```

```
   //EndBlock

   // Propagate Constellation
   GDoPhold.Clear();
   //Step Constellationellation over given duration while performing coverage
analysis
   While(Constellation[0].ElapsedTime < SimDuration);
      //Clear DoP holders
      NumVisible = 0;
      If(Verify==0);
            NumVisibleGPS = 0;

            arrAzimuth.Clear();
            arrElevation.Clear();
   //       arrDoPValues.Clear();
            arrElevationGPS.Clear();
            arrAzimuthGPS.Clear();
   //       arrDoPValuesGPS.Clear();


            // Dilution of Precision
            For i=0 to Constellation.Count-1;
                  If(general.Segments[i].Visibility(Constellation[0].Epoch));
                        Vectors[i].Active = 1;
                        If(CaseNum==0);
                              Az = MovingTarget.Azimuth(Constellation[i]);
                              El = MovingTarget.Elevation(Constellation[i]);
                        ElseIf(CaseNum==1);
                              Az = FixedTarget.Azimuth(Constellation[i]);
                              El = FixedTarget.Elevation(Constellation[i]);
                        ElseIf(CaseNum==2);
                              Az = FixedTarget.Azimuth(Constellation[i]);
                              El = FixedTarget.Elevation(Constellation[i]);
                        ElseIf(CaseNum==3);
                              Az = MovingTarget.Azimuth(Constellation[i]);
                              El = MovingTarget.Elevation(Constellation[i]);
                        End;
                        arrAzimuth.PushBack(rad(Az));
                        arrElevation.PushBack(rad(El));
                  Else;
                        Vectors[i].Active = 0;
                  End;
            End;
            //Number of visible satellites
            NumVisible = arrAzimuth.Dimension;
            If(NumVisible>0);
                  CountView += 1;
            End;
            //Call DoP procedure
            If(NumVisible>4);
                  Call CalcDoPUsingMatrix(arrElevation, arrAzimuth,
arrDoPValues, NumVisible);
                  //unpack DoP values and plot the values while updating the
view window
                  GDoP = arrDoPValues[0];
                  HDoP = arrDoPValues[1];
                  PDoP =                arrDoPValues[2];
```

```
                  VDoP = arrDoPValues[3];
                  TDoP = arrDoPValues[4];
            End;
            For i=0 to GPS.Count-1;
                  If(GPS[i].Elevation(MovingTarget)>5);
                        AzGPS = MovingTarget.Azimuth(GPS[i]);
                        ElGPS = MovingTarget.Elevation(GPS[i]);
                        arrAzimuthGPS.PushBack(rad(AzGPS));
                        arrElevationGPS.PushBack(rad(ElGPS));
                  ElseIf(GPS[i].Elevation(MovingTarget)>5);
                        AzGPS = FixedTarget.Azimuth(GPS[i]);
                        ElGPS = FixedTarget.Elevation(GPS[i]);
                        arrAzimuthGPS.PushBack(rad(AzGPS));
                        arrElevationGPS.PushBack(rad(ElGPS));
                  End;
            End;
            NumVisibleGPS = arrAzimuthGPS.Dimension;
            Call CalcDoPUsingMatrix(arrElevationGPS, arrAzimuthGPS,
arrDoPValuesGPS, NumVisibleGPS);
            //unpack DoP values and plot the values while updating the view
window
            GPS_GDoP = arrDoPValuesGPS[0];
            GPS_PDoP = arrDoPValuesGPS[1];
            GPS_HDoP = arrDoPValuesGPS[2];
            GPS_VDoP = arrDoPValuesGPS[3];
            GPS_TDoP = arrDoPValuesGPS[4];
            If(arrElevation.Dimension>0);
                  GDoPhold.PushBack(sqrt(GPS_GDoP^2 + GDoP^2));
            Else;
                  GDoPhold.PushBack(GPS_GDoP);
            End;
   //       Update PWDoP;
      End;


      // Figures of Merit
      If(CaseNum==0 or CaseNum==3);
            Call CalcCoverageQuality(general, MovingTarget.Epoch,
TimeStatistics, EventTypes, GapDuration, CountView);
      Else;
            Call CalcCoverageQuality(general, Constellation[0].Epoch,
TimeStatistics, EventTypes, GapDuration, CountView);
      End;
      If(CountView>=1 and Verify==1);
            Vectors[0].Active = 1;
      End;

      Step Constellation[0];
      If(Verify==0);
            GPS.StepToEpoch(Constellation[0].Epoch);
      End;
      NumTimeSteps += 1;
      For i=1 to Constellation.Count-1;
            Vectors[i].Epoch = Constellation[0].Epoch;
            Step Constellation[i] to
(Constellation[0].Epoch==Constellation[i].Epoch);
      End;
```

```
      MovingFacility.StepToEpoch(Constellation[0].Epoch);
      MovingTarget.StepToEpoch(Constellation[0].Epoch);
   End;

   // Update Objective Value
   //Block Objective Value
   If(Verify==1);
      If(GapDuration.Dimension==0);
            objective = 0;
      Else;
            //mean response time, average gap duration
            objective =
(GapDuration.ToArrayAsSeconds().Sum()/GapDuration.Dimension);
            //time averaged gap added to objective
            For i=0 to GapDuration.Dimension-1;
                  objective +=
((GapDuration[i]).ToSeconds()^2)/SimDuration.ToSeconds();
            End;
      End;
   ElseIf(CaseNum==0 or CaseNum==1);
      If(GapDuration.Dimension==0);
            objective = 0;
      Else;
            //mean response time, average gap duration
            objective =
(GapDuration.ToArrayAsSeconds().Sum()/GapDuration.Dimension);
            //time averaged gap added to objective
            For i=0 to GapDuration.Dimension-1;
                  objective +=
((GapDuration[i]).ToSeconds()^2)/SimDuration.ToSeconds();
            End;
      End;
      opt.SetConstraintValue("view", objective);
      objective += GDoPhold.Mean();

   ElseIf(CaseNum==2 or CaseNum==3);
      If(GapDuration.Dimension==0);
            objective = 0;
      Else;
            //mean response time, average gap duration
            objective =
(GapDuration.ToArrayAsSeconds().Sum()/GapDuration.Dimension);
            //time averaged gap added to objective
            For i=0 to GapDuration.Dimension-1;
                  objective +=
((GapDuration[i]).ToSeconds()^2)/SimDuration.ToSeconds();
            End;
      End;
      opt.SetConstraintValue("view", objective);
   End;
   //EndBlock

   // Calculate number of visits
   opt.SetConstraintValue("visit", CountView);
   Update PWobj;
   // Only update plots for nominal evaluations
   Console.CurrentTextColor =           ColorTools.Magenta;
```

```
   Report "Optimizer State; " + OptPhase[opt.OptimizationPhase] to Console;
   If (opt.OptimizationPhase==1);
      Report ReturnCode[opt.ReturnCode] to Console;
      Report Feasible[opt.IsFeasible()] to Console;
      Update PWa;
      Update PWE;
      Update PWI;
      Call UpdateOptimizationGridWindow(gw, opt);
   End;

   // Minimize the objective function
   opt.Minimize(objective);
End;

// Propagate Best Values
// Update State Variables
Call UpdateOptimizationGridWindow(gw, opt);
// Report to Console
Console.CurrentTextColor = ColorTools.Yellow;
Report "Optimizer Return Code: " + opt.ReturnString to Console;
Report "" to Console;
Console.CurrentTextColor = ColorTools.Lime;


//coverage quality
CountView = 0;
NumTimeSteps = 0;
objective = 0;
TimeStatistics.Clear();
GapDuration.Clear();
EventTypes.Clear();

//run optimization process
// Reset objects
opt.RestoreObjectsInProcess();
general.ResetMethodStates();// Reset the VisibilityCalculator
Restore MovingTarget;
Restore FixedTarget;
For i=0 to Constellation.Count-1;
      Restore Constellation[i];
End;


//Block state variables
// update state variables
If(Verify==0);
      For i=0 to FacNum-1;
            For j=0 to nSCsPerPlane-1;
                  //A, apogee
                  name = "apo#"+i.ToString();
                  Constellation[j + i*nSCsPerPlane].A =
opt.GetBestStateVariableValue(name);
                  //ADD SOME LOGIC FOR RP HEIGHT TO LV TIME
                  //E, eccentricity
                  name = "ecc#"+i.ToString();
                  Constellation[j + i*nSCsPerPlane].E =
opt.GetBestStateVariableValue(name);
```

```
                  //I, inclination
                  name = "inc#"+i.ToString();
                  Constellation[j + i*nSCsPerPlane].I =
opt.GetBestStateVariableValue(name);
                  //F, rel spacing in reference plane
                  name = "F";
                  F = opt.GetBestStateVariableValue(name);
                  Constellation[j + i*nSCsPerPlane].TA =
AdjustToCyclicRange(0, 360, j*F*PU);
            End;
      End;
Else;
      Vectors[0].Active = 1;
      For i=0 to Constellation.Count-1;
            //A, apogee
            name = "apo#"+i.ToString();
            If(opt.GetBestStateVariableValue(name)==-999);
                  For i=0 to Constellation.Count-1;
                        Restore Constellation[i];
                  End;
            Else;
                  Constellation[i*nSCsPerPlane].A =
opt.GetBestStateVariableValue(name);
                  //ADD SOME LOGIC FOR RP HEIGHT TO LV TIME
                  //E, eccentricity
                  name = "ecc#"+i.ToString();
                  Constellation[i*nSCsPerPlane].E =
opt.GetBestStateVariableValue(name);
                  //I, inclination
                  name = "inc#"+i.ToString();
                  Constellation[i*nSCsPerPlane].I =
opt.GetBestStateVariableValue(name);
            End;
      End;
End;
//EndBlock

While(Constellation[0].ElapsedTime < SimDuration);
      Update VW1;

      Step Constellation[0];
      If(Verify==0);
            GPS.StepToEpoch(Constellation[0].Epoch);
      End;
      NumTimeSteps += 1;
      For i=1 to Constellation.Count-1;
            Vectors[i].Epoch = Constellation[0].Epoch;
            Step Constellation[i] to
(Constellation[0].Epoch==Constellation[i].Epoch);
      End;
      MovingFacility.StepToEpoch(Constellation[0].Epoch);
      MovingTarget.StepToEpoch(Constellation[0].Epoch);
End;
```